ABSTRACT

Title of Document:	TEMPERATURE DEPENDENCE OF THE GROWTH MODE DURING HOMOEPITAXY ON PATTERNED GALLIUM ARSENIDE (001); ATOMIC-SCALE MECHANISMS FOR UNSTABLE GROWTH.
	Tabassom Tadayyon-Eslami, Doctor of Philosophy, 2006
Directed By:	Professor Raymond J. Phaneuf, Department of Materials Science and Engineering

In this thesis we present an extensive investigation of instability in molecular beam epitaxial growth of GaAs(001) over a range of pattern periods, cell sizes, growth temperature and As_2 flux. We find very good agreement with predictions of the continuum models of Sun, Guo and Grant [Phys. Rev. A **40**, 6763(1989)] for the growth above ~540ºC and Lai and Das Sarma [Phys. Rev. Lett. **66**, 2348 (1991)] for the growth below this temperature. Changing the growth temperature to lower than 540 ºC leads to the formation of ring-like protrusions in the [110] direction around pits patterned on the initial substrate, which are absent for growth at higher temperature. This change in growth mode occurs in the temperature range within in which both pre-roughening transition and surface reconstruction transition (β_2(2x4) to c(4x4)) also occur.

We rule out the possibility of preroughening and the change in surface reconstruction as the reason for this growth mode change, based on the As_2 flux dependence of the growth mode transition temperature.

Based on our atomic force microcopy characterization of the surface morphology during early the stage of growth, we propose a physically based model for the growth, which involves a competition between decreased adatom collection efficiency during growth on small terraces and a small anisotropic multiple step Ehrlich-Schwoebel barrier at the pit edge. This provides a physical basis for the nonlinear term in the continuum models proposed by Sun et. al., and Lai and Das Sarma, whose predictions qualitatively describe our experimental observations.

TEMPERATURE DEPENDENCE OF THE GROWTH MODE DURING HOMOEPITAXY ON PATTERNED GALLIUM ARSENIDE (001); ATOMIC-SCALE MECHANISMS FOR UNSTABLE GROWTH

By

Tabassom Tadayyon-Eslami

Dissertation submitted to the Faculty of the Graduate School of the
University of Maryland, College Park, in partial fulfillment
of the requirements for the degree of
Doctor of Philosophy
2006

Advisory Committee:
Professor Raymond J. Phaneuf, Chair
Professor Ellen D. William
Professor Goettlieb S. Oehrlein
Professor Lourdes G. Salamanca-Riba
Professor Robert M, Briber

Dedicated

To My parents

Acknowledgements

I would first like express my gratitude to my adviser Prof. Raymond J. Phaneuf, for showing his support and extreme patience with me in completing this thesis. I am also deeply grateful to Dr. Hung-Chih Kan, whose valuable guidance helped me out with all my problems. I am grateful to Mr. William K. Klomparens and Dr. William E. Vanderlinde for supporting me at the LPS and giving me the opportunity to use its excellent facilities.

I really appreciate the help I had from Dr. Michael Dreyer, Mark Thornton, Greg Latini, Dr. Lynn Calhoun, Dr. S. Kanakaraju and Dr. Christopher Richardson for helping me with my MBE growths, Laurence C. Olver, Lisa Lucas and Steven Brown for helping me in the cleanroom. Taesoon Kwon, Sonam Shah, Sherman Guo and Dominic Britti for helping me in the lab, Erin Flanagan and Alex Sztein for their help with the AFM measurements and data analysis.

Finally I have to thank to whom I am indebted for being very valuable to me with my life and work, Professor Aris Christou, Annette Mateus, Cristina Phaneuf, my parents and my dearest Tirazheh.

Table of Contents

List of Tables

List of Figures

Chapter 1

Introduction

1.1 Motivation:

Over the past two decades there has been continued technological interest in the controlled preparation of thin multilayer films of GaAs and related compounds for device applications [1]. Specific properties of GaAs such as high electron mobility and direct band structure have led to the use of this material for a variety of important semiconductor devices such as vertical cavity surface emitting lasers (VCSEL) and high electron mobility transistors (HEMT). Vertical cavity surface lasers are composed of multilayer thin films with the prototypical example made up of layers of GaAs, AlAs and InAs; High mobility GaAs-based transistors and IC's find applications in microwave communications, radar technology and RF chips for cell phones due to their low power consumption, high speed and low signal distortion. An important issue in any of these applications is interface roughness, which degrades device efficiency due to scattering of carriers and / or light.

In addition to the technological importance of this issue, from a scientific point of view it would be very interesting to understand and predict the evolution of surface roughness, and to describe whether or not the amplitude of the corrugation (roughness) will increase or decrease with growth. A related issue is whether growing a buffer layer will smooth existing roughness. We expect that both temperature and the fluxes of the individual chemical components will affect the roughening or smoothing during growth. In particular, higher temperatures might promote the growth closer to equilibrium

conditions, however the increased sublimation rate limits the practical maximum. In addition, the surface reconstruction is known to change with temperature, and the surface may roughen either due to entropy, or kinetics.

In this thesis I will describe an investigation aimed at understanding the dependence of the growth mode on the temperature and flux, and in particular on the preroughening and reconstructive transitions. I adopt the technique of patterning which Shah et al, [2, 3] have described earlier, to allow a clear identification of the length scale variation of the evolution of surface corrugation during growth, and to simplify the interpretation of these results. The work I describe here considerably extends the earlier studies, investigating the dependence of the evolution during growth on two independent length scales: the pattern period and the initial feature size.

I also describe an investigation of the variation of the unstable growth mode as the temperature is lowered through the preroughening transition [4] and identify a profound change. I use the As_2 flux dependence to rule out possible thermodynamic driving mechanisms. Finally, I suggest physically-based effects to explain the correspondence between our temperature dependent results and continuum theories [5] which until now have been phenomenological in nature.

Background

1.1.1 Previous Studies of Homoepitaxy of GaAs (001):

The central work described in this thesis is an experimental characterization of the temperature dependence of the evolution of surface roughness of GaAs(001) surface during homoepitaxial growth. There have been a series of studies on the evolution of the surface morphology of GaAs(001) on unpatterned substrates. A very large number of studies have been performed on homoepitaxial growth on GaAs(001) during molecular beam epitaxy (MBE), a technique described further in section 1.2 [6 –13]. Neave and Joyce [12] studied the temperature range for the homoepitaxial MBE growth of GaAs (with As_4). They found GaAs films which maintained a reconstructed surface could be grown down to 257 ºC and even 92 ºC, however GaAs deposited below ~ 480 ºC is highly resistive. Using a high substrate temperature reduced the total deep trap level concentration in MBE GaAs [13]. Based in part on measurements of device performance or photoluminescence and partly on observations from reflection high energy electron diffraction (RHEED) [14] a set of standard temperatures and fluxes have been developed which were thought to optimize control of the surface. The advent of the use of scanning tunneling microscope to image MBE grown surfaces brought surprises, including observation of formation of stacked-up islands or "mounds" under standard conditions [15 - 20]. Up to now most experimental studies have been done on unpatterned GaAs surfaces. G. Apostolopoulos et. al. also reported reentrant formation of mounds elongated along [$\underline{1}$10] on GaAs (001) at temperature about 210 ºC and smooth surface as the result of higher growth temperature (580 ºC)[16]. M. Adamcyk, et al. further studied the effect of the starting surface on the formation of mounds and found growth on a smooth surface

leads to smooth morphology while growth on rough surface leads to the formation of mounds [21]. Shah et al. confirmed this [2], and further identified a transient instability of these surfaces toward amplifying corrugations created by patterning.

Yet another interesting observation made possible by imaging GaAs surfaces with STM in the absence of growth comes from Labella et. al. who reported that GaAs (001) surface undergoes a preroughening transition in which a large density of islands spontaneously appears. They found that the onset temperature increases with As_4 flux [14, 15].

There have also been other reports on growth on patterned surfaces, including work by D. Vveddensky et. al. who in addition performed computer simulations of the temperature dependence of the growth kinetics on V- grooved GaAs(001) surfaces [22, 23]. They found that at high growth temperatures adatoms migrate from a high free energy facet to a low energy one, leading to a negative growth rate at the higher energy facet. However at lower growth temperature, since the atoms cannot move easily to the lower energy facet, growth proceeds in a shape-preserving manner.

1.1.2 General Consideration in Growth on surfaces:

Crystalline solids are known as to be the stable form of most materials at low temperature under moderate pressure (with the exception of helium). The reason that many of the materials around us are not single-crystalline is that crystal growth is kinetically hindered. It is subject to barriers and instabilities which cause defects and finally polycrystalline or amorphous material. Single crystal growth generally starts with a seed. In the case of 2-D epitaxy, the seed is called the substrate. Usually the substrate is

a single crystal, cut along a low miller index plane. Almost invariably, however it is misoriented to some degree from the intended orientation. Usually wide terraces appear, divided by mono-atomic steps to compensate for the misorientation (Misoriented Si(111) provides an exception to this, as it facets into flat regions separated by step bunches [24, 25]).

An intentionally misoriented surface is called a *vicinal* surface, in contrast to an ideally flat *exactly atomically flat low index oriented* surface. For a uniform vicinal surface, the distance between steps, called the terrace width L, depends only on the misorientation angle (α) and the step height (h):

$$L(\alpha, h) = h \big/ \tan\alpha$$

During growth an adatom which arrives at the surface may be adsorbed at different sites on the surface. Fig. 1.1 shows examples. The adatom may be caught by a vacancy or a step edge, then it is bound very tightly, in contrast to an adatom that just sits on an ideal terrace site. For this reason vacancies are generally immediately filled via diffusion from less highly coordinated sites at the beginning of growth, at least in near-equilibrium conditions. In addition, vacancies are very unlikely to be formed during growth in great numbers, because a relatively large number of atoms would need to be previously attached to other sites in exactly the right order. Thus, during growth on real surfaces vacancies appear only rarely and can be neglected.

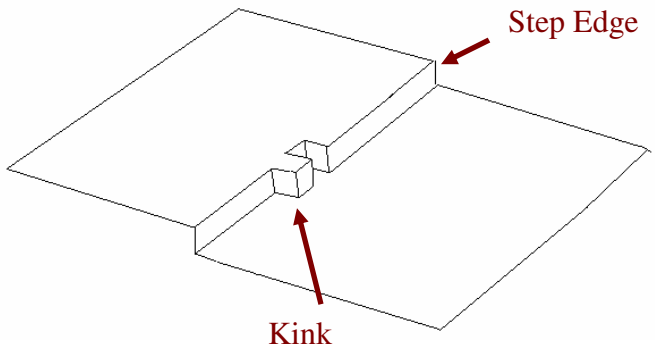

Fig.1.1 Schematic of different sites for an atom on the surface.

The number of nearest neighbor sites an adatom has depends strongly on crystal symmetry and orientation of the surface.

The growth of any single crystal includes the following steps:

1) Adsorption of an atom/ molecule at the surface

2) Diffusion of an atom/ molecule on the surface

3) Incorporation: during the diffusion an atom/ molecule may reach a site with high number of next nearest neighbor sites and incorporate.

4) Desorption of an atom/ molecule from the surface, which competes with incorporation. The longer the adatom diffuses on the surface the higher the probability of desorption.

Fig.1.2 shows the above four steps for growth of a single crystal. In some cases, an additional step is the dissociation of a molecular species either during adsorption, or incorporation. As we mentioned earlier, growth is generally subjected to instabilities and these instabilities are particularly important at the surface, where the dynamics are faster. Growth instabilities were classified by Politi, et. al. as follows: [26]:

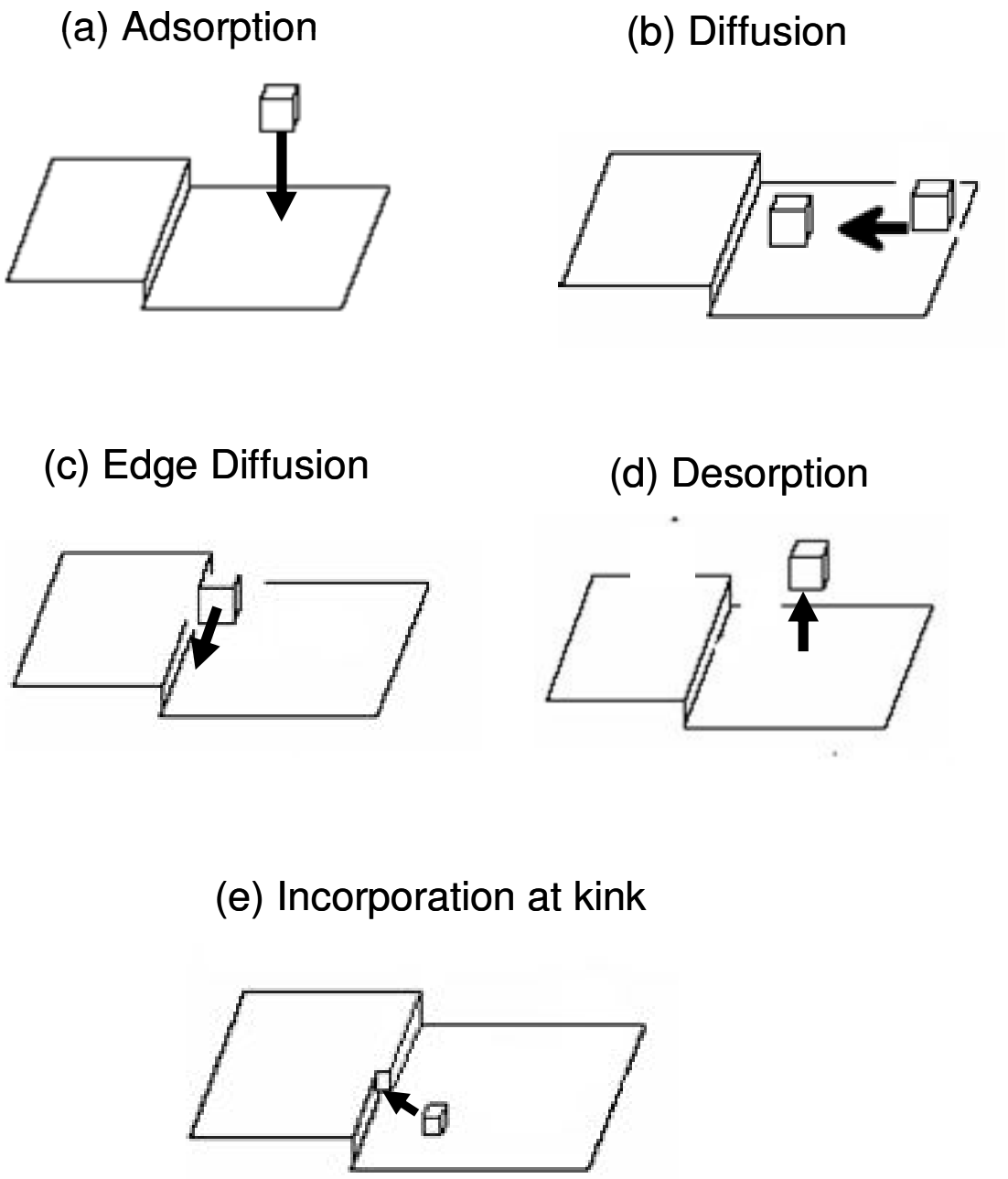

Fig. 1.2 Schematic of the different steps for growing the single crystals, (a) adsorption of adatom, (b) Diffusion of an adatom on surface, (c) Diffusion of an adatom along the step edge, (d) desorption from the surface, (e) incorporation of an adatom to the kink site.

a) *Diffusion instabilities*; this kind of instability is typical for the growth from solution or from melts. In the case of limited diffusion, atoms or molecules tend to stick to the

nearest point of the solid, and dendrites form.

b) *Kinetic instabilities*; these usually happen when the growth is fast compared to diffusion and the surface can not attain its equilibrium shape.

c) Thermodynamic instabilities; these occur during the formation of thermodynamically unstable materials or during the heteroepitaxial growth with lattice mismatch.

d) *Geometric Instabilities*; an example is shadowing, in which the geometry of the surface prevents stable and uniform growth.

1.1.3 Diffusion on Surfaces:

Diffusion on a solid surface is the motion of particles or adatoms on a discrete lattice. Usually there are two parameters which characterize the diffusion, the diffusion length and diffusion hopping rate.

Diffusion length is the mean distance on the surface that the monomer travels before it joins the surface (incorporation), or it leaves the surface (evaporation).
The diffusion hopping rate is the inverse of the average time needed for an adatom to jump from one site to another on the surface. Usually in MBE the diffusion hopping rate is fast compared to the typical arrival rate from the flux, at typical growth rates of a ~ 0.1-1 monolayer per second.

Diffusion length and hopping rate may differ for different directions, but it is usually assumed that diffusion along the different directions is independent. The adatom has to overcome the activation barrier of diffusion (E_{Diff}) for each single step, so that the diffusion can be written [27]

$$D = D_0 \exp\left(-\frac{E_{Diff}}{k_B T}\right) \quad (1.1)$$

D: Diffusion Constant
D_0: Maximum Diffusion Constant (at infinite Temperature)
E_{Diff}: Activation Energy for diffusion
K_B: Boltzmann constant
T: Absolute temperature

The average time for diffusion, τ_D, depends on the event that stops diffusion. If nucleation of an island occurs, then τ_D is equal to time between collisions of an atom with an island. Desorption is another possible event. In this case τ_D depends on the rest time on the surface.

These two limits lead to different growth regimes: nucleation-limited diffusion and desorption-limited diffusion. A high growth rate (i.e. a high adatom density on the surface) corresponds to nucleation limited diffusion and small growth rates and higher temperatures correspond to desorption limited diffusion. At higher temperature and smaller incoming flux, more adatoms can desorb before a new island nucleates.

A nucleation event comes from the collision of a large enough number of adatoms to form a critically sized island; for GaAs(001) under standard growth conditions this is thought to correspond to two Ga adatoms colliding in the presence of adsorbed As_2 [28]. Higher density of diffusing monomers leads to a higher probability of nucleation events, i.e. a higher 2- D flux of incoming species.

A higher nucleation probability however, means a shorter time τ_D for diffusion. Thus, τ_D is approximately inversely proportional to the adatom density on the surface in this regime [27]:

$$\tau_D = \frac{N_A}{J} \qquad (1.2)$$

τ_D : Diffusion time
N_A: Number of adatoms on the surface
J: Number of adatoms per unit surface per unit time

From this, and the previous equation, we can derive, the diffusion length [1.27]:

$$\lambda(N_A, J, T) = \sqrt{D_0 N_A / J}\, \exp\left(-\frac{E_{Diff}}{2k_B T}\right) \qquad (1.3)$$

From this it is obvious that since the whole exponent is negative and the temperature is in the denominator, *the diffusion length increases exponentially with temperature in the nucleation-limited regime.*

In the desorption-limited regime, an adatom desorbs if it has enough energy for desorption, therefore the residence time τ_D has an activated energy form:

$$\tau_D = \tau_0 \exp\left(\frac{E_{Des}}{k_B T}\right) \qquad (1.4)$$

Here E_{Des} is the desorption energy.

At higher temperature τ decreases and the dependence of the diffusion length (λ) is obtained from the following equation [27],

$$\lambda(T) = \sqrt{D_0}\,\tau_0 \exp\left(\frac{E_{Des} - E_{Diff}}{2k_B T}\right) \qquad (1.5)$$

The activation energy for diffusion is normally smaller than for desorption, otherwise the adatom would desorb immediately from the surface before diffusing. Therefore the *diffusion length decreases with increasing temperature* in the desorption-limited regime.

For GaAs during growth, both gallium and arsenic, in the form of $As_{2,}$ diffuse on the surface [28]. Arsenic has much higher vapor pressure, thus up to a thousand times more arsenic than gallium is directed to the surface. Usually arsenic is present in excess, and under this condition, it is thought that the arrival and diffusion of gallium controls the growth [29]. However, as more arsenic is exposed to the surface, the probability for a diffusing gallium atom to form a bond to an arsenic molecule and to be incorporated is higher, therefore the effect of changing the arsenic flux is definitely not negligible [29]. On the other hand, if more gallium is incorporated, fewer diffusing atoms move on the surface and the mean free path for diffusion increases.

The free diffusion time τ_D is affected by the gallium flux J_{Ga}, τ_D is inversely proportional to the number of gallium atoms on the surface. However an indirect As-effect also exists, because more arsenic on a surface lowers the effective density of unincorporated diffusing gallium atoms. The diffusion length λ_D is usually measured for certain growth parameters, then the activation energy E_{Diff} can in principle be obtained from an Arrhenius plot of λ measurements at different temperatures. Calculations by Kratzer and Scheffler reveal that multiple diffusing species exist, complicating this process [29].

Step Flow Growth

Surfaces usually have steps, which are preferred sites for incorporation of adatoms into the growing crystal. At high temperature the size of the critical nucleus for formation of new islands is larger and the average diffusion coefficient is also large, therefore the island number density is small. In addition, the average island separation may be much larger than the average terrace width. In this case adatoms will be captured by the steps [30]. The effect of preferred incorporation at steps is more pronounced if the steps are close together. When the diffusion length becomes longer than the average terrace width, almost all adatoms are incorporated at step edges. This mode is referred to as step flow growth.

2- D Island Nucleation and Growth

For an ideal surface without steps, adatoms arrive at the surface and diffuse around; nucleation happens when a sufficient number of adatoms meet each other. Islands grow by addition of further atoms until they coalesce. This process is similar to nucleation of a condensed phase from a supersaturated gas, which is described by thermodynamic nucleation theory [27]. The important concept in this theory is the critical nucleus, which is the free energy barrier that has to be overcome to reach the stable state and inversely is proportional to the supersaturation.

$$\Delta\mu = kT(\frac{P}{P_0}) \qquad (1.6)$$

Where the P_0 is the equilibrium vapor pressure and P is the effective pressure associated with the flux. For the growth at large supersaturation, the size of the critical nucleus may be on the order of atomic dimensions.

Layer by Layer Growth, Mound formation& Self-Affine Growth

When the atom diffusion length is smaller than the average terrace width the growth is via island nucleation. In the idealized case in which interlayer transport is perfect, all the atoms arriving on the surface are incorporated at island borders. The islands then coalesce, and the second layer will form via nucleation only when the first layer is complete. This is a *layer by layer growth.*

When the interlayer transport of the atoms is inhibited, the growth leads to mound formation [29]. In this case once the islands form, the atoms arriving to the top of them will form the second layer and consequently the third and the fourth layer will form. *Mound formation* leads to increasing the roughness of the surface. As it will be discussed in section 1.1.4, an anisotropic barrier to atoms attaching to steps from above and below has been suggested [18 -20, 31-33] as a mechanism for mound formation. At sufficiently low temperature diffusion is not effective and the adatoms will remain at the lattice site where they deposit. In this kind of growth the roughness increases during the growth. This can lead to *self-affine growth,* in which the surface topography looks essentially the same over a range of lateral and vertical length scales [34, 35]. Fig. 1.3 shows a schematic of the different above growth modes. Burton, Cabrera and Frank (BCF) analytically described the transition from 2-D island nucleation growth to the step-flow growth [36]. They calculated the dependence of the number of adatoms that reach the step from terrace width and diffusion length. However, this theory does not distinguish between adatoms that arrive at steps above and below.

As has been mentioned above, the ease of movement of atoms between layers affects whether layer-by-layer growth or the formation of the mounds occurs. The

movement of atoms between the layers; involves crossing the steps, therefore the actual crossing rate depends on the step morphology and step orientation as well as the presence of the corners and kinks.

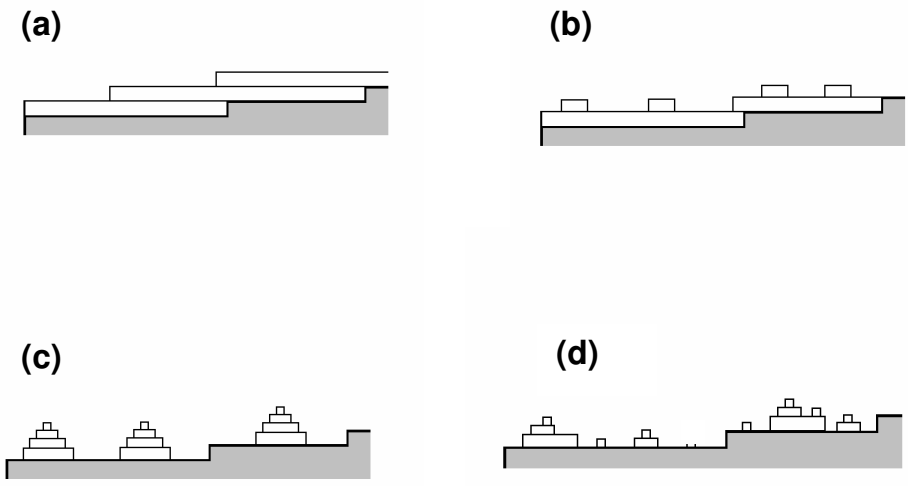

Fig. 1.3 Schematic of the different growth modes in homoepitaxy, (a) growth via step flow, (b) Layer by layer growth, (c) mound formation, (d) self-affine growth.

1.1.4 The Ehrlich-Schwoebel Effect

The Ehrlich-Shwoebel (ES) barrier leads to one of the kinetic instabilities which can occur during homoepitaxial growth. The presence of an extra barrier to adatoms crossing steps from above was first demonstrated experimentally by Ehrlich and Hudda in 1966 [31] through field ion microscopy. They observed diffusing tungsten atoms on terraces which appeared to be repelled by descending terraces. Schwoebel and Shipsey interpreted this observation as due to a change in potential barrier for an adatom which diffuses across the step edge [32, 33]. A schematic of such a barrier is shown in Fig. 1.4 A result of an ES barrier is that steps bounding different-width terraces move with different velocities over the surface during growth during step flow growth. If the

Schwoebel barrier is positive, i.e. as shown in Fig. 1.4, steps that bound large terraces from below move slower than the steps bounding it from above. As the result a uniformly stepped surface is stabilized during growth [18]; perturbing it by moving one step so as to create a short terrace followed by a long terrace causes the short terrace to "catch up".

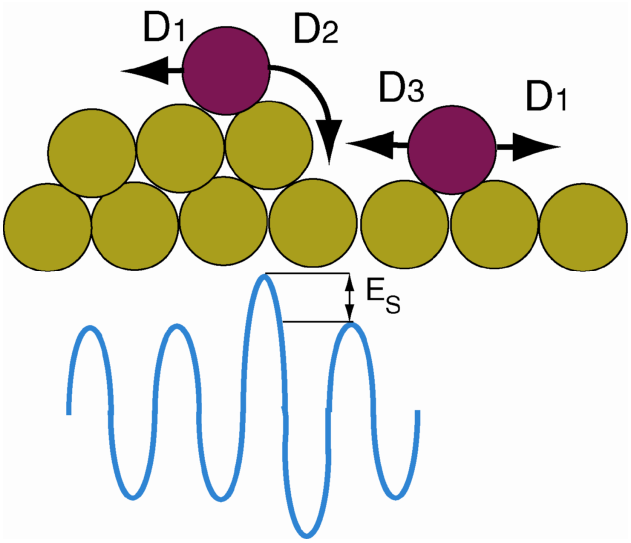

Fig. 1.4 Diffusion potential with positive Schwoebel barrier

Anisotropy in growth can occur because of anisotropy in the hopping barrier or in the sticking probability to steps of different orientations. Anisotropy in hopping barrier will affect the island shape, and in high symmetry surfaces it leads to formation of 3-D structures rather than layer by layer growth. On vicinal surfaces, if growth proceeds through the step flow mechanism, the ES barrier can lead to a second instability: a meandering of the steps [37].

Several authors have studied metal epitaxy and through observations of the nucleation rate on top of islands performed indirect evaluation of the Schwoebel barrier [38-42].The existence of this barrier in semiconductors is a very important but unresolved

question. For example for elemental semiconductors, this barrier might be able to explain the roughening of Si(001) surfaces before it becomes amorphous [43]. In the case of Ge (001) the barrier is found to be very weak [44]. For GaAs, Johnson, et al. suggested that mound formation during growth might be due to the existence of this barrier [18].

Finally even for the case where the ES barrier is very weak, it has been proposed that a cooperative multistep ES barrier for closely bunched steps might lead to observable effects [45].

1.2 Growth Techniques

Depending on whether species are transported physically or chemically from the source to the substrate, the various techniques of growing thin films in high vacuum can be divided roughly in two categories, physical transport or chemical transport. In physical deposition techniques (PDT), the compound to be grown or the constituent elements are vaporized from a polycrystalline or amorphous source and transported toward the substrate without any chemical changes.

In chemical deposition techniques (CDT), volatile species containing the constituent elements of the film to be grown are transported to the reaction zone near the substrate. Gaseous species undergo chemical reaction or dissociate thermally to form reactants which participate in the growth of the film on substrate. Thin films crystallize via reaction between the thermal-energy molecular beam or atomic beam of constituent elements and the substrate surface at ultra-high vacuum and elevated temperature. Relative arrival rates of the constituent elements and dopants determine the composition

of the growth epilayer and its doping level. Simple mechanical shutters in front of the beam sources are used to stop the deposition and doping.

MBE was developed in the early 1970's as a technology to grow high- quality epitaxial layers of compound semiconductors [46]. Since then, it has evolved into a popular technique for growing III-V and II-VI compound semiconductors, as well as other materials, such as oxides, silicon and germanium, metals and even insulators. Typical growth rates for MBE are 0.1-1 monolayer per second. It has the advantage of being able to produce artificial devices, superlattices or multilayer structures. MBE has been touted as producing high-quality single crystal layers with very abrupt interfaces, monolayer control of thickness, accuracy in composition precise and doping. Because of the perceived high degree of control and flexibility using MBE, it has been used extensively in fabrication electronic, magnetic and photonic devices.

MBE growth is carried out under conditions far away from equilibrium, using controlled fluxes in vacuum. It is governed mainly by the kinetics of the surface process that occurs during reaction of the impinging beam with the substrate surface. This is in contrast with other epitaxial techniques which proceed at conditions near thermodynamic equilibrium, like vapor phase epitaxy and liquid phase epitaxy. These processes proceed near thermodynamic equilibrium conditions and most frequently are controlled by diffusion processes occurring in the crystalline phase surrounding the substrate crystal.

The mean free path of gas molecules penetrating the vacuum and concentration of the gas molecules (number of molecules per unit volume) are two parameters related to pressure and important for characterization of the vacuum. Under conditions of ultra high vacuum (beneath approximately 10^{-9}-10^{-11} Torr) the mean free path for atoms is much

greater than physical dimensions of the vacuum chamber. Thus, the flux of evaporated material is referred to as a "beam" whereby negligible scattering occurs between the time at which an atom/ molecule leaves source material and that at which it reaches the substrate.

The use of ultra high vacuum is necessary to have minimal contamination during growth and to have molecular flow rather than viscous flow or diffusive flow. Another advantage of ultra high vacuum is that it allows a real time monitoring with RHEED (reflection high energy electron diffraction) as well as mass spectroscopy. In MBE chambers, the molecular beams are generated in effusion cells or introduced into the vacuum chambers through special gas inlets.

Evaporation cells are typically heated using resistive wire or foil heaters with thermocouple feedback and for monitoring however, ion gauges are normally used to monitor the fluxes. The molecular gases are produced by evaporating off the materials from their own locally shuttered crucibles or Knudsen calls. The growth rate depends on temperature at the time that shutter is open and the molecular flux controlled by (Knudsen cell temperature). The sticking coefficient of the type III species is approximately one, and the growth rate is determined by group III flux. Because of the high sublimation rate of As_2 from the substrate at temperatures higher than 350 ºC, an excess partial pressure of As_2 is needed over the GaAs substrate at higher temperatures. The materials grown by As_2 have different growth characteristics than As_4 [47].The flux of the Ga species is controlled by the Ga effusion cell temperature and the flux of As_2 is control by the valve position. The cracking zone is a heated tube which converts As_4 into As_2.

1.2.1 Quasi Equilibrium Description:

In spite of the departure from equilibrium corresponding to growth, it is still useful to think about the evolution of surfaces in terms of spatially varying chemical potentials. The equilibrium concentrations of the component atoms on the surface are determined by their chemical potential. In the case of gallium arsenide there are three chemical potentials to be taken into account. These are the chemical potential of bulk GaAs "molecules" ($\mu_{\text{GaAs bulk}}$), and the surface values of the chemical potentials of arsenic $\mu_{s\ As2}$ and chemical potential of gallium $\mu_{s\ Ga}$ at the surface. The chemical potential of the bulk GaAs is constant at a given temperature and pressure. However during growth the latter two can change on the surface. Their upper limit is given by the chemical potential of a bulk of the component, ($\mu_{\text{As bulk}} > \mu_{\text{As}}$), otherwise an arsenic crystal would form or, at the other extreme, gallium droplets will form.

In equilibrium, the following conditions should be satisfied,

$$\mu_{s\ Ga} + \mu_{s\ As} = \mu_{\text{GaAs bulk}} \qquad (1.7)$$

$$\mu_i = \left(\frac{\partial G}{\partial N_i}\right) T, P, N_j, j \neq 1 \qquad (1.8)$$

$$\mu_{\text{Ga vapour}} > \mu_{\text{Ga surface}} \geq \mu_{\text{Ga bulk}} \qquad (1.9)$$

$$\mu_{\text{As vapour}} > \mu_{\text{As surface}} \geq \mu_{\text{As bulk}} \qquad (1.10)$$

Growth involves raising the individual fluxes and thus vapor-phase chemical potentials above that of the bulk solid. This typically drives the surface out of equilibrium with the

bulk, however it is expected that during growth under As-rich condition on GaAs(001) surface the reconstructions are As rich, while under Ga-rich conditions, different reconstructions, which are Ga-rich are favored.

1. 3 Surface Reconstruction and Relaxation:

In many materials including some metals, rare gas crystals, or crystals of complex molecules, in which the binding forces are small compared to k_BT, or the components forming the crystal are large, the structure of the crystal surface is approximately the same as the bulk; such a surface is described as having *truncated bulk structure*. However, on nearly all ionic or covalent crystals the binding energies are quite high. Usually the atom arrangement at the surfaces of such crystals is not the same as in the bulk, and the atoms rearrange themselves to lower the surface free energy. The symmetry or the stoichiometry of the surface also changes from the bulk structure. This rearrangement is called a *reconstruction* and the structure is classified according to the dimensions of the surface unit cell with respect to the unit vectors that an ideally terminated bulk structure would have. On GaAs (001), under As-rich conditions, multiple reconstructions have been reported, including (2×4) and c (4×4). For semiconductor surfaces, reconstructions are driven by the high energy of broken bonds. In the bulk of a crystal atoms tend to have eight valance electrons in order to complete the sp outer most shell. In the case of GaAs, gallium can contribute three valence electrons, and arsenic can contribute five valence electrons. By symmetry there are four bonds to each atom in the zinc blend structure; one can simply say that gallium contributes 3 /4 electron and arsenic 5 /4 to each bond. On a surface, some of these orbitals have unpaired electrons

which are in *dangling bonds.* The atoms in GaAs are sp^3 hybridized. In the bulk, two hybridized orbitals combine to form a bonding and anti bonding orbital. At the surface some hybrid orbitals can not form bonds so that if reconstruction did not occur, partially filled dangling bonds would remain. This situation would be very unfavorable energetically and therefore dangling bonds are very reactive. Such a surface has a large free energy and reconstruction occurs to reduce this. For the surface which forms due to cleavage, a simple rehybridization of the dangling bonds sometimes occurs. The dangling bonds which correspond to a bonding orbital should be filled and those that correspond to an anti-bonding orbital should be empty. On most III-V and II-VI semiconductor surfaces (e.g. GaAs or ZnSe) there is a simple criterion for which dangling bonds are bonding and anti-bonding: Group V (VI) dangling bonds correspond to bonding orbital (they want to be filled), while group III (II) dangling bonds correspond to anti-bonding orbital (they want to get rid of their electrons). Therefore for GaAs, gallium dangling bonds are empty and arsenic dangling bonds are filled. This is the so-called *electron counting rule* [48]. Another way to fulfill this rule is to redistribute the electrons of the dangling bonds, which leads to a so called *relaxation*. The electron is usually redistributed between next neighbor atoms. The atom rearrangement may take the form of a simple compression, or more generally expansion of the atomic planes parallel to the surface as shown in Fig. 1.5.

Surface reconstruction is generally more complex, where the surface atoms relax normal to the surface as well as undergoing a rearrangement of the surface periodicity. If we consider a primitive surface mesh formed by a bulk termination of the surface which has basis vectors $\vec{a}$ and $\vec{b}$, and the reconstructed surface has primitive basis vectors $m\vec{a}$

and $n\vec{b}$, then the surface is said to have m × n reconstruction [49]. A c (m×n) or (centered) reconstruction has an additional mesh point at the center of the conventional (m×n) mesh.

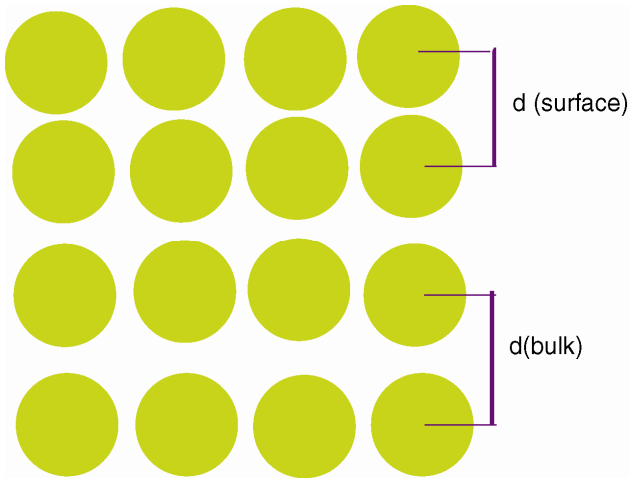

Fig. 1.5 Surface relaxation, the outermost atomic layer has shifted inwards to reduce the surface free energy.

1.3.1 Surface Reconstructions of GaAs(001)

For (001) surfaces of III-V semiconductors such as GaAs, $\vec{a}$ and $\vec{b}$ lie along the [110] and [$\underline{1}$10] directions respectively. Common reconstructions of these surfaces include (4×2), c (8×2), c (4×4), (2×4) and c (2×8). Then atoms must leave their normal places in order to form a reconstruction, which may lead to vacancies, single ad-atoms, dimers, or rarely also trimers and tetramers. (A dimer denotes a bond between two atoms on the surface, which move closer together compared to the bulk bonding arrangement.) The stability of a single crystal surface depends on having the right number of electrons per unit mesh, other factors like strain or the chemical environment also have effect on

surface reconstructions. They are all reflected in the surface energy. For different conditions different reconstructions can meet the criterion of minimum surface energy.

Surface reconstruction is a thermodynamic phase transformation, so it has dependence on thermodynamic variables such as temperature and adatom densities. The difference in energy between the different reconstructions is often very small and indeed several domains with different reconstruction may co-exist on the same surface [50].

On compound crystals the concentrations of the component atoms at the surface also have to be considered. This means that, for example, for GaAs (001) under arsenic rich conditions a reconstruction is favored which incorporates more arsenic atoms. The (2x4) reconstructions on GaAs(001) surfaces are the most investigated since they occur over a wide range of growth parameters. According to the brightness of the 2/4 streak along the fourfold symmetric axes it is possible to identify three different (2x4) phases, α, β, and γ. Fig. 1.6 shows the surface reconstruction models for different (2x4) reconstructions [1.51].The c (4x4) is the other type of arsenic rich GaAs(001) reconstruction. Ohtake et al. have reported that depending on the incident As molecular species there are two c (4x4) reconstructions. Under As_4, the reconstruction is c(4x4) and under As_2 is β(2x4) [52]. Fig. 1.7 shows the proposed atomic model of c(4x4) reconstructions.

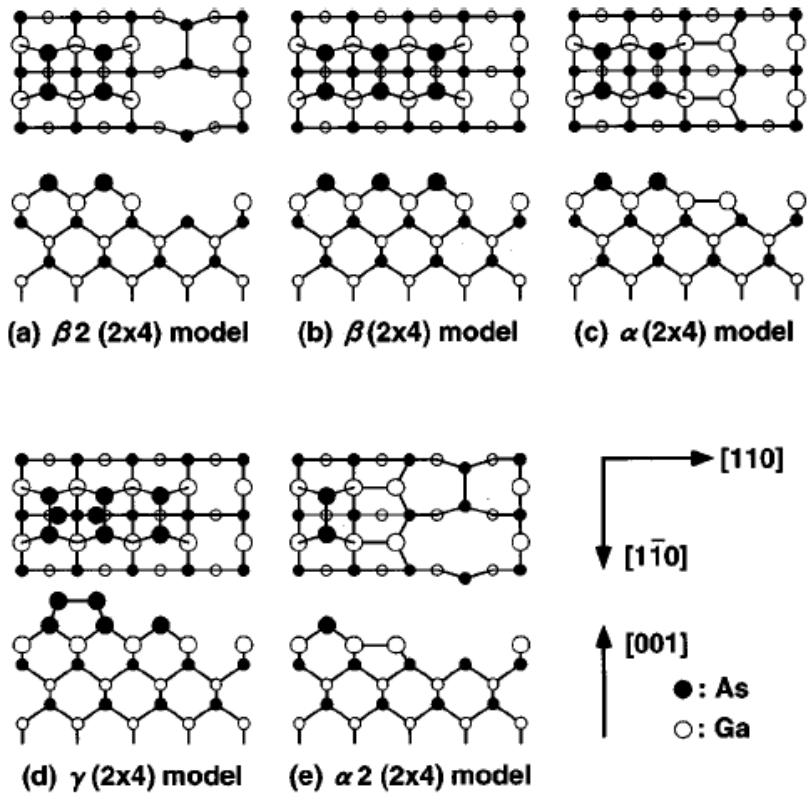

Fig. 1.6 Surface reconstruction model for GaAs(001) –(2x4(from ref [1.51))

It has been reported that by annealing the initial c(4x4) reconstructed surface, As_2 or As_4 desorption occurs; when the As coverage drops beneath approximately 1.75 monolayer the surface becomes rough as c(4x4) domains begin to disappear and the β_2(2x4) domains appears on the surface; the latter phase covers the surface at 0.75 ML [1.58], at which point the surface becomes smooth again [53].

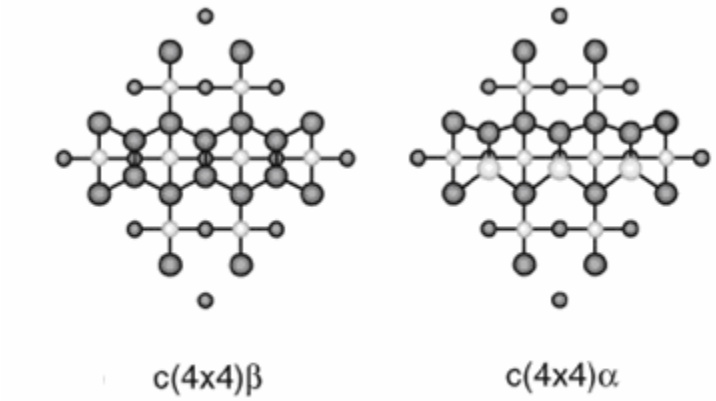

Fig. 1.7 Shows the different atomic arrangement for c(4x4) reconstructions, open circles denotes Ga and closed circles corresponds to As atoms (from Ref [52]).

Fig. 1.8 shows the STM image of each stage in the phase transformation from (2x4) to c(4x4) [53]. K. Kanisawa and H. Yamaguchi also reported that the diffusion length of the Ga species during the phase transformation is remarkably long and they estimated to be about the micrometer scale [54]. The inset in Fig. 1.8 shows proposed atomic arrangements for the different reconstructions [53].

The GaAs(001) surface is 2-fold, not 4-fold symmetric. As a consequence, the arrangement of atoms at steps descending along [110] and [$\underline{1}$10] are different, as are their free energies per length and sticking coefficient to them. Bell, et. al. refer to steps descending along [110] (or parallel to [$\underline{1}$10]) as type "A" and those descending along [$\underline{1}$10] (parallel to [110]) as type "B". Their STM images show that type-B steps predominate under typical growth conditions [55].

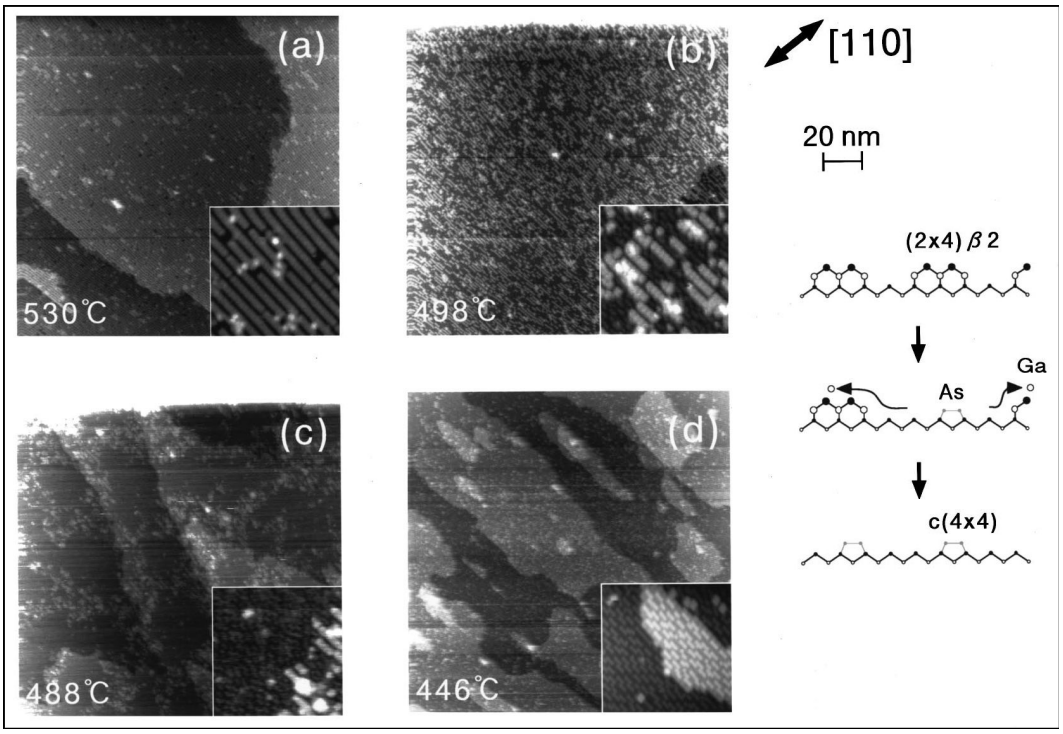

Fig. 1.8 Phase transformation from (2x4) to c(4x4) as the annealing temperature under As_4 flux is reduced. (a) β_2(2x4), (b) γ(2x4), (c) the phase in which only the c(4x4) is just observed on a RHEED pattern, (d) a c(4x4) phase. The filled STM images in each stage are in 20 nm x 20 nm scale. The inset shows the cross section of the β_2(2x4) and c(4x4). The filled circle is As and the open circle is Ga. (From Ref. [53]).

1.4 Reflection High Energy Electron Diffraction (RHEED):

Reflection High Energy Electron Diffraction is an in-situ method which is often used as a diagnostic in MBE growth. The glancing incident angle in RHEED makes this technique very sensitive to the surface [56]. An accelerated incident electron beam with high energy (5-100 keV) is incident on the surface with very small angle (< 3 degree). Upon reflection, electrons interfere and form a diffraction pattern. Although energetic electrons can penetrate deeply into materials, because of the glancing angle the sample region is typically only a few atomic layers. Fig. 1.9 shows the geometry employed in the RHEED [57].

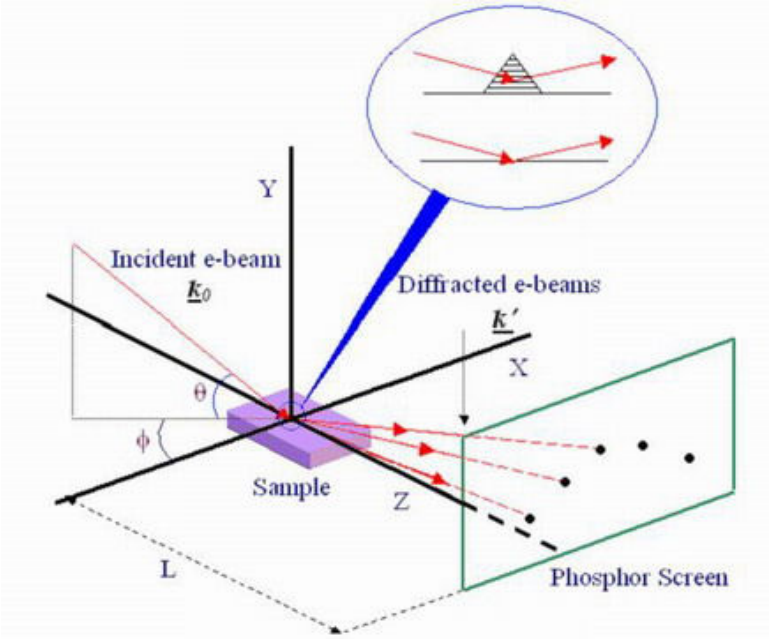

Fig. 1.9 Schematic of RHEED. inset shows two kinds of reflection: transmission-reflection diffraction scattering by three-dimensional crystalline island (top) and surface scattering from flat surface (bottom) [from Ref(57)].

The diffraction pattern is determined by the surface morphology and the atomic structure of the surface. A perfectly flat surface will result in a RHEED pattern which consists of the intersection of reciprocal lattice rods with the Ewald Sphere, i.e. streaks. However surfaces are not generally completely flat. The RHEED pattern for sufficiently short scale 3-D roughness represents a transmission pattern. Reflection and transmission-reflection can be distinguished from the resulting RHEED patterns. Reflection diffraction pattern consists of streaks or spots that lie on the Laue ring, while in transmission – reflection diffraction, discrete diffraction spots lie along straight lines.

1.5 Thermodynamic Surface Roughening and Preroughening:

An atomically flat surface at equilibrium and zero Kelvin should not have any steps. The step free energy is defined as:

$$F_{step} = E_{step} - T.S_{step} \qquad (1.11)$$

Here, E_{step} is the enthalpy of formation a step, S_{step} is the step entropy (mainly configurational), and T is the absolute temperature. With increasing temperature, formation of steps on a surface, while increasing the energy, also increases the configurational entropy. At any temperature, the equilibrium step density is determined by the balance between the energy cost to form steps (including step interactions) and the entropy, which is gained through the formation of steps.

As the temperature increases, the equilibrium step density also increases and at the transition temperature, the step density becomes unbounded [58]. Thermal roughening influences the surface at all length scales; at the microscopic scale the height fluctuations make the flat faces disappear from equilibrium crystal shape [58], and strongly influence various properties including the growth mode and chemical reactivity of the crystal surface. The roughening transition temperature depends on the surface orientation [58].

Low index surfaces, e.g. (001) or (111) of fcc metals remain smooth up to temperatures very close to melting [59] High index surfaces have lower roughening temperatures. There have been lots of studies on roughening, which have mainly been based on diffraction methods. The diffraction intensity can be compared to the Fourier transformation of the height-height correlation function,

$$G(\vec{\rho}) = \langle (h_i - h_j)^2 \rangle \qquad (1.12)$$

Where h_i is the height at site i and $\vec{\rho}$ is the displacement between the sites *i* and *j,* projected onto the average surface plane. The bracket denotes the ensemble average. At temperatures below roughening, the height-height correlation function should remain finite for all ρ, however above the roughening transition it should diverge logarithmically with ρ [58].

M. Den Nijs has predicted the possibility of an intermediate phase between the flat and rough phases which is called *"disordered flat"* phase. Here the surface remains flat on average although disordered array of steps are presents on the surface [60]. At the pre-roughening transition, the free energy of steps vanishes and the flat surface disorders though the formation of islands and / or pits. At a higher roughening transition the surface goes from disordered flat into a rough phase [61].

It has long been recognized [34 - 36] that growth can proceed most quickly in the presence of a supply of step edges to which diffusing adatoms can attach. It also known that at high enough temperatures many surfaces spontaneously roughen [58]. It is therefore reasonable to expect that roughening or preroughening might strongly affect growth.

1.6 Extrinsic or Non equilibrium Roughness:

In addition to thermodynamic roughness, "quenched-in roughness" can, and generally does exist on surfaces. It is often present due to the way in which a surface is prepared, for example in the removal of the oxide which covers the surface due to exposure to atmosphere.

The native oxide of GaAs is an amorphous layer of mixture of gallium and arsenic related oxide compounds and has to be removed prior to the growth. The desorption process of the GaAs oxide is a multi-step reaction due to the difference in thermal stability of each oxide compound. If the sample temperature is ramped upward, the first stage is the desorption of the volatile As-related oxide at temperatures below 400ºC. The second stage occurs in the temperature range of 400 ºC -500 ºC, where desorption of volatile Ga_2O-like oxide occurs. The final stage is the desorption of Ga_2O_3-like oxide at temperatures above 500 ºC. This is the most stable compound among the GaAs oxides. To desorb the Ga_2O_3 oxide a supply of Ga atoms is required; this comes from the substrate surface, and results in a roughened surface, with the formation of pits.

For Ga_2O_3-like oxide, the reaction can be considered as following [62, 63]:

$$Ga_2O_3 + 4GaAs\ (bulk) \longrightarrow 3Ga_2O\uparrow + 2As_2\ (or\ As_4)\uparrow$$

An alternative method to desorb the native oxide from a GaAs surface is to expose the surface with atomic hydrogen. This allows removal of the oxide at temperature as low as 300 ºC and produces a surface which is less rough [64, 65]. Atomic hydrogen is believed to convert both the oxides and hydrocarbons adsorbed on the surface into volatile species [66, 67]. The mechanism for atomic hydrogen assisted oxide removal for a GaAs wafer is thought to be the following [66-67]:

$$As_2O_x + 2\ x\ H^* \rightarrow x\ H_2O + As_2$$

$$Ga_2O_3 + 4\ H^* \rightarrow 2\ H_2O + Ga_2O$$

$$Ga2O3 + 4\ H \rightarrow H_2O + 2\ GaOH$$

A second form of extrinsic roughness can be created using lithographic patterning and etching [68-70]. We use this technique to perturb the nominally flat surfaces, and study the stability against such perturbations as the subject of this thesis, as presented below.

1.7 Models of Growth:

As we will show in Chapter 3, the unstable growth modes we observe can be used to discriminate between models of MBE growth. Making a comparison involves numerical simulations on the predictions of these models.

The atomistic process during growth that can be modeled depends on the time scales of interest. Theoretical models for evolution of surface morphology during the growth can be divided in three groups. In *Molecular Dynamics simulation,* one numerically integrates the classical equations of motion for each atom. In order to find the equation of motion, the forces have to be specified, which is obtained from the forces between the atoms. Molecular dynamics simulation can be done in fixed energy or fixed temperature, but the size of the system is typically limited to about 10^4 atoms.

Kinetic Monte Carlo simulations have been extensively applied to the evaluation of thermodynamic equilibrium properties or non equilibrium phenomena such as crystal growth. It can handle larger scale systems, but it is very time consuming and slow method.

1.7.1 Continuum Models:

Continuum equations are widely used to predict the surface morphology after growth [5, 18, 71, 72] on the mesoscopic or macroscopic height scale. One of the most

commonly employed continuum equations was proposed by Kardar, Parisi and Zhang (KPZ) [71]. They suggested that the growth happens locally and most quickly along the direction perpendicular to the interface. Therefore, a simple Taylor series expansion of the projected growth velocity in powers of the height gradient ∇h predicts that change in height with time will be given by,

$$\frac{\partial h(x,t)}{\partial t} = v\nabla^2 h + \frac{\lambda}{2}(\nabla h)^2 + \eta(x,t) \quad (1.13)$$

The first term in this equation is the smoothing via sublimation and condensation *(Edward and Wilkinson*). It could be interpreted as redistribution of the roughness on the surface in the way that the average height will not change. The second term is non-linear in ∇h. The last term is the noise, corresponding to instantaneous variations in the local incident flux. In this model the mass is not conserved because $(\nabla h)^2$ can not be written as the divergence of a current density.

A mass conserving form of the KPZ equation was proposed by Sun et al [5], it is also called the conserved KPZ or CKPZ equation. It has the form,

$$\frac{\partial h(x,t)}{\partial t} = -\nabla^2\left[v\nabla^2 h + \frac{\lambda}{2}(\nabla h)^2 \right] + \eta(x,t), \quad (1.14)$$

or,

$$\frac{\partial h(x,y)}{\partial t} = -\upsilon\nabla^4 h - \frac{\lambda}{2}\nabla^2(\nabla h)^2 + \eta(x,t) \quad (1.15)$$

The first term in this equation describes surface diffusion with a diffusion constant proportional to ν. The second term is again nonlinear, but has a form unlike that of KPZ. Its physical significance has been unclear until recently [73, 74]. The last term is again the noise, corresponding to instantaneous variations in the local incident flux.

A non-linear MBE equation with nearly the same form was proposed by Lai and Das Sarma [72] to explain evolution of the surface morphology during growth.

$$\frac{\partial h(x,t)}{\partial t} = \nabla^2\left(-\nu\nabla^2 h + \frac{\lambda}{2}(\nabla h)^2\right) + \eta(x,t) \qquad (1.16)$$

It differs from the conserved KPZ equation by a sign change in the nonlinear term.

Yet one more model, based on the Ehrlich-Schwoebel barrier was proposed by M. D. Johnson et al. [18], to explain the formation of mounds during homoepitaxial growth on GaAs(001). As discussed in section 3.2 this model accounts for the Ehrlich-Schwoebel barrier for an atom to hop downward across a step. The proposed height equation is:

$$\frac{\partial h}{\partial t} = -\nu\nabla^4 h - \nabla\cdot\left(\frac{\lambda\nabla h}{1+D(\nabla h)^2}\right) + \eta \qquad (1.17)$$

$$\frac{\partial h(x,y)}{\partial t} = -\nabla.\vec{j} + \eta(x,t) \qquad (1.18)$$

Here $\vec{j}$ is the adatom current density, and is a function of the local slope.

In section 3.2 we compare the predictions of these models with our experimental results for MBE growth on GaAs(001).

Chapter 2

Experiment

2.1 Design of patterning

We begin the experimental section with a description of the techniques employed in producing the patterned substrates used in our investigations of the stability of the GaAs(001) during MBE.

Our purpose in patterning the GaAs(001)substrates used in these studies is to observe how the surface corrugations evolve during growth as a function of their lateral length scale. The advantages of this approach are as follows:

1) Patterning allows probing the response of the surface roughness with well defined characteristic lengths built in to the initially patterned structure.
2) By patterning on the same surface with patterns of varying characteristic lengths, we perform multiple growth experiment on various patterned structure simultaneously, with maximum degree of control due to the high spatial uniformity of growth achieved with our MBE system.
3) The pattern serves as a navigation tool. With the patterned structure as a guide, and with the long range (~ $(4 \text{ inch})^2$) search capability from our atomic force microscope (AFM, DI dimension 3100), we can return to the same area for morphological characterization after each growth step.

Fig. 2.1 shows the mask we designed for patterning our initial surface for growth with photolithography. In the arrangement shown here, arrays in the same column have a constant center to center spacing, S, and those in the same row have a constant pit

diameter (D). The center to center spacing starts with 1.4 μm at the leftmost column, increases by factor of $\sqrt{2}$ for the next column on the right, and reaches 16.0 μm for the rightmost column. Pits in the bottom row have a diameter D equal to 0.7 μm. The initial pit diameter, D increases by factors $\sqrt{2}$ for the next and successive rows, and reaches 8.0 μm for the top row. This 2D array allowed us to study independently the evolution of the growing surface as a function of two different characteristic lateral length scales.

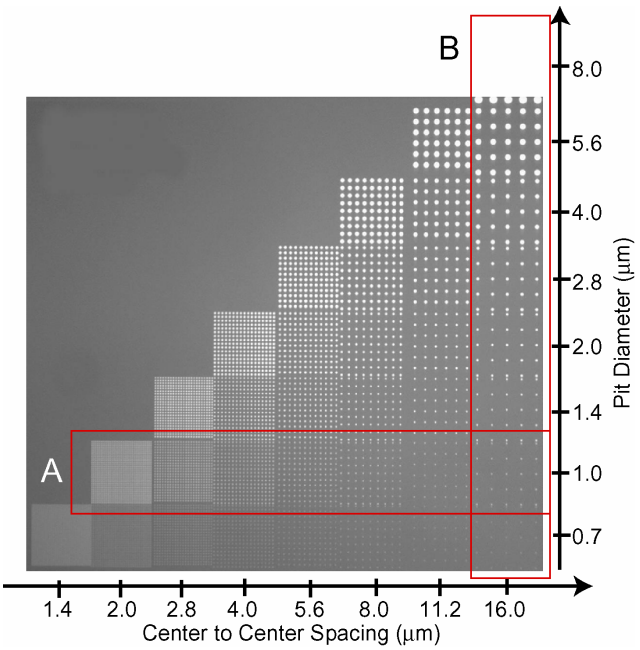

Fig. 2.1 Optical image of the mask used in fabrication of the patterned GaAs (001) surface. The demagnified spacing between the cylindrical pits and its diameter varies across the horizontal direction, from 1.4 μm - 16 μm (left to right, and in the vertical direction from 0.7 μm – 8 μm (bottom- to-top), respectively.

2.2. Patterned Substrate Fabrication:

2.2.1. Introduction

We create periodic arrays of our cylindrical pits (see Fig. 2.1) using photolithography on GaAs(001) substrates. A summary of the patterning process is shown in figure 2.2. The n-type GaAs wafers used in these experiments were two inches in diameter with thickness of 500 $\pm$ 25 μm and surface orientation of (001) $\pm$ 0.5º, supplied by American Crystal Technology (AXT).

All the processes described below have been done in a class 10 clean room to minimize the presence of particles on the surface. Impurity clusters act as nucleation centers for growth of rough structures or pinning of the steps during growth, which significantly affect the evolution of surface morphology. We have taken special care to remove all residues of the photoresist from the patterned surfaces, using multiple cycles of solvents and oxygen plasma etching. We examined the results by scanning the surfaces with AFM after each cycle to judge the results. This is repeated until all detectable resist has been removed.

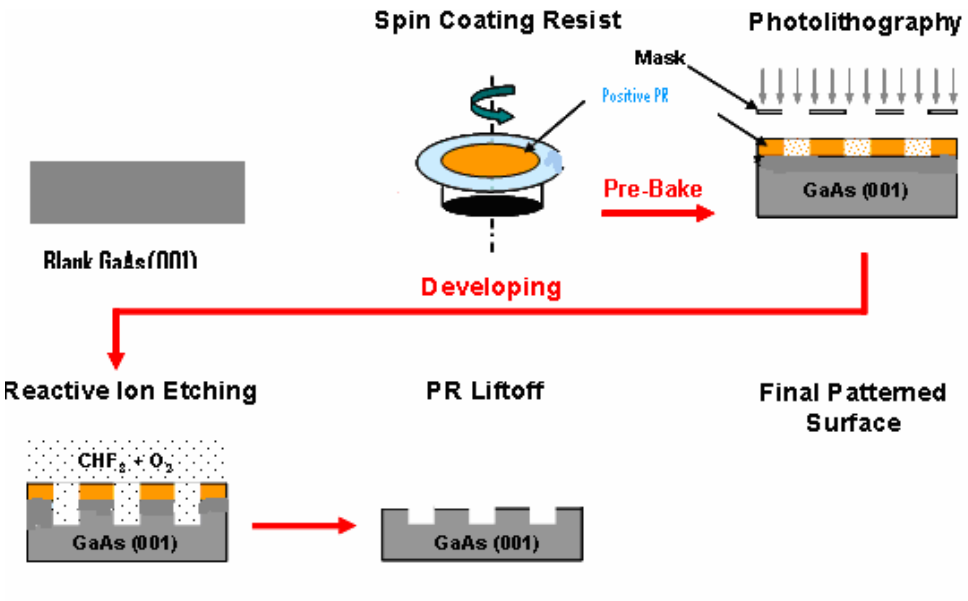

Fig. 2.2 Summary schematic of patterning steps for GaAs (001) wafers used in this thesis.

2.2.2 Photolithography:

We opted to use positive resist, for which regions exposed to UV light are subsequently removed during developing process. We based this choice on our experience that after patterning, it is easier to remove residual positive photoresist than negative photoresist.

Hexamethyldisilizane (HMDS), which acts as an adhesion promoter of the photoresist to the wafer, was first spun on the wafer at 6000rpm for 60 seconds. Next, several drops of positive photoresist (OIR-90610) from Futurrex INC were deposited on the wafer with a disposable pipette, and the wafer was then immediately spun at 6000 rpm, again for one minute. This spinning rate creates a fairly uniform film of photoresist with thickness of ~0.8 micron on top of the wafer. The wafer was then put on a hot plate

and pre-baked at 90 °C for 60 seconds to harden the photoresist and to enhance its adhesion to the wafer.

We used a GCA 200 ALS 5:1 stepper to expose the photoresist with 365 nm wave length UV light through the mask to transfer the pattern onto the resist. The optimum resolution of the stepper is nominally 0.5 μm. The optimum operating settings for the stepper, i.e. the focus and the exposure time were obtained by trial and error. For each trial, we expose the photoresist with a matrix identical pattern, for which both the focus setting and the exposure time were varied systematically. After developing the resist and transferring the pattern to the substrate by reactive ion etching, we removed the resist and measured the pit topography with atomic force microscopy (AFM). We search for the patterns that have dimensions closest to the desired values. We refined the exposure time and focus settings until we found the combination which produced pits of the desired diameters for all the patterns shown in Fig. 2.2.

After exposing the resist, the wafer was "post-baked" at 120 °C for 60 sec on a hot plate to further harden the photoresist for development. The exposed photoresist was removed with a resist developer (ODP 9646 from Futurrex Inc.) for 60 s. The sample was then rinsed with flowing Deionized (DI) water for approximately one minute to remove the residues of the developer, and then blown dry with dry nitrogen.

2.2.3 Reactive Ion Etching:

The next step in the patterned substrate fabrication process is transferring the pattern to the substrate using reactive ion etching. We chose a dry etching method which allows for anisotropic etching, resulting in pits with nearly vertical side walls. The

etching was done in a Plasmatherm RIE Model 790 system. The operating parameters for the process are given in table 2.1.

CHF_3 Gas	80 %
O_2 Gas	20 %
Pressure	40 mtorr
RF Power	175 W
Total time	9 mins

Table 2.1 Parameters for etching GaAs(001) in Plasmatherm reactive ion etching system

We further decided on an initial depth of approximately 50 nm, which is more than an order of magnitude larger than the root-mean squared amplitude of the uncontrolled roughness on the starting substrate surface. This required approximately 9 minutes of etching. However, continuously etching the resist leads apparently to overheating; the resist takes on a very dark appearance, and was very hard to remove. To avoid overheating the resist, we chose to etch the wafer in 12 cycles. In each cycle, we etched 45 seconds then waited for 3 minutes for the resist to cool down. After this multi-cycle etch procedure, we found that the resist was much easier to remove.

2.2.4 Sample Cleaning and Characterization:

After transferring the pattern to the substrate via RIE, we dissolved the resist with acetone, while agitating in a ultrasonic bath for 45 minutes. We then immersed the wafer in boiling (~80 ºC) n-methyl-2-pyrrolidone(NMP) for 30 minutes. The wafer was next

rinsed with a series of solvents: acetone, methanol, and isopropyl alcohol. Finally, we rinsed the wafer with flowing deionized (DI) water. This procedure removed the bulk of the photoresist on the wafer, however with AFM (Fig.2.3) we see that quite often there is still small amount of residue decorating the pit edges.

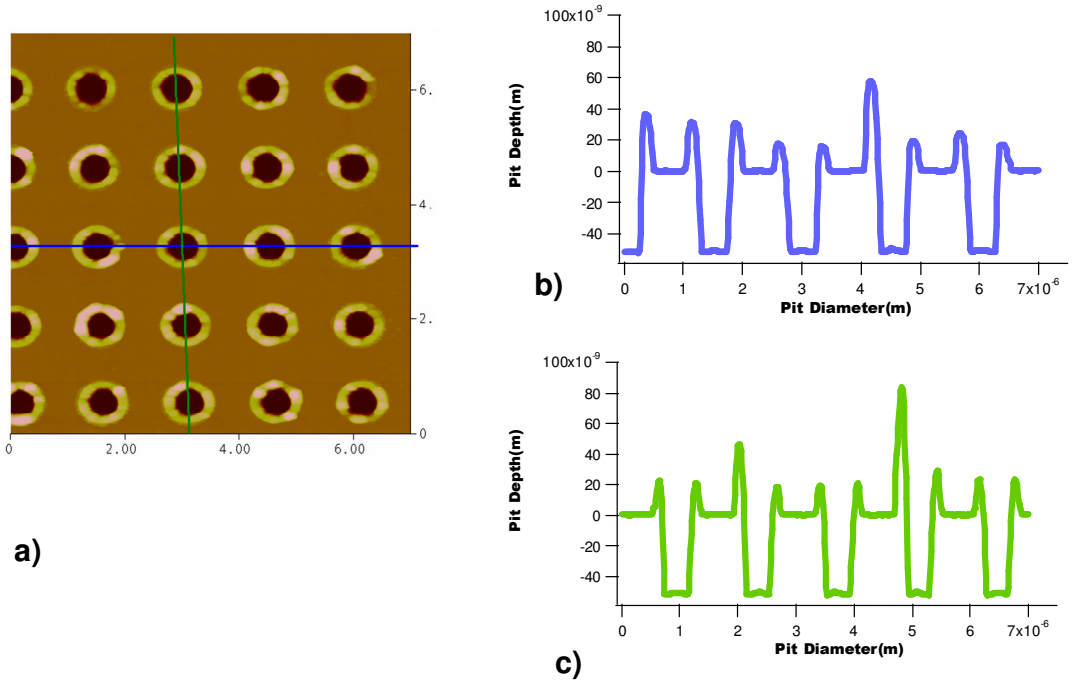

Fig. 2.3 (a) AFM image from patterned GaAs(001) after immersion within a series of solvents (see text), showing resist residue decorating the edges of the pits. (b), Line profile across the center of the pit structures shows the square profile of the pit shape and the depth of ~50 nm along[110], and (c) along [110].

Repeating the solvent cleaning process described above does not completely remove these residues. We found that in order to remove the residual resist completely, it was necessary to subject the wafers to oxygen plasma cleaning (Matrix System One Stripper Model 102) followed by very mild etching with buffered HF oxide solution

100:1(HF:NH4OH). After this the sample was again rinsed with acetone, methanol, isopropyl alcohol, flowing DI water, and blown dry with dry nitrogen. We found that cycles of the solvent rinsing and the oxygen plasma etching remove all residues to beneath the limit detectable in AFM imaging.

Fig. 2.4 shows an AFM image of a clean patterned surface prior to loading it into the MBE chamber. Such images were recorded for each cell before the MBE growth. More examples of such images are shown in figure 2.5.

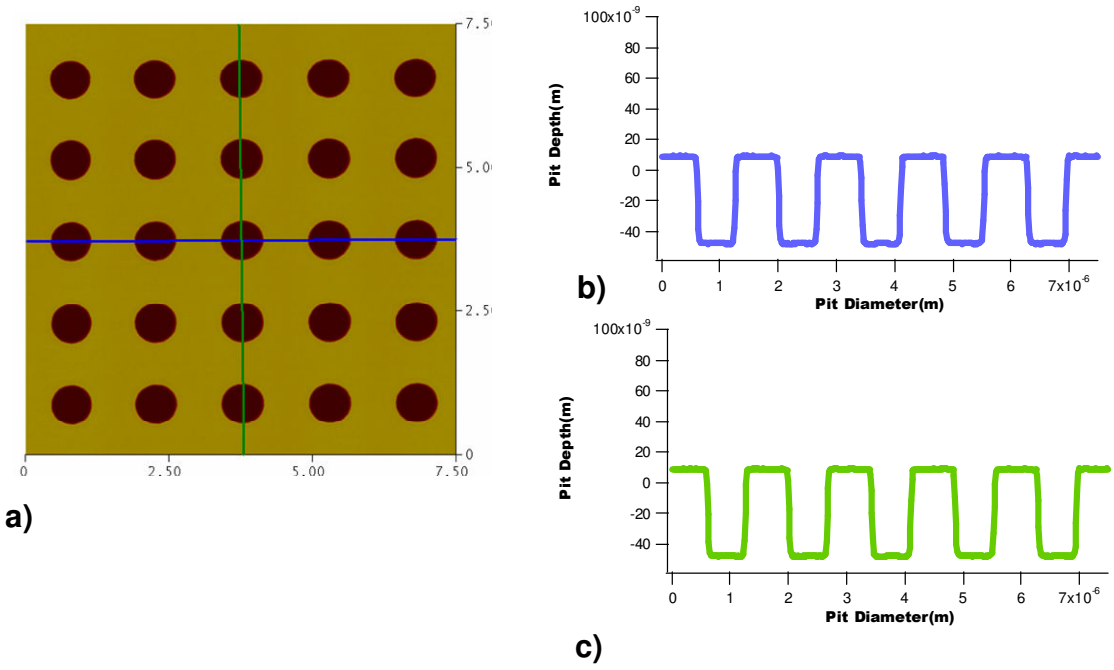

Fig. 2. 4 (a) AFM image from a patterned GaAs(001) surface after solvent cleaning and oxygen plasma cleaning,(b) Line profile across the center of the pit structures shows an approximately square wave profile and a depth of ~50 nm.

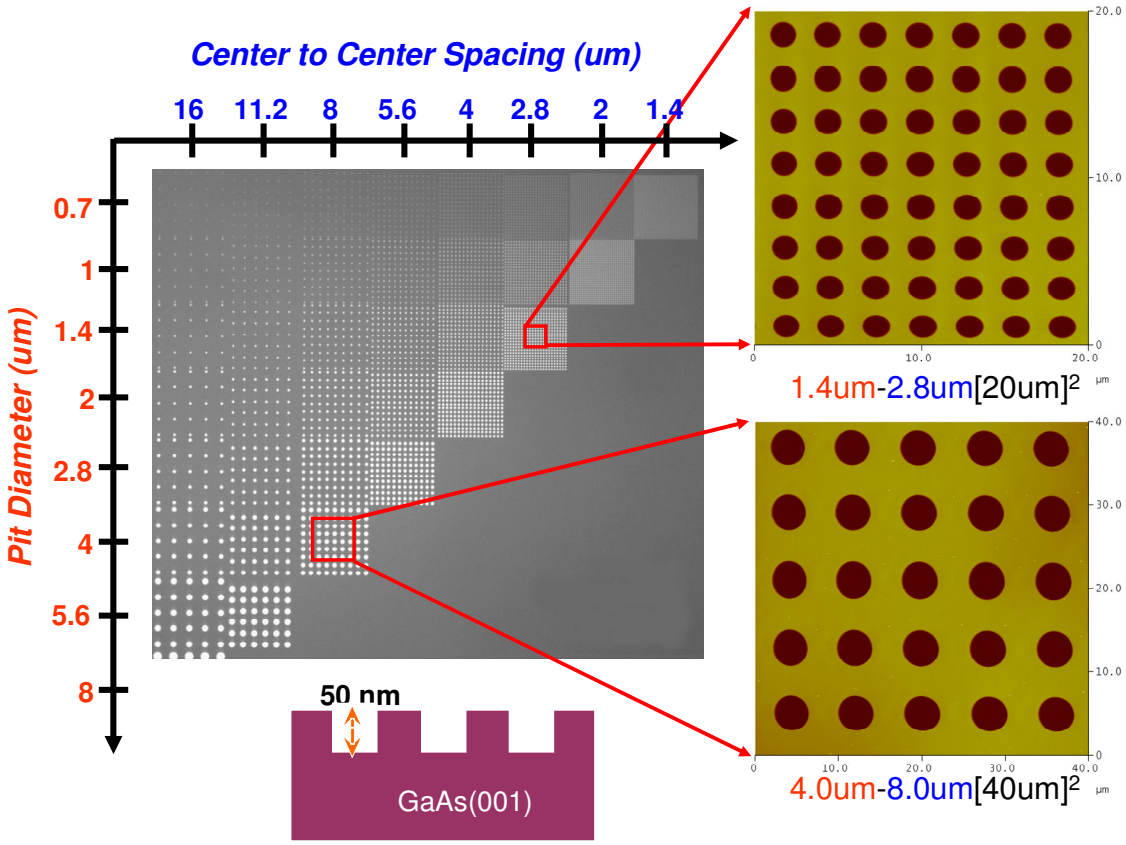

Fig. 2.5 GaAs(001) surface resulting from patterning of two areas; at top right a region with 1.4 µm pit diameter and 2.8 µm center to center spacing; at bottom right one with 4 µm diameter pits and 8 µm centre to center spacing. The initial depth of corrugation is ~50 nm.

2.3 MBE Experiments:

We next describe the procedures used in the final surface preparation and in MBE growth in these experiments.

2.3.1 Pre-Loading Preparation:

Prior to loading a wafer into the MBE system one final series of solvent rinses was performed. This consisted of a sequence of rinses, 3 minutes each, while agitating in an ultrasonic cleaner. The sequence of solvent was 1-1-1-trichloromethane (TCA) followed by acetone, methanol and isopropyl alcohol: A clean beaker used for each step. The sample was then rinsed with flowing DI water for 4 min and then blown dry with N_2.

2.3.2 MBE Growth Stations:

MBE growth was done in two different commercially available MBE growth systems. The first, which we refer to as deposition station C ("Dep C") is a EPI model 1040 system. It is capable of growing compounds based upon Ga, Al, As, N and Sb; with *in situ* atomic hydrogen capability, reflection high energy electron diffraction (RHEED), and residual gas analysis diagnostics. This station was used for some of the early growths. The majority of the work described here was done in a second station, referred to as "Dep A". It is a VG-80H MBE system with same sources for growing compounds based on Ga, Al, As, N and Sb. It also has *in situ* RHEED. For Dep A, the atomic hydrogen capability is available through another vacuum chamber ("Dep B") that is physically connected to Dep A.

After solvent rinsing, the sample was loaded into the introduction chamber of the MBE system through a load-lock system, and degassed for 12 hrs at 180 ºC at a background pressure of approximately 10^{-11} torr. Next, the sample was transferred into the preparation chamber ($P = 10^{-11}$ torr) where the second stage of degassing of the sample was carried out, typically for 30 minutes at 400 ºC.

Prior to growth, the beam equivalent pressures (BEP) of the As_2 flux and the Ga flux from the effusion cells were measured using an ion gauge located in the growth chamber; this was done while the sample was still in the preparation chamber. Once both the As_2 flux and Ga flux were calibrated to the desired settings, the sample was then transferred to the growth chamber for growth. For the growth, As_2 flux was used in excess so the growth rate was controlled by the Ga flux. The growth rate was fixed at 0.32 nm/second. Fig. 2.6 shows a schematic of the MBE and the etching chambers.

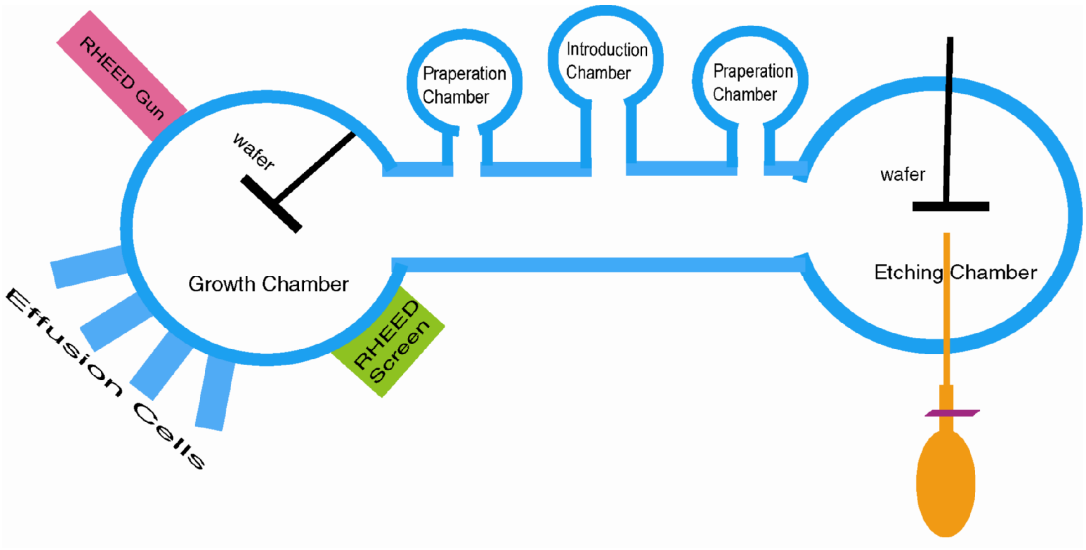

Fig. 2.6 Schematic drawing of the MBE growth and etching chambers.

2.3 Oxide Removal:

As was described in chapter 1, the native oxide on the substrate must be removed prior to the growth. This can be done in two ways, desorption by heating to ~600˚C or desorption while heating to ~300˚C in the presence of atomic hydrogen. In our experiments we desorbed the oxide layer thermally under As_2 flux at temperatures of approximately 630 ºC. Desorption of the oxide was monitored using RHEED. As the oxide was removed the RHEED pattern was observed to develop diffraction streaks, which is characteristic of an ordered GaAs(100) surface.

Fig. 2.7 shows examples of our RHEED patterns for a GaAs(001) surface after removing the oxide layer for the electron beam incident along the [$\underline{1}$10] and [110] azimuths.

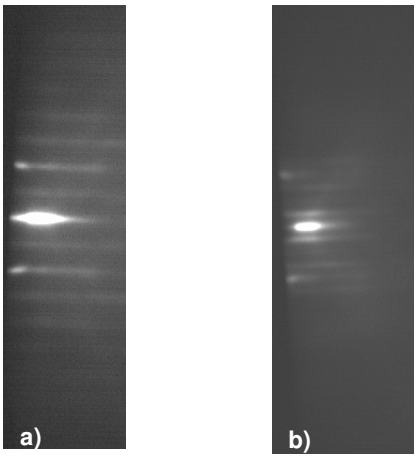

Fig. 2.7 Reflection high energy electron diffraction (RHEED) patterns from un-patterned GaAs(001) surface after removing the oxide thermally at 630 ºC (a) pattern measured with incident electron direction, projected onto (001), along [$\underline{1}$10]. (b)) pattern measured with incident electron direction, projected onto (001), along [110].

The surface after oxide removal was scanned with AFM in air. Figure 2.8 shows that the surface is rough, and is decorated with pits; the root mean squared (RMS) amplitude of the roughness is 0.95 nm.

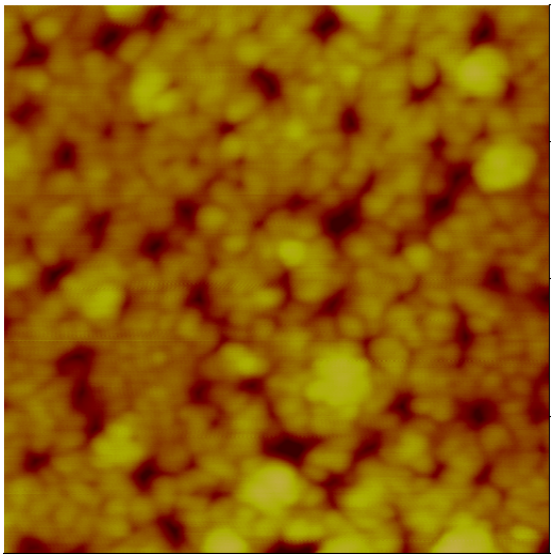

Fig. 2.8 AFM images from GaAs(001) surface after desorbing the oxide by heating in vacuum to 620 ºC. This leads to formation of pits, and RMS roughness of 0.95 nm. Field of view is 1 μm x 1μm.

Removing the oxide at lower temperature in the presence of atomic hydrogen gives us a smoother starting surface. In order to carry this out experimentally I transferred the wafer to the etching chamber and stabilized an atomic hydrogen flux over the wafer surface with the ion gauge reading indicating a pressure of 1.1×10^{-6} torr. I slowly ramped the substrate temperature up to 300 ºC and kept the wafer at that temperature for about 40 minutes.

As noted above, I used the formation of streaks in the RHEED pattern as an indication that the oxide layer had been removed. Fig. 2.9 shows that the surface resulting

from removing the oxide in the presence of atomic hydrogen is much smoother than removing the oxide at higher temperature, without atomic hydrogen.

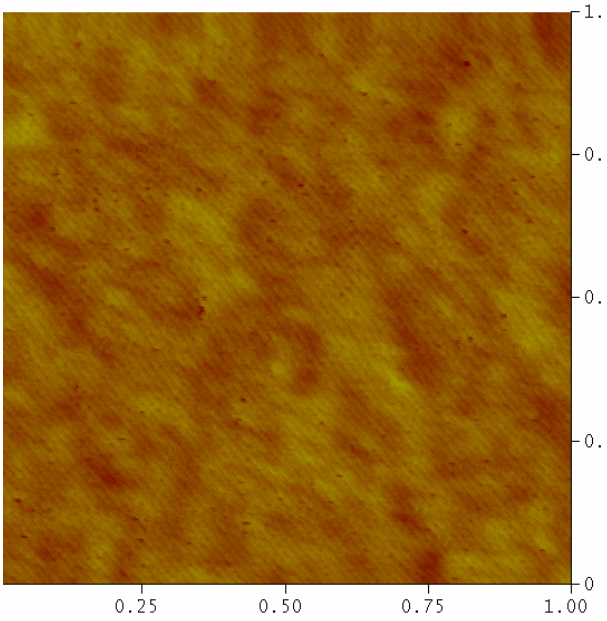

Fig. 2.9 AFM image of a GaAs(001) surface after desorbing the oxide at T~300 ºC, in the presence of atomic hydrogen. The RMS roughness is ~0.15 nm. Field of view is 1 µm x 1 µm. 3 nm in height corresponds to full scale.

2.3.3 Annealing and Growth Experiments:

In the work described in this thesis, I carried out two types of experiments: (1) annealing of un-patterned GaAs(001) and (2) homoepitaxial growth of GaAs on patterned GaAs(001) substrates.

In first case the goal was to determine to the preroughening onset temperature as a function of As_2 flux. In this experiment I desorbed the oxide at ~300 ºC while exposing

the surface to atomic hydrogen, followed by growth of a buffer layer ~0.4 μm in thickness. I then annealed the surface at different temperatures and As_2 fluxes for an extended period of time (1~2 hour).

I performed growth of GaAs on patterned GaAs (001) at different temperatures spanning the pre-roughening onset temperature and for different growth duration. After each experiment the evolution in morphology was characterized using tapping mode AFM in air.

2.3.4 Surface Reconstruction:

In addition to the AFM images presented in this thesis, Ialso recorded the RHEED pattern along different crystalline directions before, during and after growth. In order to get good quality RHEED patterns, I desorbed the oxide thermally and we grew a 0.4 μm buffer layer. Then I annealed our surfaces at 585 ºC for one hour. I recorded the RHEED images along [110], [$\underline{1}$10] and [100] crystalline directions once we change the temperature and As_2 pressure. From this I determined the surface reconstruction. Results are discussed in section 4.2.3.

Chapter 3: Evolution of the Patterned Surface Far Above the Onset Temperature

3.1 Experimental Results:

In this section, we present a systematic experimental study of the transient evolution of the surface corrugation during growth and its length scale dependence. We have published these results previously elsewhere [73, 70, 2] It had been reported by other investigators that initial morphology has a profound effect on the evolution of the surface morphology during growth [73, 70]. In particular, Ballestad et al. [10] found that the formation of "growth mounds", attributed by Johnson, et al. [18] to an extra diffusion barrier toward atoms crossing steps from above (the Ehrlich-Schwoebel barrier [31, 3.2, 33]) was in fact a transient response to pre-existing roughness on the GaAs(001) substrate. As a result the initial surface morphology is a crucial part of the control of the experiment. Typically growth or etching experiments are done on nominally flat surfaces, where random roughness itself is the subject of study and comparison to theory [64, 10, 18]. We adopted a different approach, following the evolution of the amplitude of a well-defined pattern during growth in order to characterize the lateral length scale dependence of the transient response of the growing surface to existing corrugations. For this we used the mask shown in Fig. 2.1 to pattern our GaAs(001) surfaces. The lateral size of the features and the repeat period of the structure are varied independently. This amounts to a combinatorial approach, and it allows us to investigate the dependence of the response of the surface during growth on these two different characteristic distances. In these studies we measure the topography of the starting substrates, and the surfaces resulting from the growth of

films of various thicknesses using standard conditions of temperature (585 ºC) and flux (~0.3 nm /s, P_{As2} / P_{Ga} = 10:1) with atomic force microscopy in tapping mode.

3.1.1 Evolution of the Patterned Surface vs. Spacing at Constant Pit Diameter:

We first examine the evolution of pit-patterned GaAs(001) surfaces at fixed pit diameter, D=1 μm, as a function of the center-to-center spacing. Fig. 3.1 shows two AFM images of the surface structure prior to the growth. The average initial depth of the pits is approximately 50 nm.

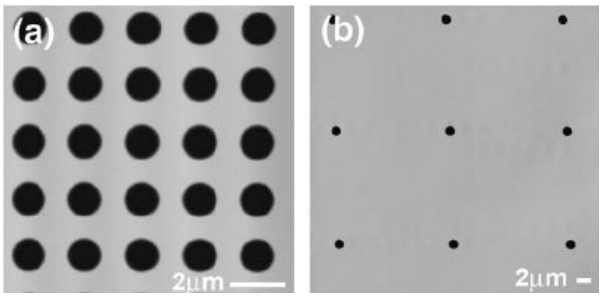

Fig. 3.1 AFM images of regions of a patterned GaAs (001) surface, prior to growth. (a), D=1㎛, S=2㎛; (b), D=1㎛, S=16㎛.100 nm gray scale.

We transferred this substrate into the MBE growth chamber, desorbed the oxide, and deposited in steps of 100 nm of GaAs using the growth condition described above. Fig. 3.2 shows corresponding AFM images of the same regions of the surface subsequent to growth.

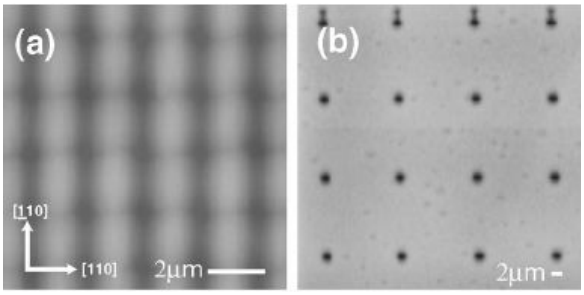

Fig. 3.2 AFM images of patterned GaAs(001) surface shown in Fig. 1 after 1000 nm thickness of growth. Pit diameter and center-to-center spacing for (a), (b) are identical to those indicated in Fig. 1(a), 1(b), respectively. 30 nm gray scale.

These images reveal a pronounced dependence of the evolution on the center-to-center spacing of the pits. In figure 3.2(a), for a spacing of twice the diameter, there is a strong coupling between neighboring pits, as well as anisotropy, resulting in a modulated columnar structure along the [1̄10] direction, whose period is equal to that of the initial pattern. We point out that the substrates are rotated in azimuth continuously during growth; the anisotropy in the evolution rate between the [1̄10] and [110] direction seen here is mainly due to the anisotropic adatom diffusivities on the reconstructed surface and the orientation dependence of the attachment rates of adatoms to atomic steps [55, 75, 28, 76]. At the largest spacings studied, each pit evolves independently as shown in figure 3.2(b); the major change in the image with growth is a blurring of the pit edges.

Examination of height profiles, measured across the centers of rows/columns of pits provides a more clear understanding of the evolution of the topography during the growth. Figure 3.3 shows two series of such profiles, measured along both the [1̄10] and [110] crystalline directions for layers of increasing thickness grown onto the patterned areas shown in Figs. 3.1. Height profiles at small spacings measured along [110], Fig. 3.3(b), initially show an evolution from an approximately square-wave shape into nearly

sinusoidal curves, quite similar to what might be expected for a diffusion-like relaxation. Comparing the panels of profiles at the left of Fig. 3.3 with those at the right illustrates dramatically the anisotropy in the evolution of the corrugation amplitude: it occurs faster along [$\underline{1}$10] than in the [110] direction, providing insight into the formation of the grooved structure shown in Fig. 3.2(a).

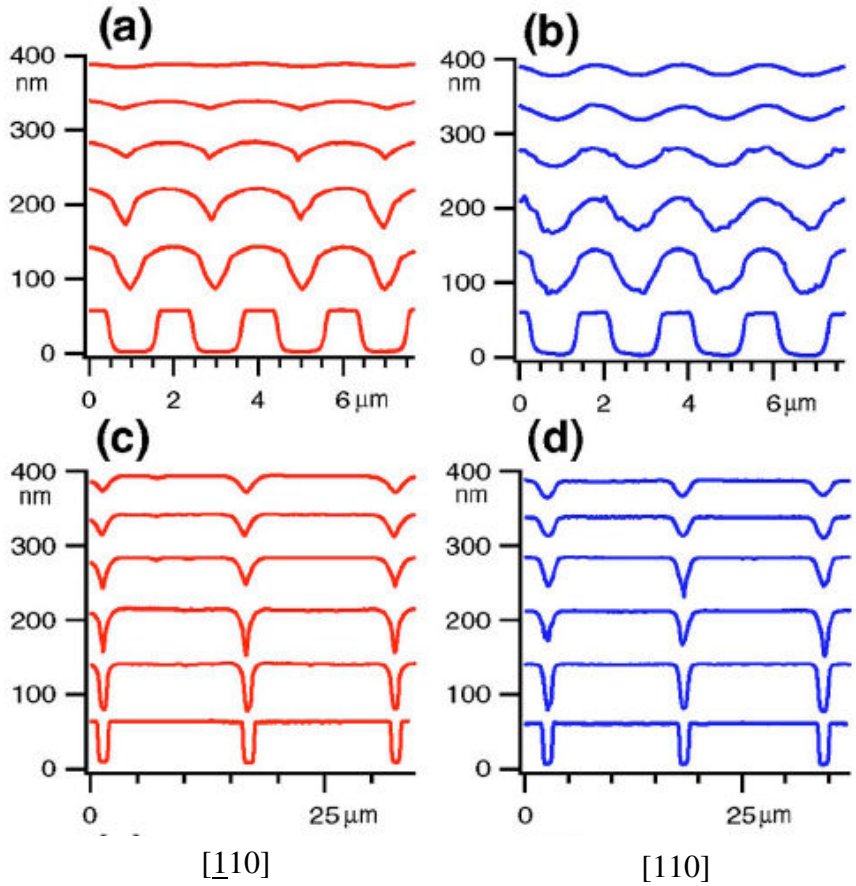

Fig. 3.3 Line profiles measured across pit-centers after growth of progressively thicker GaAs layers. Line profiles in (a) and (c) are scanned along the [$\underline{1}$10] direction, and those in (b) and (d) are scanned along the [110] direction. Line profiles in (a) and (b)are from the areas shown in Fig. 3. 2(a); D=1μm, S=2μm; (c) and (d) from Fig. 3.2(b), D=1μm, S=16μm. In each panel the bottom profile is the initial surface, and the thicknesses of the growth for successive profiles are 100, 200, 300, 500, and 1000 nm, respectively.

As shown in panel 3.3(a), for the smallest spacing, soon after growth starts, cusps form at the center of each pit in profiles along the [$\bar{1}$10] direction. The cusps persist through the growth, and the rounded regions between pits eventually extend all the way to the pit center on both sides. The profiles after 300 nm of growth consist of series of concave downward parabolas intersecting at cusps.

The coupling of the evolution of neighboring pits is clearly evident at the smaller spacings from the finite curvature between them, while at the larger spacings the profiles are flat topped. During the growth, cusps form at pit centers in profiles along the [$\bar{1}$10] direction while smoothly varying topography forms at the pit bottoms in the [110] direction. It is this rounding of the pit edges which produces the blurring of the pit edges seen in figure 3.2(b). Significantly, the amplitude of the line profiles increases slightly [73, 70] after the first 100nm growth, and then decays with further growth.

Figure 3.4 summarizes the spacing dependence of the evolution of the amplitude of the surface corrugation for a fixed diameter of 1 μm. The depths are in each case normalized to the initial pit depth. The amplitude of the corrugation evolves at a faster rate for patterns for $S < 4$ μm, where coupling between neighboring pits is strong. For patterns with $S \geq 4$ μm, the amplitude of the corrugation initially increases, then decays at a nearly uniform, but slower rate. We find that the coupling is significant beneath ~ 4 μm, which gives us a rough measure of the distance over which atoms diffuse on the surface under our growth conditions; i.e. (S-D)/ 2~1.5 μm.

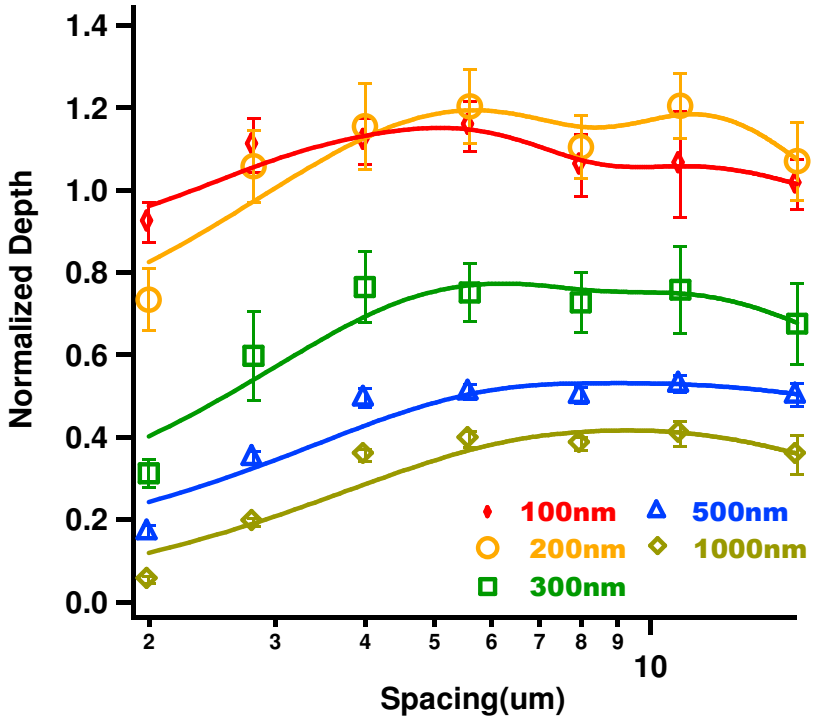

Fig. 3.4 Summary plots of the normalized pit depth measured from line profiles, along the [$\underline{1}$10] direction, as a function of longer characteristic dimension, i.e. center-to-center spacing. The individual curves are for different layer thicknesses, indicated in the key. Normalized pit depth plotted as a function of spacing at a fixed diameter D=1μm.

3.1.2 Evolution during Growth vs. Initial Pit Diameter at Constant Center-to-Center Spacing:

Next we examine the variation of the evolution of the surface corrugation as a function of the second characteristic lateral length scale illustrated in Fig. 2.1; i.e. the variation with initial diameter at a fixed center-to-center spacing of 16 μm. Fig. 3.5 shows the initial patterned surfaces and Fig. 3.6 shows the surfaces after 1000 nm thickness of growth.

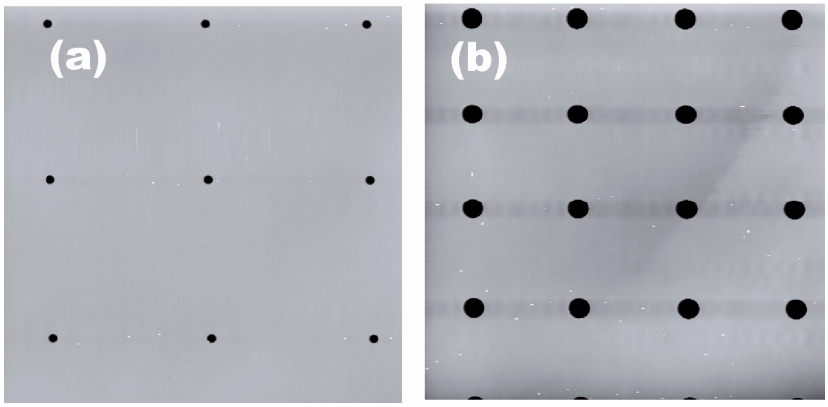

Fig. 3.5 AFM images of regions of a patterned GaAs (001) surface, prior to growth. (a), D=1 μm, S=16 μm; (b), D=2.8 μm, S=16 μm. The horizontal dark bands between the pits in both are artifacts. 100 nm gray scale.

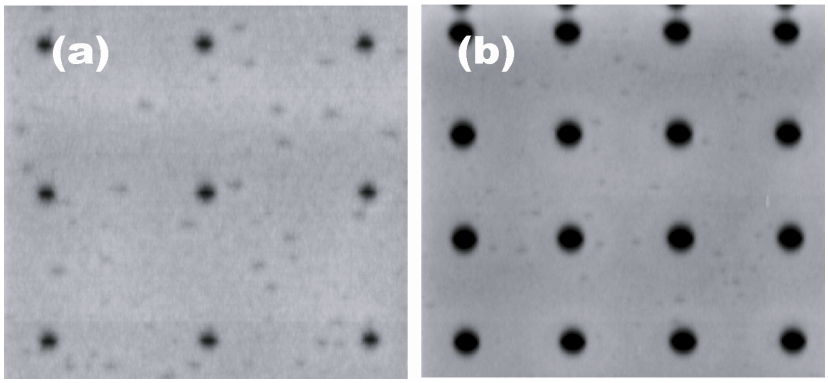

Fig. 3.6 AFM images of patterned GaAs(001) surface shown in Fig. 3.5 after 1000 nm thickness of growth. Pit diameter and center-to-center spacing for (a), (b) are identical to those indicated in Fig. 3.5(a), (b), respectively. 30 nm gray scale.

As Fig. 3.6(a), (b) show there is no evidence for coupling between the pits. The effect of growth is simply a blurring of the edges. The results of height profiles extracted from the AFM images are presented in Fig. 3.7, again along both [$\underline{1}$10] and [110] crystalline directions, and at a series of increasing grown layer thicknesses. Line profiles measured along both crystalline directions remain flat topped between the pits during growth. In panel 3.7(a) for a pit diameter of 0.7 μm, cusps quickly form at the center of the pits in

profiles along [1̄10] direction and persist throughout further growth. Along [110] direction (3.7(b)) the line profile develops smoothly varying pit bottoms as growth continues. Contrasting behavior is observed when the pits are significantly larger; here the trenches initially appear at the bottom of the pits near the wall edges due to formation of growth mounds [10, 18] near the pit centers. These persist, but move inward and eventually coalesce to form single cusps at the center of the pits in profiles measured along [1̄10] direction (Fig. 3.7(c)).

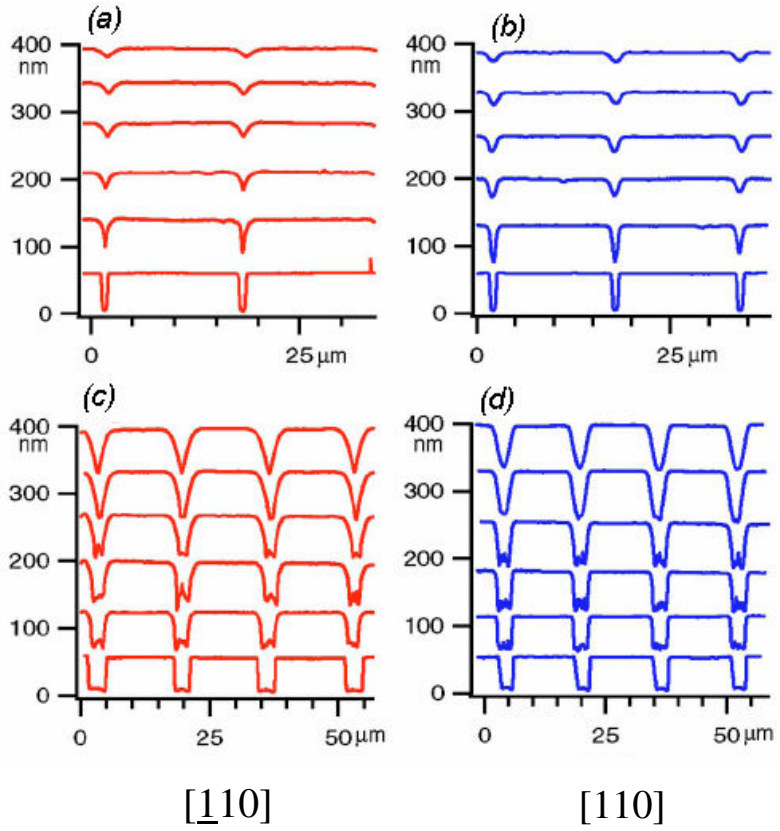

Fig. 3.7 Height profiles measured across pit-centers after various stages of GaAs growth for a fixed center-to-center spacing of 16㎛, but variable initial diameter. Line profiles in (a) and (c) are scanned along the [1̄10] direction, and those in (b) and (d) are scanned along the [110] direction. Line profiles in (a) and (b) are from the area D=0.7㎛, S=16㎛; (c) and (d), D=2.8㎛, S=16㎛.for initial patterned surface and 100 nm, 200nm, 300nm, 500 nm and 1000 nm growth thickness

Coalescence of trenches along [110] again leads to rounded pit bottoms in line profile. For the line profiles shown in Fig. 3.7(c) and 3.7 (d), an initial increase of amplitude during the growth is observed.

A quantitative examination of the sequence in which the pit diameter is varied reveals a quite different trend from that for variable spacing.

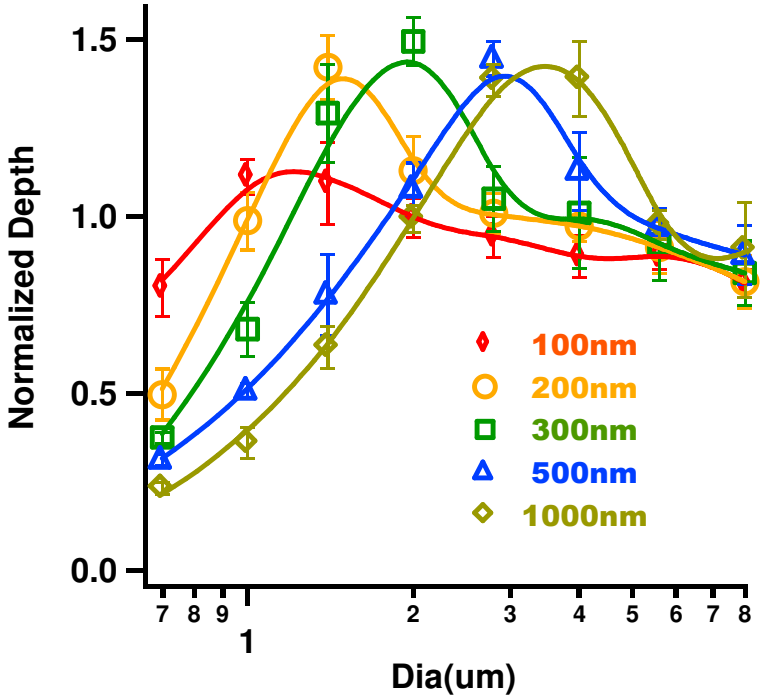

Fig. 3.8 Summary plots of the normalized pit depth as a function of the initial pit diameter at a fixed center to center spacing S=16 μm. The individual curves are for measurements after growth of layers of increasing thickness, as indicated in the key. Values measured from line profiles along [1̲10] direction.

A summary, for patterns with a fixed spacing of 16 μm, is shown in Fig. 3.8. It shows that after each growth step the normalized amplitude evolves with a non-monotonic dependence on initial diameter; there is a maximum in the corrugation amplitude which moves toward larger values of initial diameter with growth. Physically, this maximum separates regimes of corrugation amplification and decay. For the smallest growth

illustrated here, patterns with D$\leq$ 1.2 μm, further growth smoothes the surface. Beyond this maximum the corrugation amplifies. The amplification is transient; further growth shifts the maximum to larger diameters and once the maximum shifts and past the initial diameter of a given pattern, further growth results in a relaxation of the amplitude.

3.1.3 Evolution during Growth vs. Initial Pit Diameter at Constant Spacing/ Diameter Ratio:

For comparison in this section we review the evolution of the surface for a third case, described by Shah [2, 77] for which we change the initial pit diameter and center-to-center spacing in such a way that ratio is fixed at 1:2. In Fig. 2.1, this corresponds to pattern cells which lie along the main diagonal. The results, again in the form of the normalized depth are shown in Fig. 3.9 the behavior is nearly identical to that seen for the fixed center-to-center spacing case illustrated in Fig. 3.8.

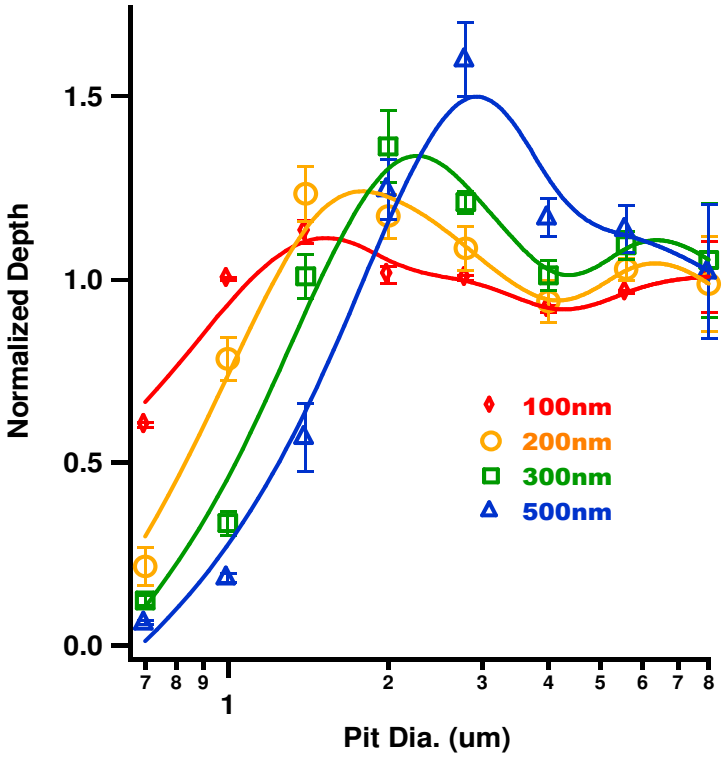

Fig. 3.9 Surface corrugation amplitude, normalized to the initial value as a function of initial diameter D for a fixed spacing/diameter ratio S/D = 2:1. The individual curves are for measurements after growth of layers of increasing thickness, as indicated in the key. Determinations from height profiles measured along [1̲10] direction are shown.

Again, after each growth experiment, the length scale dependence of the amplitude shows nonmonotonic behavior, with a maximum corrugation at a diameter which shifts toward larger values as growth continues. The similarity of this behavior to that of the extremely weak coupling limit, illustrated in Fig. 3.8, indicates that it is the smaller of the characteristic length scales (the initial diameter) which dominates the evolution. This is perhaps not so surprising, in that mass transport processes such as diffusion occur most quickly at shorter distances. There are quantititative differences, presumably associated with pit coupling at spacing < 4 μm: the height of the maximum

drops at smaller diameters for the strongly coupled case of Fig. 3.9, but is nearly constant in the weakly coupled case of Fig. 3.8.

Fig. 3.10 summarizes the thickness / time dependence of the normalized surface corrugation and its variation with spacing and with diameter. Fig. 3.10(a) is for a fixed pit diameter of 1 μm, with each curve corresponding to a particular spacing. The evolution of the amplitude with thickness approaches a spacing-independent form for spacings greater than ~5.6 um. In the large spacing limit, the normalized amplitude reaches a peak which is ~20% larger than the initial value by 200 nm of growth; beneath this the corrugation amplitude increases, while beyond this the amplitude decays. The rate of decay rolls off with increasing thickness, with an inflection point at ~300 nm for large spacings. In the opposite limit, for the smallest spacing (2 µm), no increase of amplitude with growth is evident for the thinnest layer grown in these experiments; the inflection point which marks the roll off in amplitude decay shifts down to ~200 nm in this strongly

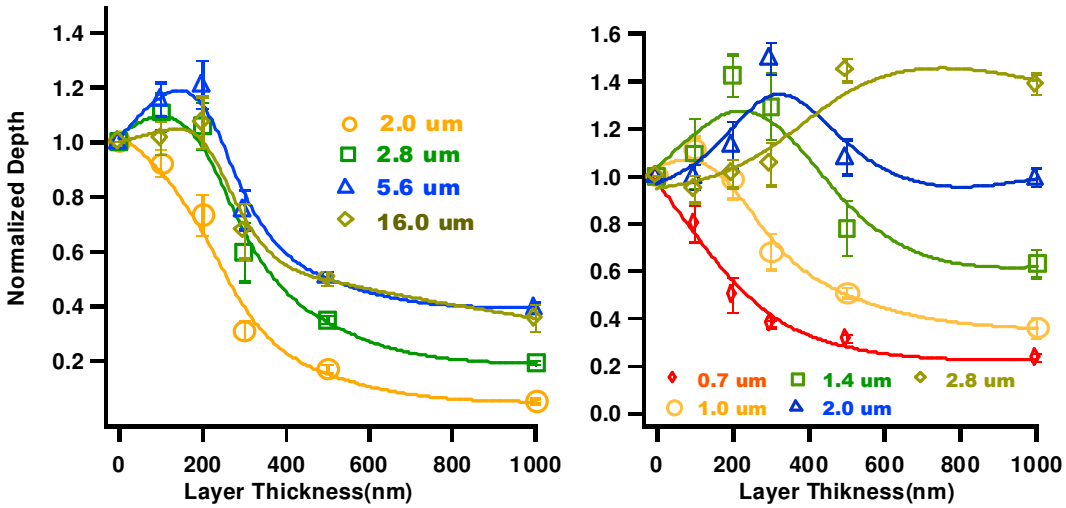

Fig. 3.10 The evolution of the normalized pit depth as a function of the thickness of the growth in (a) for constant pit diameter of 1μm and varying the center to center spacing and (b), for patterns with varying diameter and constant center to center spacing of 16μm.

coupled case.

Fig. 3.10(b) shows the evolution of the corrugation amplitude with grown thickness for a constant center-to-center spacing of 16 μm, and with the initial pit diameter varied from curve to curve. The amplitude, in nearly all cases, shows a maximum; this occurs at a critical thickness, which increases monotonically with diameter. This corresponds to the same transient instability illustrated earlier, in Fig. 3.8. The maximum in the amplitude increases slightly with diameter, reaching a value of ~50% above the initial amplitude for the largest diameter for which data is presented here (2.8μm). An exception to this is for the smallest diameter (D=0.7 μm) where no initial increase in the corrugation amplitude is observed for the thinnest layer we grew; we expect that smaller growth steps would show an initial increase here as well.

3.2 Simulations of High Temperature Growth:

To motivate the investigations described in chapter 4 here I review the results of numerical simulations carried out by H.-C. Kan which we have published elsewhere [73, 70]. There have been a number of continuum models [71, 5, 72, 18] proposed to predict the evolution of surface roughness during growth; these might be expected to apply at the length scales of our patterned structures. Here we compare our experimental results with the predictions from four models that have received considerable attention. The first is the Kardar-Parisi-Zhang (KPZ) model [71], in which instability of a flat surface to cusp formation results from fastest growth along the normal direction, and surface roughness smoothes out through evaporation and re-condensation of atoms on the surface. The

second model is that proposed by Sun *et al.* [5], which mathematically generalized the non mass conserving KPZ equation into a conserved form (CKPZ). The third model we examine is the equation proposed by Lai and Das Sarma [72] for surface evolution under MBE growth. The last model was proposed by Johnson et al. [18], which attempted to explain their observation of mound formation during homoepitaxial growth on nominally flat GaAs(001) surfaces as due to the Ehrlich-Schwoebel effect [31-33] As we show below, these four models predict distinctly different behaviors, which we compare with our experimental results.

To compare the predictions of these models with our measurements, we start with the measured topography of as-patterned surfaces and use this to set the initial conditions for our numerical simulations, integrating the continuum equations using the finite difference method [78] to simulate the growth. Anisotropy between [110] and [$\underline{1}$10] is introduced through an anisotropic version of the continuum equations [18, 71-72], replacing the standard smoothing term in the height evolution equation, e.g. $\upsilon\nabla^2 h$ with $\upsilon_x(\partial^2 h/\partial x^2)+\upsilon_y(\partial^2 h/\partial y^2)$ and the nonlinear, growth-related term, e.g. $\lambda(\nabla h)^2$ with $\lambda_x(\partial h/\partial x)^2+\lambda_y(\partial h/\partial y)^2$. We choose the *x* and *y* axis to correspond to the [110] direction and the [$\underline{1}$10] direction, respectively; *h(x, y)* describes the surface corrugation. A limitation of a number of the existing continuum equations proposed for growth is their phenomenological nature, i.e., the lack of a direct connection to physically based microscopic models. This makes it difficult to test the predictions of these equations using physically reasonable estimates of the values of the υ's and λ's; because of this, here we treat them as fitting parameters in our simulation. We find that ratios of

υ_y / υ_x and λ_y / λ_x equal to 5 and 10, respectively, produce anisotropy similar to what was observed in the AFM images. The relative magnitudes between the υ's and the λ's are chosen within the range such that the growth terms play a significant role in the evolution. Our measurements indicate that the dominant features in the topography remain those at the pattern length scale over the range of growth we have explored; this implies that local fluctuations due to instantaneous and local variations in the flux are not significant for understanding our results. We therefore numerically integrated the equations with a negligible noise term. Fig. 3.11 shows the results of the simulations for a region on which the initial pit diameter was 0.7 μm, and the spacing is 1.4 μm, for each of the four models. Fig. 3.11(a)–3.11(d) show grayscale representations of the surface morphology after allowing the simulations to run until a significant change in the morphology was visible. Fig. 3.11(e)–3.11(h) show the evolution of line profiles across the pit centers along the [$\underline{1}$10] direction. These make clear the major differences between the evolutions predicted by the models. Fig. 3.11(a) is for the KPZ model and shows the surface morphology after 1600 s of simulated growth. At this stage, the corrugations are partially smeared out along the [$\underline{1}$10] direction, similar to what is seen in Fig. 3.2(a). The profiles in Fig. 3.11(e) show that the simulated growth very quickly produces cusps at the bottom of each pit center, which again is in qualitative agreement with the observed trend shown in Fig. 3.3(a). However, no initial amplification in corrugation is evident, in contrast to our observations. Fig. 3.11(b) shows corresponding results for the CKPZ model after 3200 s of evolution. The most noticeable effect in this case is that each pit evolves from circular to elliptical in shape. The buildup of ridges of material between pits along the [$\underline{1}$10] is not as pronounced in this case as for the KPZ model. Simulated growth

line profiles for this model are shown in Fig. 3.11(f) and indicate trench formation around the bottom edges of the pits initially, which coalesce to single cusps at the bottom of each pit as growth proceeds. Significantly, the amplitude of the corrugations behaves nonmonotonically in time, with an initial amplification of the patterned corrugation.

For both the KPZ and CKPZ model, the line profiles through the pit center along the [110] direction (not shown) evolve into sinusoidal modulation, similar to those shown in Fig. 3.3(b). Fig. 3.11(c) shows a grayscale image of the surface using the MBE equation to simulate 3200 s of growth. The general appearance is quite different from the AFM images shown in Fig. 3.2 (a). Initially, a ring-shaped protrusion forms around each pit. Eventually, neighboring rings merge, forming persistent features, which are in the cusped direction but linear at right angles to this. The formation of upward cusps at the shoulders between neighboring pits is the opposite of what happens during growth, allowing us to exclude this model. Fig. 3.11(d) shows the simulation according to the model proposed by Johnson *et al.* after 1600 s of simulated growth [18]. This model predicts the formation of anisotropic mounds around and between the pits along the [$\underline{1}$10] direction. The evolution of the pits is anisotropic, as is seen in the experiment. However, both the grayscale image and the line profiles shown in Fig. 3.11(h) are distinctly different from what we observe in Fig. 3.2(a) and 3.3(a). The mounds join to the sidewalls of the pits, forming quasi continuous rings about them. The sidewalls are nearly linear, and the angles that they make with respect to (001), as well as the overall corrugation, continue to grow monotonically with time. We thus exclude this model as well. Of the four models that we have examined, only the KPZ and the conserved KPZ models predict morphological evolution that is qualitatively consistent with our observations during

epitaxial growth. We thus restrict a more complete analysis of the predicted length scale dependence to these two models.

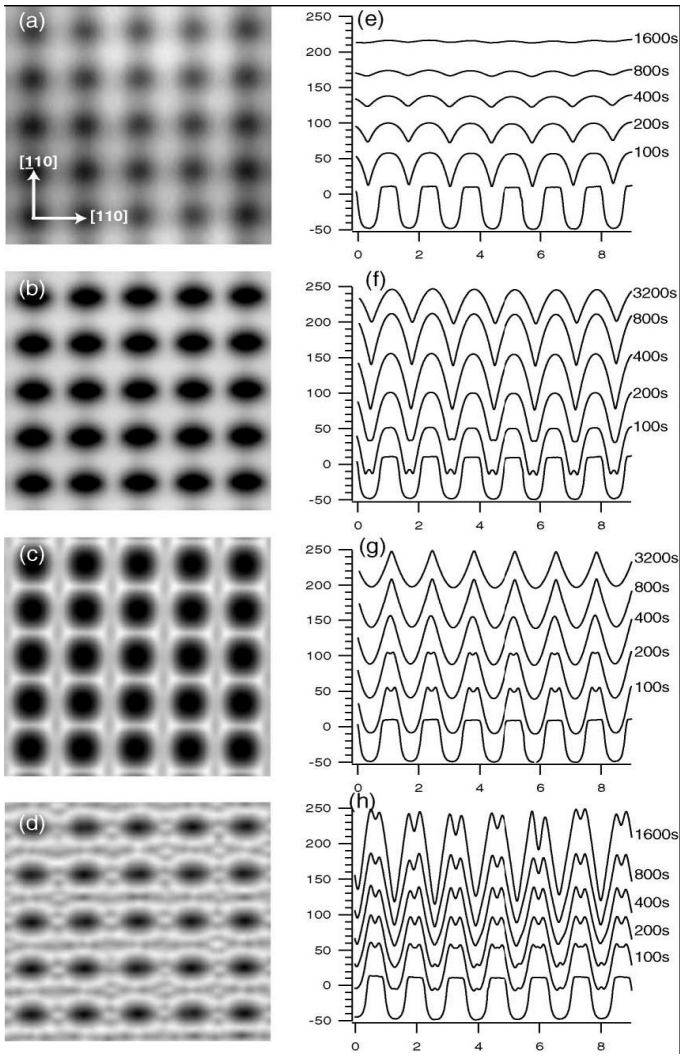

Fig.3.11 (a) –(d) Numerically simulated surface morphology of the 0.7 μm diameter pit array and (e) –(h) the line profiles scanned along the [$\underline{1}$10] direction. (a),(e) The KPZ model, with $\upsilon_x = 10$ nm^2/s and $\lambda_x = 1$ nm /s. (b),(f) The conserved KPZ model, with $\upsilon_x = 10^4$ nm^4/s and $\lambda_x = 10^3$ nm^3/s. (c),(g) The MBE model, with $\upsilon_x = 10^4$ nm^4/s and $\lambda_x = 10^3$ nm^3/s.(d),(h) The model by Johnson et al., with $\upsilon_x = 10^4$ nm^4/s and $\lambda_x = 10$ nm^2/s. The equation for this model is

$$\frac{\partial h}{\partial t} = -\nabla^2(\upsilon_x \partial^2 h/\partial x^2 + \upsilon_y \partial^2 h/\partial y^2) - \nabla((\lambda_x \partial h/\partial x, \lambda_y \partial h/\partial y)/\{1 + a[\lambda_x(\partial h/\partial x)^2 + \lambda_y(\partial h/\partial y)^2]\}), w$$

here $a = 100.00\sqrt{\lambda_x \lambda_y}$.

Fig. 3.12(a) and 3.12(b) summarize the simulated evolution of the corrugation vs initial pit diameter for the KPZ and CKPZ models, respectively. The results differ qualitatively from one another. The KPZ equation predicts a monotonic variation of the corrugation amplitude with lateral period and a monotonic decay with growth for any given initial pit diameter (3.12(a)).

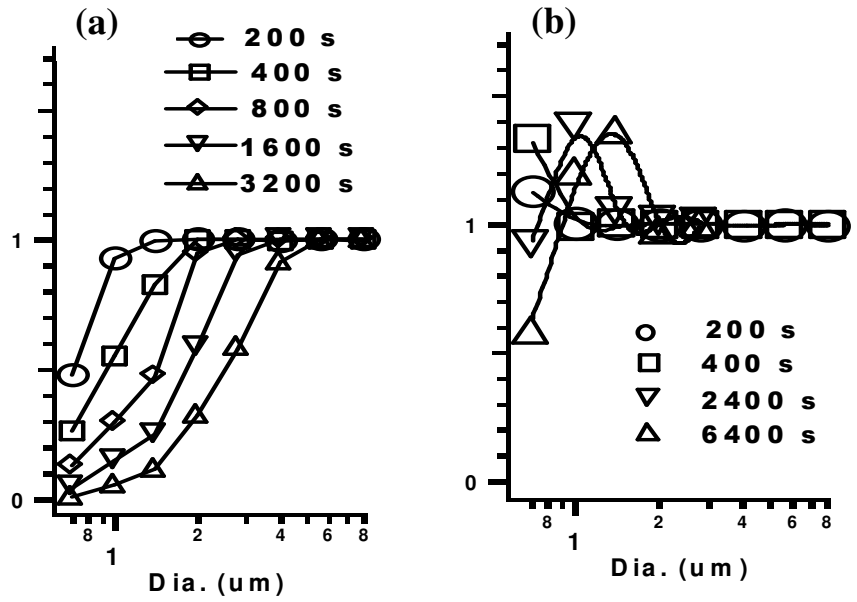

Fig. 3.12 The overall amplitude of the pit array corrugation measured after each growth from line profiles across the pit center along the [$\underline{1}$10] direction normalized with its initial values, plotted as a function of the initial pit diameter for(a) KPZ model, and (b) conserved KPZ model.

This is inconsistent with the experimental results shown in Fig. 3.9. However, the CKPZ model [Fig. 3.12(b)] shows a peak in the corrugation with respect to lateral length scale, which moves to larger diameters with increased growth. The amplitude of the corrugation also behaves non monotonically with growth for a fixed initial diameter, with an initial amplification and an eventual decay, qualitatively consistent with our observations. The CKPZ model is thus in closest agreement with our patterned growth experiments. However, there are quantitative discrepancies. Most notably as seen in Fig.

3.9, our observations show a maximum corrugation amplitude which increases with growth, while those predicted by CKPZ are approximately constant.

This lack of complete agreement is not surprising. Since continuum models such as CKPZ were developed for describing the long term behavior of the surface roughness, only those terms which dominate in the asymptotic limit were kept in the height equation. In our case, the transient evolution of a surface that is artificially patterned with sharp edges would presumably require additional terms to be maintained. A modification of this and other continuum models to do so is beyond the scope of this investigation. Nevertheless, the comparison between the experiment and the simulation presented here demonstrates a straightforward approach for testing existing models in the technologically relevant transient regime and potentially could also provide guidance for further refinement of existing models. Our observations of the evolution of the morphology of a patterned GaAs(001) surface shows the response of surface roughness to be nonmonotonic, with an initial amplification followed by decay and a characteristic lateral length scale, which divides these behaviors and whose value increases with further growth.

These observations allow us to rule out the KPZ model for MBE growth in this system, in contrast to the conclusions of [10]. We find instead that, among the models proposed in the literature, the conserved KPZ model most closely reproduces what we observe. In chapter 4 we present a corresponding atomic scale model based upon physical processes.

3.2.1 Extended Simulations of Growth vs Pattern length and Initial Pit Diameter:

Fig. 3.13 shows the CKPZ simulated surface morphologies for the patterned regions shown in Fig. 3.1 and 3.5, after prolonged simulation up to ~ 50 000 s of simulation time. This corresponds to changes in the amplitude of the surface corrugation which are comparable to what is observed in the experiment after 500 nm of growth. The simulated images resemble those of Fig. 3.1(a), 3.1(b) and 3.5(a) and 3.5(b). Panel 3.13(a) shows evidence for strong coupling between neighboring pits at smaller spacing, while panel 3.13(b) shows no such evidence at larger spacing, and panels 3.13(c) and 3.13(d) show a localized blurring of the pit edges, with no obvious evidence for coupling.

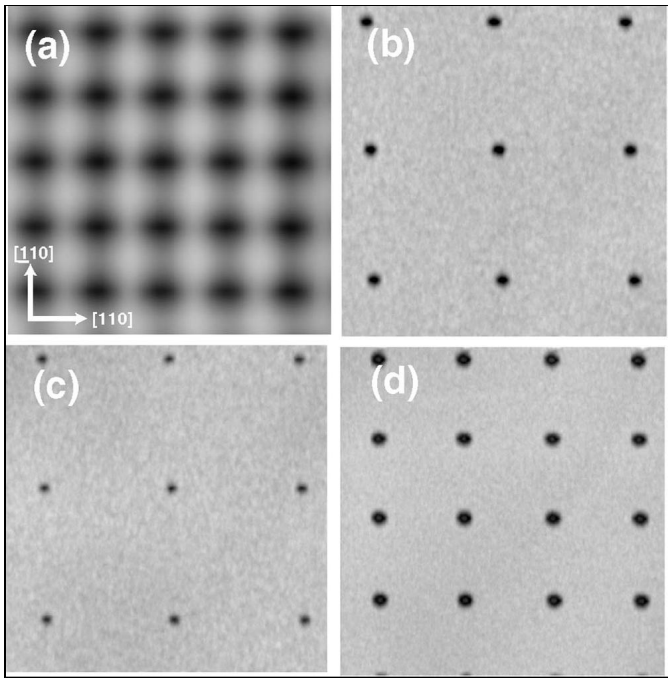

Fig. 3.13 Simulated evolution of patterned surface with conserved KPZ equation. (a), (b),(c), and (d) are results after ~50,000 s of numerical simulation taking the AFM images shown in Figs. 3.1(a)& 3.1(b) and also 3.5(a)and 3.5(b)as starting topography, (a) S=2 μm, D=1 μm; (b) S=16 μm, D=1 μm; (c) S=0.7 μm, D=16 μm; (d) S=2.8μ m, D=16 μm.

Fig. 3.14 shows the time dependence of line profiles across the pits predicted by these simulations. Panels 3.14(a)–3.14(d) show more clearly that the close similarity of the variation of evolution with S to that seen in the experiment, i.e., panels 3.3(a) - 3.3(d). For smaller spacing, a strong coupling between neighboring pits is again evident from the curvature of the profiles between pits. One discrepancy is that the simulation predicts trenches at the pit bottoms along both directions for small amounts of growth; these are not observed in our experiments. However, as seen in panel 3.14(a), for further simulated growth the side walls of the pits close in along the [$\underline{1}$10] direction. The resulting cusps at the pit bottoms again persist through the simulation, consistent with our observations. From then on the simulated line profiles show the same intersecting concave downward parabolas seen in panel 3.3(a). In addition, along the [110] direction, panel 3.14(b) shows an evolution of line profiles which reproduce that of Fig. 3.3(b), becoming sinusoidal curves. At larger spacing, panels 3.14(c)–3.14(d) also show trends similar to those observed in Fig. 3.3(c) and 3.3(d), except that here the initial increase of the amplitude is somewhat larger than observed experimentally.

A comparison of panels 3.14(e)–3.14(h) from the CKPZ simulations with 3.7(a)–3.7(d) from the experiments shows that the qualitative agreement extends to the evolution at a fixed separation of 16 μm: individual pits evolve without coupling to their neighbors. For the smallest pit size, i.e., D=0.7 μm, panels 3.14(e) and 3.14(f) display a larger initial increase in the amplitude of the corrugation at the beginning of the simulation than that observed. However, for larger pit size, panels 3.14(g) and 3.14(h) reproduce the transient trench formation at the pit bottoms seen in Figs 3.7(c) and 3.7(d); although the pit bottoms are smoother in the simulation. It is clear from the top profiles

shown in panels 3.14(g) and 3.14(h) that the simulation has not yet reached the extent of evolution observed in the experiment. Substantial extension of the simulation would be computationally expensive; the results shown here required months of computing time.

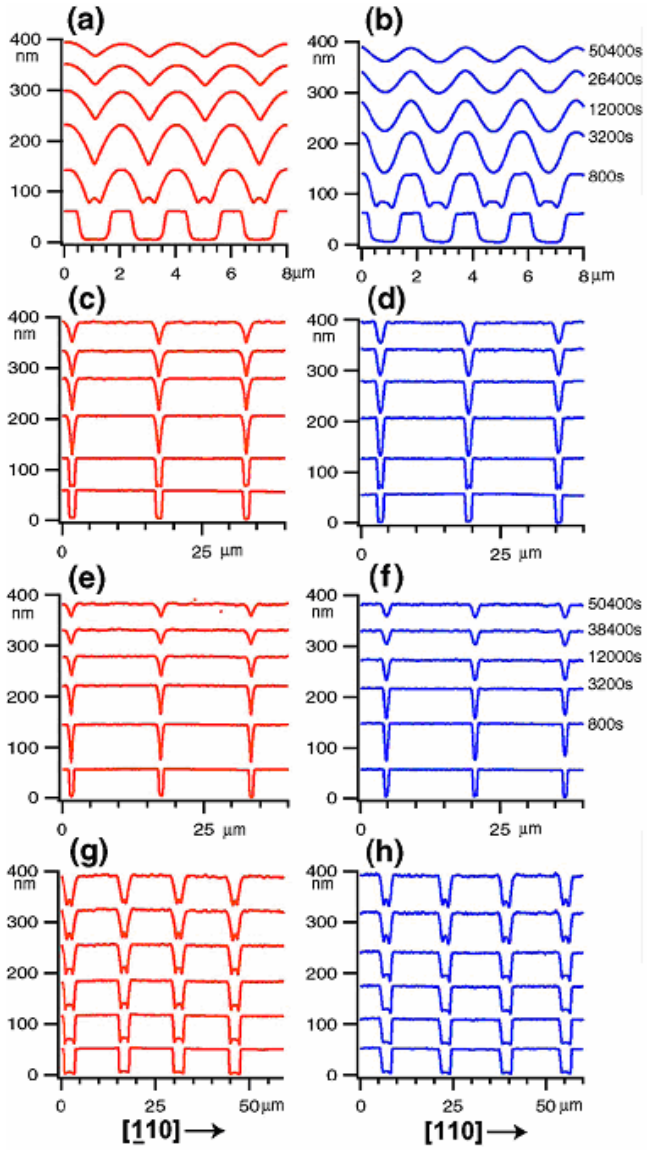

Fig. 3.14 Line profiles scanned across the center of the pits from the CKPZ simulations. Line profiles in (a), (c), (e), and (g) are scanned along the [1̲10] direction, and those in (b), (d), (f), (h) are scanned along the [110] direction. In panels (a)–(b) D=1 μm, S=2 μm; (c)–(d) D=1 μm, S=16 μm; (e)–(f) D=0.7 μm, S=16 μm; (g)–(h) D=2.8 μm, S=16 μm. In each panel the bottom profile is the initial surface. For panels (a), (b), (c), and (d) the simulation time is indicated in panel (b), and for panels (e),(f), (g), and (h) the simulation time is indicated in panel (f).

Summary plots of the normalized pit depth as a function of spacing and diameter from the conserved KPZ simulation are shown in Figs 3.15(a) and 3.15(b). A comparison with the corresponding experimental plots in Figs 3.4 and 3.8 again shows that the simulation reproduces the qualitative trends seen in the experiment. Panel 3.15(a) shows a knee in the amplitude, with decreasing values beneath S~4 μm. It also shows the transient amplification and eventual decay with time seen in Fig. 3.4. There are quantitative discrepancies, however; higher maximum amplitudes are predicted in the simulation than in experiment. In addition, as seen in Fig. 3.4, the experiment shows sign of broad, weak maxima for layer thickness of growth greater than 300 nm, while panel 3.15(a) shows a much weaker maximum near S~5.6 μm.

Fig. 3.16 summarizes the thickness / time dependence of the normalized surface corrugation for both the experiment and simulation for selected patterns. For a fixed pit diameter of 1 μm and variable spacing, Fig. 3.10 (a) shows that in the experiment the time variation for all but the smallest spacing lie essentially along the same curve, reaching a maximum corrugation ~20% larger than the initial size by 200 nm of growth. Beyond this, the amplitude of the corrugations decays with growth. There is a significant reduction in the rate of decay beginning at approximately 400 nm of growth. The pattern with the smallest spacing, S=2.0 μm, follows a slightly different curve. The simulations for the same sequence, shown in panel 3.16 (a), show very similar behavior, but again with some quantitative differences; the maximum amplitude is ~40% larger than initial value, rather than 20% as measured, and the reduction of the decay rate at a later stage is not as obvious.

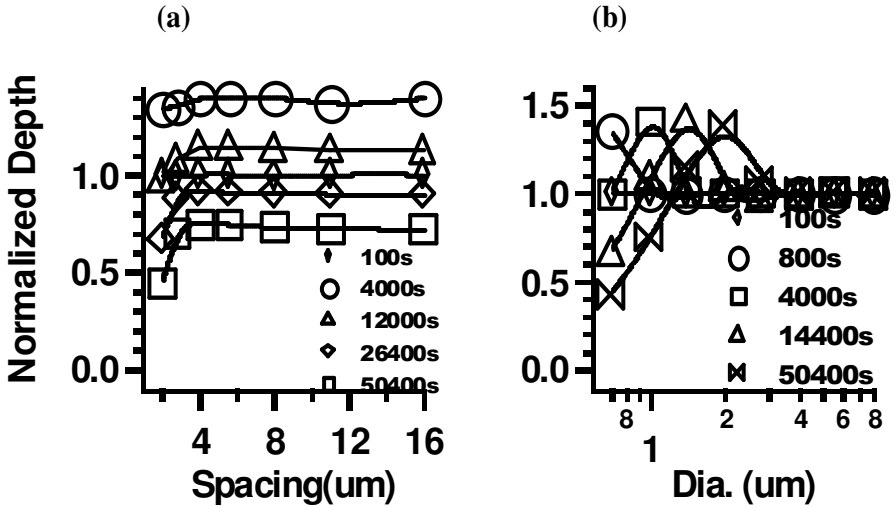

Fig. 3.15 Summary plots of the normalized pit depth measured from line profiles, along [1̄10] direction, as a function of characteristic dimensions after each growth step from the simulations. (a): normalized pit depth plotted as a function of spacing at a fixed diameter D=1 μm (sequence A). (b): normalized pit depth plotted as a function of diameter at a fixed spacing of 16 mm (sequence B).

Examining the fixed spacing/variable diameter results of Fig. 3.10(b) shows that in the experiment each pattern reaches maximum amplitude at a critical thickness of growth, as was also seen in Fig. 3.8. The thickness at which this maximum occurs increases with the initial diameter of the pit, i.e., the larger the pit the later it reaches maximum corrugation with growth. The maximum amplitude increases slightly with diameter and reaches ~50% above the initial amplitude for the case of D=2.8 μm. An exception to this is the pattern with D=0.7 μm, where no initial increase in the corrugation amplitude is observed. This might be due to the coarse steps in growth used in our experiments. Panel 3.16(b) shows that the simulation again catches the general trends seen in the experiment (Fig. 3.10(b)), predicting an initial increase in the amplitude for all pit diameters; the simulation predicts a transient increase even for D=0.7 μm,

however, in contrast to the experiment. It correctly predicts that the maximum amplitude reached in the evolution is approximately 50% above the initial value. As we discuss in chapter 4, the equation proposed by Sun *et al.* [5] mathematically converts the well-known KPZ equation [71] i.e.,

$$\frac{\partial h}{\partial t} = \upsilon.\nabla^2 h + \lambda(\nabla h)^2$$

into a version that conserves mass deposited on the surface. However, this operation also changes the form of the nonlinear term. In the KPZ equation, the evolution of surface roughness results from the competition between the linear term $\upsilon\nabla^2 h$, which is associated to the process of the adatom evaporation and recondensation, and the nonlinear term $\lambda(\nabla h)^2$, which describes the growth along the surface normal direction. In the conserved KPZ equation, the linear term $-\nabla^2(\upsilon\nabla^2 h)$ now describes the process of surface diffusion of an adatom on the surface [79] However, the physical nature of the nonlinear term $-\nabla^2.(\lambda.(\nabla h)^2)$ has not been clear. Villain first suggested that this term could be derived from the surface slope dependence of the adatom density, i.e., $\rho = \rho_0 + \rho_1.(\nabla h)^2$ [79]. Since the surface adatom flux $\vec{j} \propto -\nabla\rho$, and $\frac{\partial h}{\partial t} = -\nabla.\vec{j}$ for the continuum equation that conserves mass, a positive value of ρ_1 leads to the same nonlinear term in Eq. (1) but with the opposite sign. Later on, Politi *et al.* [80] indicated that in the limit of small surface slope, a "symmetry breaking (adatom) current" could lead to the same nonlinear term in their continuum equation with the same sign as in CKPZ equation. Similarly, based on general physical arguments and the series expansion of the functional dependence of the effective Hamiltonian, Lai *et al.* [72]

proposed their MBE equation, which also include this nonlinear term (with the opposite sign).

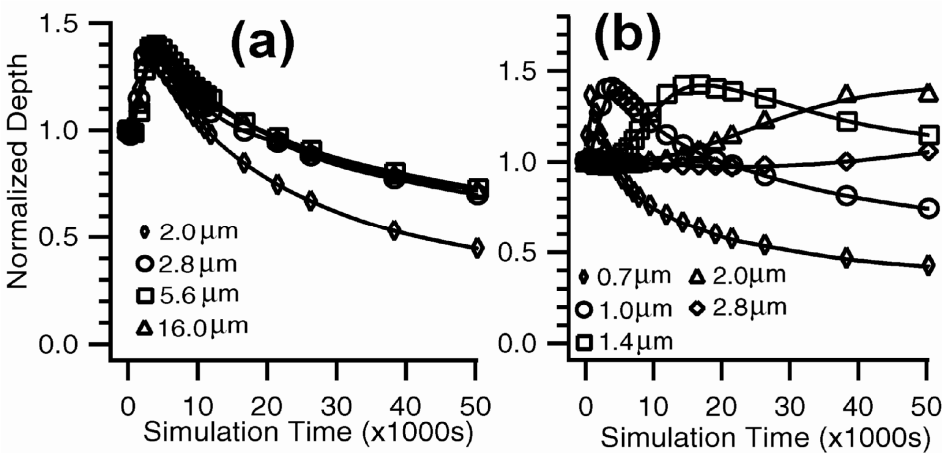

Fig. 3.16 The evolution of the normalized pit depth as a function of the thickness based on the simulation time in (a), correspond to the evolution for patterns with varying spacing (Fig. 2.1, sequence A), and (b) for patterns with varying diameter (Fig. 2.1, sequence B).

The results we have presented here provide an extensive test of the conserved KPZ equation against experimental observation. The excellent qualitative agreement seen here argues for the correctness of the form of this nonlinear term. This serves a starting point toward the ultimate goal of these studies, which is an understanding of the atomic processes corresponding to this term in the continuum limit, leading to a predictive capability for practical thin film growth. Based on the notion of the up-down symmetry-breaking nature of the conserved KPZ equation, we now speculate on a scenario based upon atomic scale surface process which might lead to the nonmonotonic evolution we observe both in the experiment and in the simulation based on the conserved KPZ equation. In this scenario, the formation of trenches at pit

bottoms at the beginning of growth causes the up-vs -down symmetry breaking in the morphological evolution of the patterned surfaces.

Based on our AFM observations, islands nucleate and grow at flat areas such as the pit bottom and areas in between the pits during growth. On the other hand, the side walls of each pit consist of dense arrays of steps, which move inward, toward the center of the pit during growth. Trenches form at the bottom of a pit, adjacent to the sidewalls due to the island nucleation and growth at the pit bottom. The collection efficiency of atoms landing on the surface is smaller at the trenches; this is essentially the "Zeno effect" suggested by Elkinani and Villain [81]. This slows down the motion of the steps at the bottom of the sidewall, causing bunching of steps there. This would correspond to negative ρ_1 in Villain's model [79] since the effect is a lower adatom density in regions in which steps are bunched together. It is reflected by a steeper surface slope at the trench, consistent with the effect of the nonlinear term in the CKPZ equation, which increases the slope at the bottom for the simple case of a sinusoidal height profile. Further growth eventually causes the sidewalls to close inward, coalesce into cusps at the pit centers. During this stage, the total collection efficiency of the atoms at the pit bottom is significantly decreased, and results in a slower growth rate here compared to that at the flat regions between the pits. Therefore, the overall amplitude increases and reaches a maximum larger than the initial amplitude. Subsequent to the trenches coalescing into cusps, further growth fills the cusps slowly. For pit arrays with the same diameter but with varying spacing in Fig. 2.1 (sequence A), it would take roughly an equal amount of growth for the trenches at each pit bottom to coalesce. This would imply that the amplitude of the corrugation should reach maximum at nearly the same

time, as observed in Fig. 3.10(a) from the experiments and reproduced in the simulation, as shown in Fig. 3.16(a). The only exceptions are pits with smaller spacing, where diffusion results in a strong interaction between the neighboring pits. On the other hand, for pit arrays with varying diameter but with fixed spacing in Fig. 2.1(sequence B), it is clear that it takes longer growth for the trench at the pit bottom to merge for larger pits. This is what we see in both the experiment and the simulation, i.e., Fig.s 3.10(b) and 3.16(b), respectively described above, the trench formation breaks the up-down symmetry in two respects: partial pinning of the step motion at bottom of the sidewall, and merging of the trench leading to a slower rate of growth at the pit bottom. As seen from Figs. 3.11, 3.12 among the continuum model we have tested, the conserved KPZ model is the only one that predicts the formation of trenches at pit bottoms at the beginning of growth; physically the form of the equation arises naturally in the scenario we describe above.

To summarize the results of this chapter, our experimental characterization of the length scale dependence of the evolution of the surface roughness during homoepitaxial growth on patterned GaAs(001) surfaces shows pronounced differences in the dependence on two distinct characteristic lengths. For patterns with varying pit spacing and fixed pit diameter, coupling between closely spaced pits plays a significant role in the evolution of surface morphology during growth, increasing the rate of evolution. In the limit of large spacing, no such coupling is observed, and the evolution of the amplitude of corrugation proceeds at a rate independent of spacing. For patterns with varying pit diameter and a large fixed spacing, the evolution of the amplitude of the surface corrugation shows non monotonic behavior both with regard to lateral size and

grown film thickness; this is similar to our previous observations [70] for the small spacing limit as illustrated in Fig. 3.8. There is a characteristic diameter which separates regimes of amplification and decay, which increases with growth. We find that simulations based upon the conserved KPZ model reproduce these more extensive experimental observations qualitatively.

The level of quantitative agreement might be improved given more extensive calculations in which the parameters of the model are optimized, however, the existing calculations already required months of computing time. The qualitative consistency between the experiment and the numerical simulation seen in this detailed comparison provides a strong case for the correctness of the form of the nonlinear term in the corresponding height equation. Finally, the form of the equation can be understood in a simple scenario based upon diffusion in the presence of an adatom density which is small in regions where steps bunch up during growth.

Chapter 4

Dependence of Unstable Growth Mode on Temperature and As_2 Flux:

In this chapter we present the major experimental results of this thesis, a study of the temperature and arsenic flux dependence of the unstable growth mode described above. In particular, we were interested in a possible connection between the preroughening of GaAs(001) at T~530 ºC in the absence of growth [82] and the unstable growth we reported on at 585 ºC in chapter 3.

4.1 Determination of Preroughening Temperature in As_2 flux:

In the earlier work of Labella, et al. [82] it was found that the preroughening [83] onset temperature, i.e. that above which a large density of islands spontaneously form at the surface in the absence of growth, decreased monotonically with the magnitude of the incident As_4 flux; a limiting value of ~527 ºC as the flux approached zero was determined[82]. In our earlier observations we however used As_2 flux [2, 74]. We thus began these studies by repeating the annealing experiments described by *Labella et. al*. substituting As_2 for As_4.

We first annealed unpatterned GaAs (001) surfaces under the same As_2 flux used in our earlier growth experiments. We performed these annealing experiments at a series of increasing temperatures for 1 - 2 hours, with longer anneals at the lower end of the temperature range we explored. Throughout this thesis we will thus refer to the As_2 flux corresponding to a growth rate of 0.32 nm/s and as As_2 /Ga beam equivalent pressure

ratio of 10:1 as "moderate" flux. This terminology will reduce confusion in comparing results from different growth stations. As described earlier, in chapter 2, we first removed the native oxide layer in the presence of atomic hydrogen ($1.1x10^{-6}$ torr) while heating to a temperature of approximately 300 ºC for 40 minutes. With the oxide removed, we then grew a 0.4 µm thick buffer layer on the substrate at 580 ºC. This last step follows Labella's procedure, and is designed to reduce extrinsic effects due to frozen in surface roughness resulting from the oxide removal process. The growth parameters for the buffer layer are shown in table 4.1.

Growth Temperature(ºC)	580 ºC
Growth Rate(ºA/ Sec)	0.32 nm/ sec
Gallium BEP(mbar)	2.8 e-6
Arsenic BEP(mbar)	2.8 e-5
Layer Thickness(μm)	0.4

Table 4.1 Growth parameters for the buffer layer ("moderate"As_2 Flux)

After annealing, we cooled the wafer abruptly by switching the substrate heater power off. The As_2 flux was maintained at its "moderate" value until the temperature dropped beneath approximately 450 ºC, at which point the As_2 flux was terminated. Beneath 450 ºC continued exposure to this As_2 flux caused the streaks in the RHEED pattern to disappear, indicating the formation of an amorphous layer on the surface which would prevent determination of the equilibrium GaAs(001) morphology.

Next we measured the topography of the resulting surface using tapping mode atomic force microscopy, in air. We tacitly assume that the thin oxide layer which forms is conformal to the morphology of the surface which forms during annealing. There is some reason to believe that this should be so: previous measurements by *Tsai et. al.* show this to be the case for Si surfaces [84], and as the native oxide thickness is smaller for GaAs, we expect this result to carry over to GaAs.

In agreement with previous reports by Labella, et al [82], our annealing experiment shows evidence for pre-roughening. Specifically, as we discuss below, we observe an abrupt increase in the density of islands on the surface on increasing the annealing temperature through a specific value; this temperature increases with As_2 flux.

Fig. 4.1(a) shows the surface after annealing in the presence of a "moderate" As_2 flux (as defined above) for one hour, at a temperature of 700 ºC. The surface is covered with islands connecting together on the terraces away from the step edges. As shown in Fig. 4.1(b)-(c) reducing the annealing temperature does not change the surface morphology qualitatively. The surface remained covered with islands but showed no evidence for formation multiple level islands, as would be expected if a roughening transition occurred. Very different results are seen for annealing temperatures below 525±25 ºC as shown in Fig. 4.1(e), 4.1(f); very few islands were observed on the terraces. The surface shows large-scale finger-shaped terraces, indicative of incomplete coalescence of the islands which form during growth. Visually, from these AFM images it is clear that the preroughening transition must occur somewhere between 500 ºC and 550 ºC.

To make this determination more quantitative, we measured the root-mean square (RMS) roughness using regions ~100nm x 100nm in extent, on large terraces away from the step edges for the determination. The lateral extent of these regions is more than an order of magnitude larger than the correlation length determined from the same regions.

The results are summarized in Fig. 4.2, which shows the RMS roughness vs. the annealing temperature. The solid curve is a cubic spline interpolation, and shows an inflection point in the temperature dependence at ~540 ºC. We use this as an estimate of the pre-roughening onset temperature at this As_2 flux.

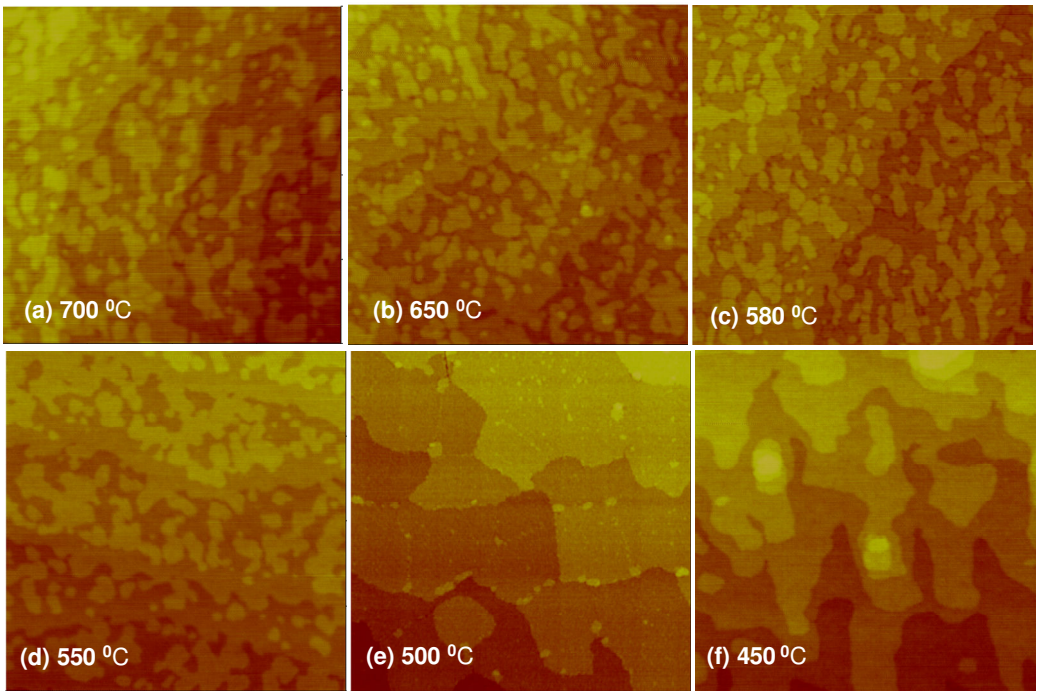

Fig. 4.1 AFM images of GaAs(001) surface after annealing under"Moderate"As_2 flux at different annealing temperatures. Field of view is 1 µm x 1 µm. Vertical range is 5 nm full scale.

As a consistency check, we repeated a part of the annealing experiment described above, using temperatures slightly above(550 ºC) and slightly below(525 ºC) that of the

inflection point in Fig. 4.2. The resulting AFM images, (not shown) confirm a dramatic increase in the island density occurs at an intermediate temperature. Based upon this, the corrected pre-roughening onset temperature in is 537 ± 13 ºC, in agreement with the value of 535 ºC.

As we will show later, an important insight into understanding whether thermodynamic pre-roughening is relevant in the growth mode change that we observe comes from the variation of onset temperature with As_2 flux. *Labella et. al.* reported [82].

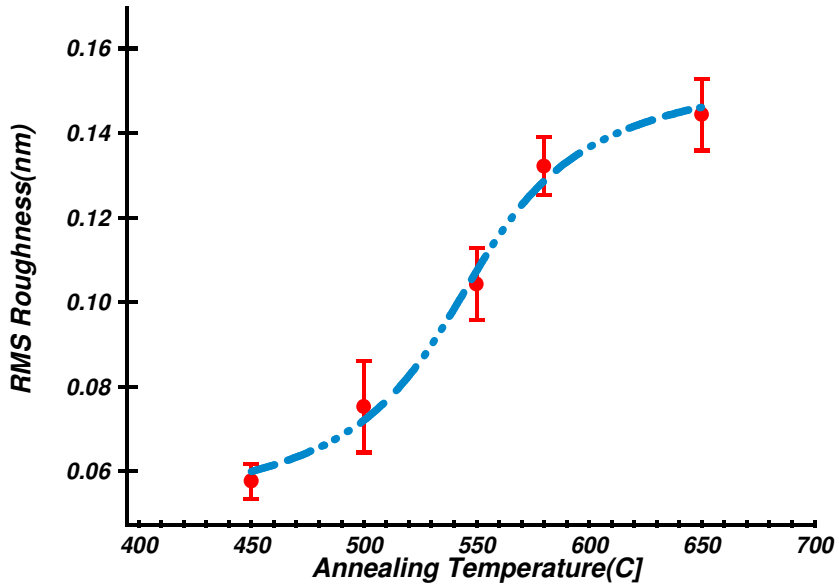

Fig. 4.2 RMS roughness vs annealing temperature for GaAs(001) surface after removing the native oxide in the presence of atomic hydrogen, heating to 300 ºC for 40 min and grown a 0.4 ㎛ buffer layer. The annealing has been done under As_2 (BEP)=2.8x10 $^{-5}$ mbar.

that the onset temperature shifts monotonically upward with increasing As_4 flux; to see if the trend is the same for As_2 we performed similar annealing experiments for As_2

fluxes five times larger(" high flux") and one half ("low flux") of that used in Fig. 4.2. Fig. 4.3 shows the *preroughening onset temperature increases with increasing As_2 flux*. This monotonic increase with flux is qualitatively consistent with what was observed for As_4 [82].

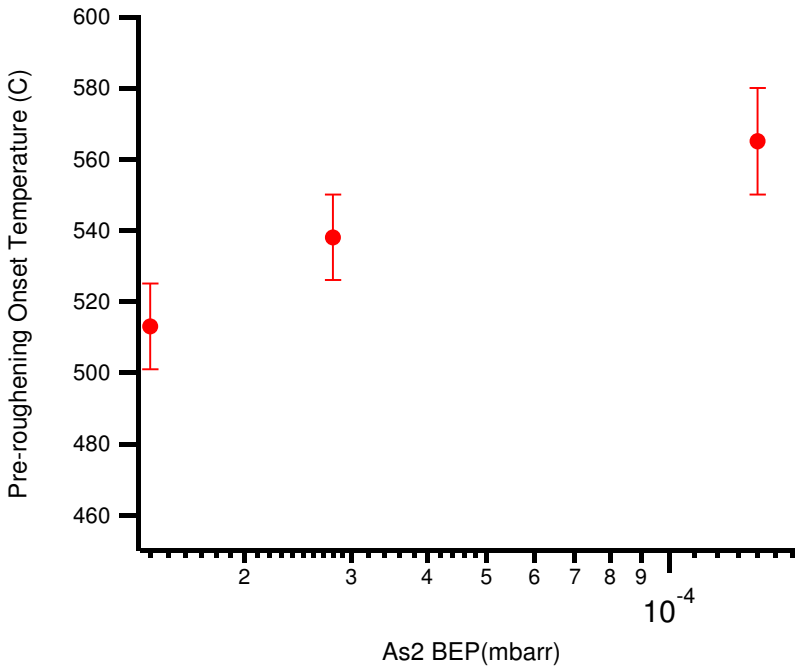

Fig. 4.3 GaAs(001)Preroughening onset temperature vs As_2 beam equivalent pressure.

4.2 Growth on Patterned Surfaces:

4.2.1 Growth above and below the onset temperature (Coarse Growth Steps):

In this section we investigate the temperature dependence of the unstable growth mode which Shah, et al studied at a single growth temperature and flux [2, 74], and how this changes with As_2 flux. We then use these results to determine whether or not

thermodynamic pre-roughening observed here and by Labella [82] has a significant effect on the growth mode.

In this part of the study, we carried out a set of growth experiments on the patterned surfaces described in Section 2.2 at temperatures well above and below the pre-roughening temperature which we determined in the annealing experiments described above. As was done by Shah, we restrict our analysis to regions of the surface for which the center to center spacing is twice the initial pit diameter.

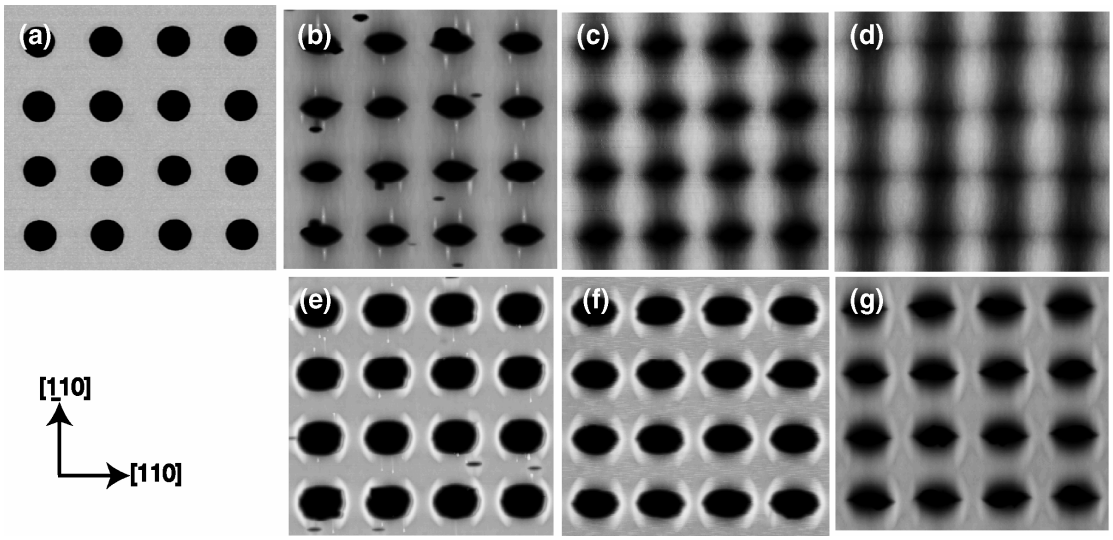

Fig. 4.4 AFM images of patterned GaAs(001) for 0.7 μm pit diameter (a) before MBE growth, (b) after growth of 100 nm growth at 600 °C, (c) after 200 nm growth at 600 °C, (d) after 500 nm growth at 600 °C, (e) after 100 nm growth at 500 °C, (f) after 200 nm growth at 500 °C, (g) after 500 nm growth at 500 °C. Field of view is 7.5 μm x 7.5 μm. Vertical range is 100 nm full scale.

In the initial growth experiments an atomic hydrogen source was not available; the patterned samples were heated to a temperature approximately 625 ºC under "moderate" As_2 flux to sublimate away the oxide layer. Temperature measurement and determination

of when the oxide layer had desorbed were as described in a previous chapter. Once the oxide was removed, a streaky RHEED pattern appeared on the screen, which after one hour annealing at 550 ºC under a "moderate" As_2 flux showed the half-order and quarter-order streaks characteristic of the β_2(2x4) reconstruction generally reported on GaAs(001) under these conditions [55]. The purpose of the annealing was to heal some of the roughness generated during the sublimation of the oxide [64, 82]. The choice of the temperature was based upon previous experience [85]. We expect, based upon the results we presented in the last section that the resulting surface between pits contains a high density of monolayer-height islands. We grew films of various thicknesses ranging from 100 nm to 500 nm under "moderate" arsenic flux conditions at temperatures of 500 ºC and 600 ºC, i.e. below and above the thermodynamic pre-roughening temperature in the absence of growth, respectively.

We find that the growth mode changes dramatically between these two temperatures. A clear signature of this change can be seen in the AFM images displayed in Fig. 4.4, which allows a comparison between the surface topography for growth at these temperatures for films of increasing thickness on a region of the substrate in which 0.7 μm diameter pits are spaced at 1.4 μm, center-to-center. Panels (a)-(d), at the top of the figure are for growth at 600 °C. In agreement with our earlier results for growth at 585 °C [2, 74] the growth results in a pronounced anisotropy of the pattern. These images also show evidence for an initial instability towards mound formation, most easily seen in Fig. 4.4(b) as the narrow, vertical features, concentrated near the edges of the pits. In agreement with earlier reports [2, 64], we find that the mounds are transient structures and eventually disappear, though coalescence, after further growth (Fig. 4.4(c), (d)). The

structure evolves more quickly with growth along the [$\bar{1}$10] direction. The evolution is not a simple smoothing of the pattern: there is build up of material between the pits along the slow direction [110] which leads to column-wise-structure (Fig. 4.4(d)), similar to what was shown in Fig. 3.3(a) for growth at 585 ºC.

Contrasting behavior occurs for growth on this pattern below the pre-roughening temperature, as shown in Fig. 4.4(e)-(g). Anisotropic rings build up around the edges of each pit, along the more slowly evolving [110] direction (Fig. 4.4(e)). The rings amount to multilayer stacks of terraces which wrap partially around the edges of the pits. With further growth the rings spread out, as seen in Figs. 4.4(f), (g).

The contrast in evolution between these two temperatures is seen even more clearly in height profiles measured across the pit centers, and shown in Fig. 4.5, in the form of profiles measured along both the [110] and [$\bar{1}$10] directions. Fig. 4.5(a) is for growth at 600 °C along the faster evolving [$\bar{1}$10] direction. The bottom-most profile, of the substrate as patterned, is nearly square. After 100 nm of growth the profiles show formation of cusps at the center of the pits; further growth reduces the amplitude of the corrugation, but the cusps still remain. As we have pointed out elsewhere [2, 74], this is markedly different from what would be expected in a simple diffusion-mediated relaxation of the pattern. In addition, we find that within the pits the sidewalls are not flat, so that this does not correspond to a faceting during growth. The evolution is both slower, and different along the [110] direction for growth at 600 ºC, as seen in Fig. 4.5 (c), with the profiles becoming sinusoidal by a film thickness of 200 nm. For growth at 500 °C, along the fast evolving [1$\bar{1}$0] direction we again see formation of cusps at the center of the pits which persist during the further growth (Fig. 4.5b). The rings which

were visible in Fig. 4.4 (e)-(g) are easily seen in the profiles along [110] for growth at 500 °C, shown in Fig. 4.5 (d); they appear as peaks at the upper edges of the pits. With continued growth the peaks move together and coalesce as the ridges expand outward from the centers of the pits, by a film thickness of 500 nm.

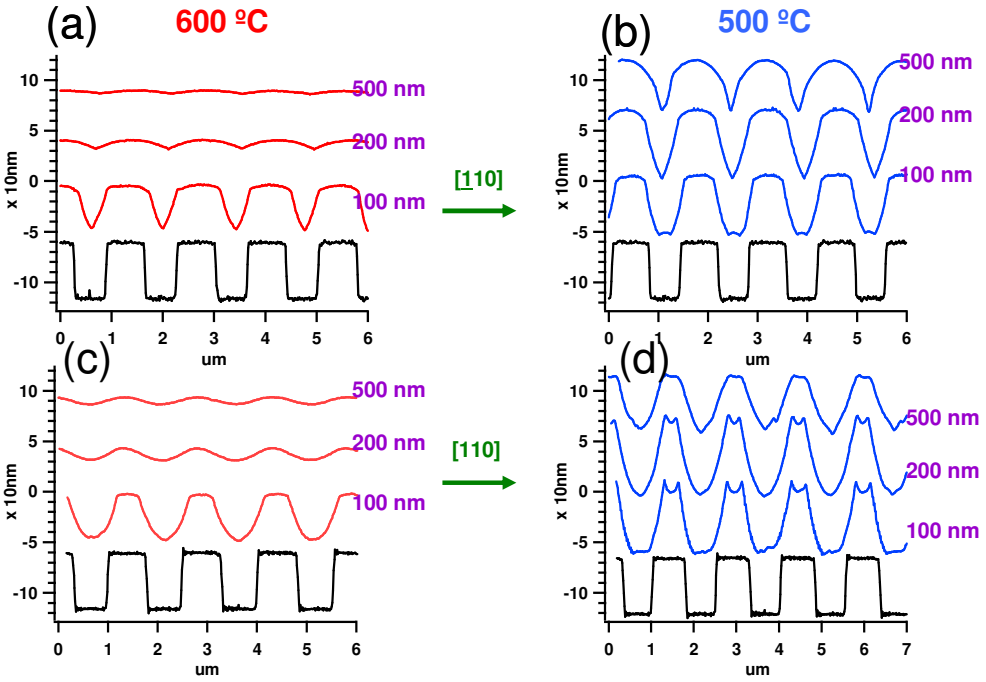

Fig. 4.5 Measured AFM height profiles across center of pit structure along [1̲10] ((a) & (b)) and along [110] ((c) & (d)), for MBE growth at 600° C ((a) & (c)), and for growth temperature 500° C ((b) & (d)).

Fig. 4.6 shows the normalized depth versus pit diameter for growth at 600 ºC (a) and at 500 ºC (b). Fig. 4.6(a) is qualitatively consistent with what we see for the growth at 585 ºC, Fig. 3.9. The amplitude of corrugation decreases after the first growth for pit diameters beneath 1 μm; a maximum is seen in the first growth curve at ~ 1.2 μm, beyond this the normalized depth approaches 1 asymptotically. Further growth again

leads to increasing the amplitude and a shift in the maximum to the larger diameters. For the growth at the lower temperature (Fig. 4.6(b)) the amplitude of the corrugation measured along [1̲10] shows qualitatively similar, but quantitatively different behavior: the maximum in each curve is shifted to a smaller diameter. This is consistent with a smaller diffusive smoothing effect at lower temperatures.

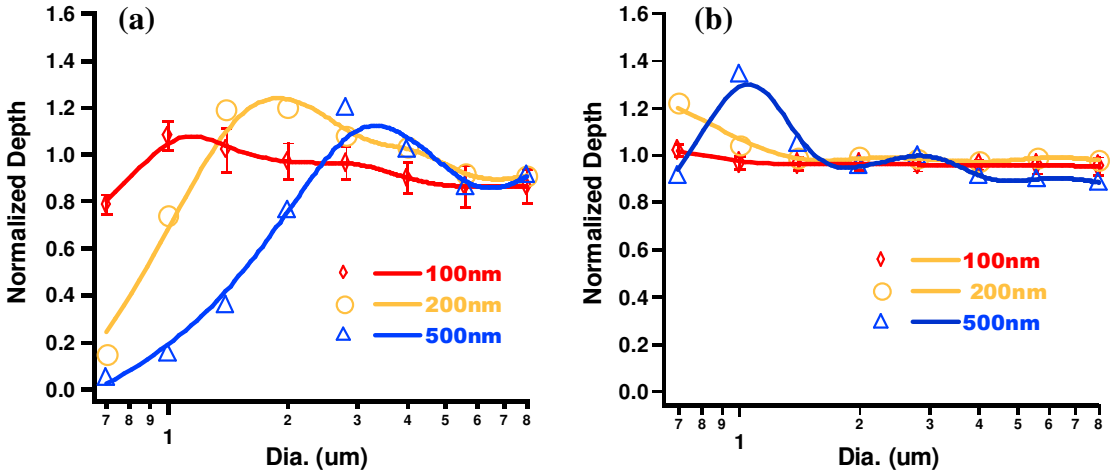

Fig. 4.6 Summary plot of Normalized Depth vs. initial pit diameters after various stages of GaAs Homoepitaxial growth along fast evolving direction [1̲10]at 600 ºC (a), and 500 ºC (b) on patterned GaAs (001).

The height of the ring also changes with grown thickness. Fig. 4.7. shows how the ring height depends on the pit diameter.

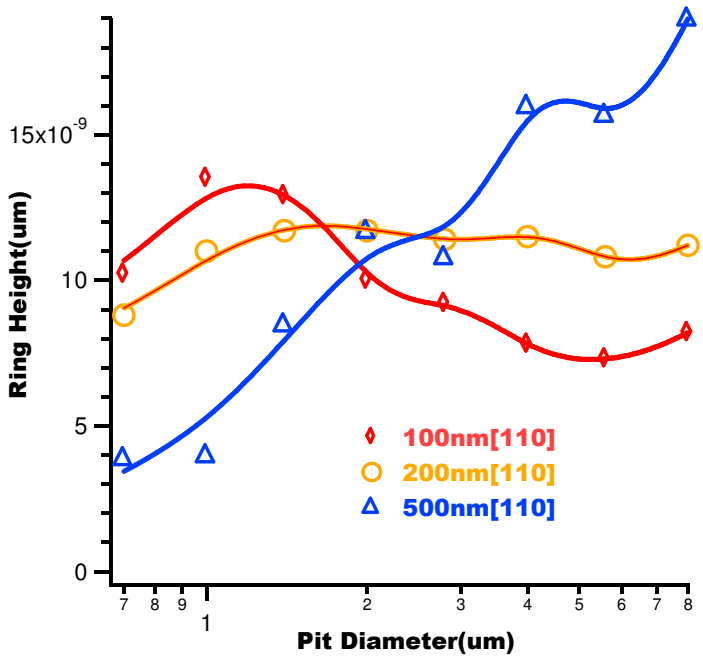

Fig. 4.7 Height of the ring vs pit diameter for different growth thicknesses, Tg=500 ºC.

For the smaller pit diameters, the height of the ring decreases with growth: further growth on the surface leads the smaller features on the surface to decay. For the larger features on the surface, further growth leads to amplification of the height of ring. Therefore we observe similar regions of the amplification and decay as Shah et. al. reported for the growth at 600 ºC (See fig. 3.9).

4.2.2 Growth mode versus Growth Temperatures (Fine Growth Steps):

We next attempted to determine whether the change in growth mode visible in Fig. 4.4 and 4.5 is in fact coincident with the thermodynamic pre-roughening transition. To do this we performed a set of growth experiments at a series of temperatures between 500 °C and 600 °C. Fig. 4.7 shows the results of growing films 100 nm thick at 500 °C, 525 °C, 560 °C and 580 °C on a part of the surface patterned with 0.7 μm diameter pits, spaced at 1.4 μm. These experiments were carried out using a moderate As_2 flux (2.8 x 10^{-5} mbar), at the same growth rate as previously (0.323 nm/sec). It is clear that the ring

disappears somewhere between 525 °C and 560 °C. We can divide the growth mode in two regimes, below 525 °C where the rings appear around pits during growth and above 560 °C where no rings form. To quantify the change in growth mode, we again measured height profiles across the pits; these are shown in Fig. 4.8; the rings are visible as peaks at the edges of the pits. The presence of the rings results in a net concave upward curvature in the profiles between pits. This net curvature reverses sign at the higher growth temperature, and thus serves as a useful measure of the change in growth mode. As seen in the red curve in Fig. 4.9, we find the temperature at which the mode changes at 542.5 $\pm$ 17.5 ºC. This coincides with the preroughening temperature of 537$\pm$ 13ºC at this As_2 flux, to within the uncertainty of the determinations.

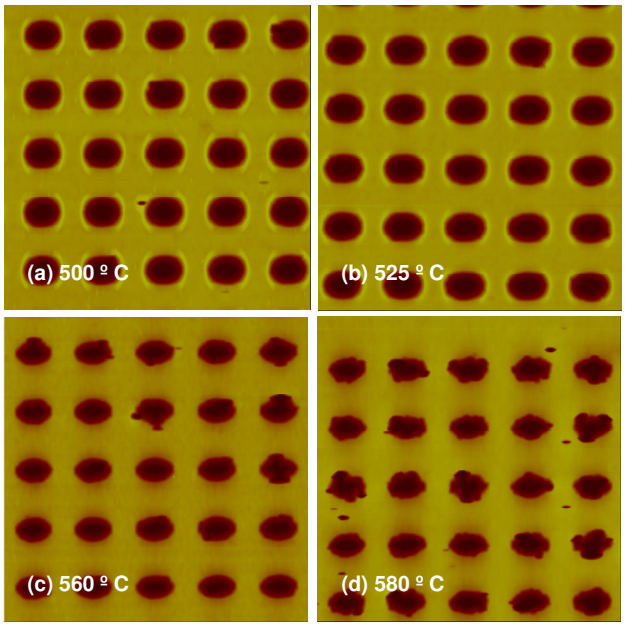

Fig. 4.8 AFM image from 1.4 μm pit diameter 2.8 μm spacing area after 100nm growth with "moderate" As_2 flux at (a) 500 °C, (b) 525 °C, (c) 560 °C and (d) 580 °C. Field of view is 7.5 μm X 7.5 μm. Vertical range is 100 nm full scales.

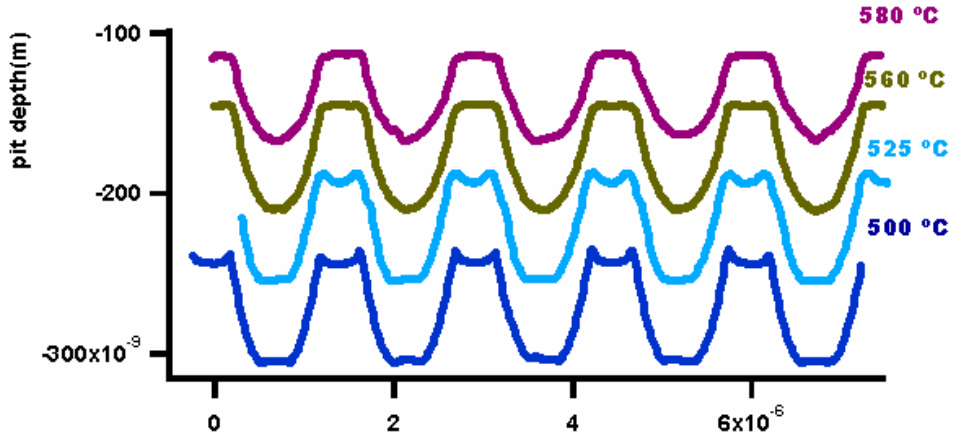

Fig. 4.9 Line profiles across the pit structure along [110] for growth of 100 nm of GaAs at different temperatures and Moderate As_2 flux conditions (2.8 x 10^{-5} mbar).

The simple coincidence of the two transition temperatures at a particular As_2 flux, while suggestive, does not clearly demonstrate that preroughening drives the change in growth mode. A more stringent test of whether such a cause and effect relationship exists comes from the As_2 flux dependence of the two transitions. We therefore measured the dependence of the growth mode transition temperature on the flux for comparison with that shown in Fig. 4.3 for the preroughening onset temperature. We repeated the growth experiments on a patterned substrate for an As_2 flux one half of that for Fig. 4.8 and Fig. 4.9 at a series of temperatures ranging from 500 ºC to 620 ºC. We again assigned the growth mode transition temperature to be that at which the sign of the net curvature of height profiles between rings measured along [110] reverses. The blue and red curves in Fig. 4.10 shows a comparison of the fitted radius of curvature between pits versus temperature from profiles, at the two different As_2 fluxes.

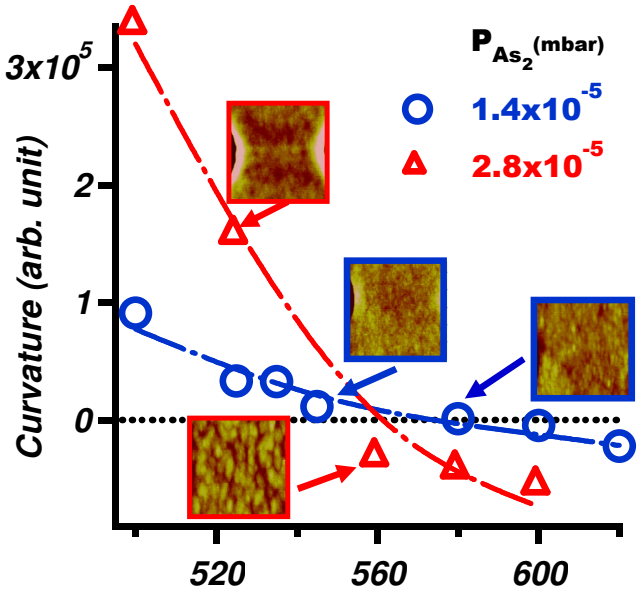

Fig. 4.10 Fitted curvature from height profiles measured between pits, along [110], vs. temperature after growth of a 100 nm thick GaAs film on a part of the substrate patterned with 0.7 μm diameter pits spaced at 1.4 μm center–to-center spacing. Growth was performed under moderate As_2 flux conditions ($2.8x10^{-5}$ mbar, red curve) and half this flux (blue curve).

The result is the opposite of what would be expected if preroughening were responsible for the change in growth mode. As we have shown in the previous section, doubling the As_2 flux, from $1.4x10^{-5}$ mbar to $2.8x10^{-5}$ mbar results in an *increase* in the thermodynamic pre-roughening onset temperature of approximately 28 ºC. As seen in Fig. 4.10, for the growth mode opposite trend is observed. For the same change in As_2 flux the temperature at which the surface curvature between pits crosses zero *decreases* by 28 ºC, from 570 ±10 ºC to 542.5±12.5 ºC. We conclude that the pre-roughening can not be responsible for the growth mode change.

4.2.3 Surface reconstruction:

It is clear from the results presented in the previous section that the change in growth mode can not simply be attributed to thermodynamic pre-roughening. An alternative explanation might be based upon the known change in the surface reconstruction which occurs at a temperature near that in which we observe the change in growth mode. Studies by Ding and Labella [86] and Ohtake [52] indicate that the surface reconstruction of GaAs(001) surface also changes as a function of arsenic pressure and temperature. In fact the reason of this growth mode change might be because of the change in the surface reconstruction. We heated the GaAs(001) surfaces after removing the oxide thermally and grew a buffer layer of 0.4 μm GaAs under "moderate" As_2 pressure. We found that the surface reconstruction changes from β_2(2x4) to c(4x4) upon cooling below approximately 545 ºC, by observing where the quarter order beam intensity along [110] decreases to zero and quarter order beams along [001] appears. This is summarized in Fig. 4.11.

We repeated this experiment for one half our normal As_2 growth flux; the result, in the form of the intensity of the β_2(2x4) ¼-order beam vs temperature for the two As_2 fluxes, is shown in Fig. 4.12.

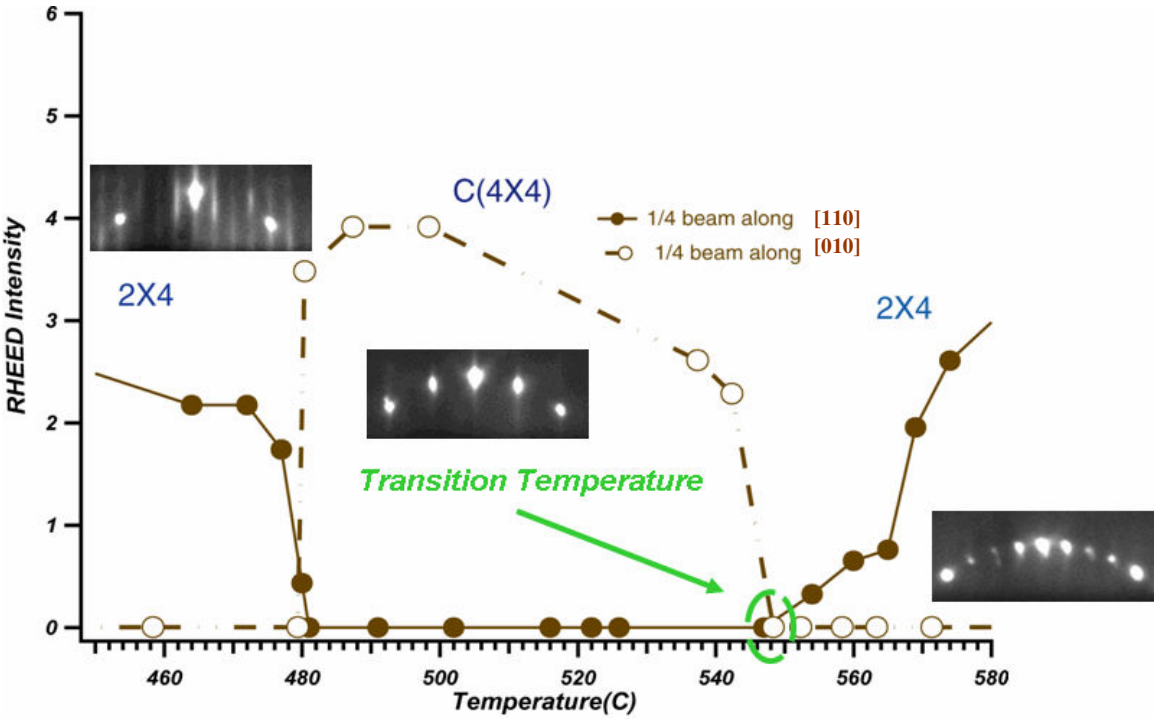

Fig. 4.11 ¼ -Order RHEED Intensity versus substrate temperature. The reconstruction changes from β_2(2x4) to c(4x4) upon cooling through 545 ºC. The second transition which is from c(4x4) to β_2 (2x4) is related to closing the As valve below that temperature, as described in section 1.3.1.

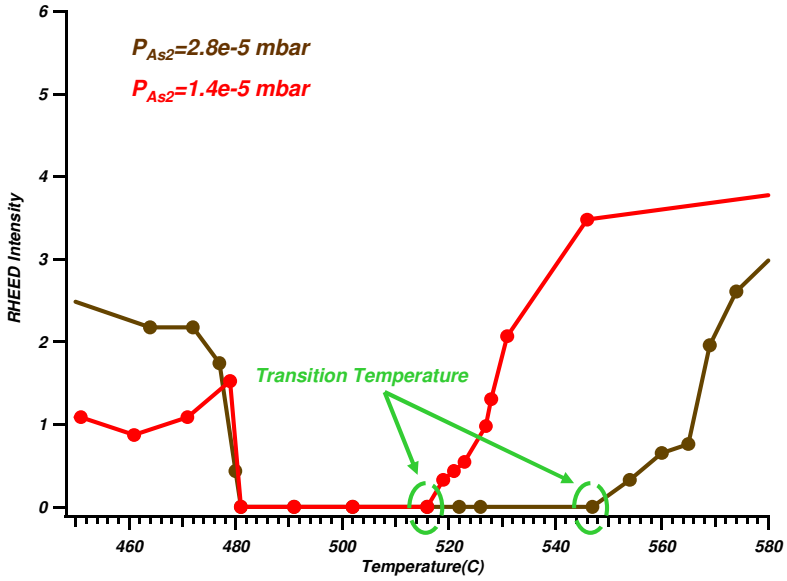

Fig. 4.12 Intensity of ¼ order RHEED beam along [1̲10] versus substrate temperature. The reconstruction transition temperature shifts to the lower temperatures with reducing the As_2 pressure.

The surface reconstruction transition temperature shifts to the lower values as we reduce the As_2 pressure as shown in Fig. 4.13. This is again in the *opposite* direction of that shown in Fig. 4.10; therefore the change in reconstruction can not be responsible for growth mode change.

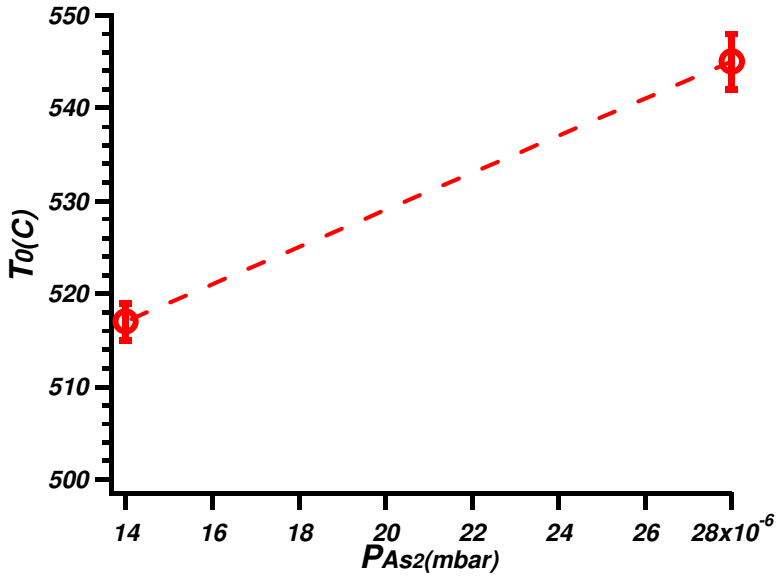

Fig. 4.13 Change in the reconstruction transition temperature with As_2 pressure. As the As_2 pressure increases the transition temperature also increases.

4.2.4 Island Shapes: Ring formation and Evidence for Ehrlich-Schowebel Barrier

Having ruled out the possibility that the growth mode change is driven by either thermodynamic preroughening or the c(4x4) to β_2(2x4) transformation, we consider the possibility that it results from kinetic effects. To investigate this possibility, we carried

out additional experiments, involving much smaller increments in grown film thickness on our patterned surface, and examining the AFM images carefully to see how the rings form on the surface. To minimize the extrinsic roughness, before growth atomic hydrogen-assisted oxide desorption was carried out at 300 ºC for about 40 minutes, followed by annealing the surface at 580 ºC for one hour under a "moderate" As_2 flux(2.8 x 10^{-5} mbar).

Some results from these growth experiments are illustrated in Fig. 4.14. Fig. 4.14(a1) and 4.14(a2) show two different regions of the initial surface after annealing, but before growth. They are for regions between the pits along [110] and along [$\underline{1}$10], respectively; there are relatively big islands on the surface as the result of annealing above the pre-roughening temperature and a fairly slow cooling subsequent to this. Figs. 4.14(b1) and 4.14(b2) show corresponding images of the surface after growth of a GaAs layer with 1 nm in thickness at a lower temperature, 500 ºC. The surface is now covered with both large islands, (which remain from the starting surface after annealing, and slow cooling) and very small islands, which form during the growth. As we show below, the density of these islands in not uniform; the variation in density provides information on the local density of adatoms during growth. Fig. 4.14(c1) and 4.14(c2) are for 3 nm of growth at this same temperature; the big islands have become larger and have begun to coalescence. Regions bounding the pit along $\pm$ [$\underline{1}$10] are nearly free of small islands. Fig. 4.14(d1) and Fig. 4.14(d2) show AFM images after 6 nm of growth. By this point, the smaller islands resulting from growth have visibly begun to coalescence and there are voids on the surface, presumably as a result of incomplete coalescence. In Fig. 4.14(d1) we begin to see the first stages of ring formation, through island coalescence, at edges

bounding pits along both $\pm$ [110]. A further increase in height of the by now fully formed rings is seen after growth of 100 nm as shown in Fig. 4.14(e1). Again, these are completely absent along [$\bar{1}$10]-type edges as seen in Fig. 4.14(e2).

For comparison, a series of AFM images for a similar regions and the same As_2 flux, but at a temperature of 600 ºC, is shown in Fig. 4.15. Figs. 4.15(a1) and 4.15(a2) again show the starting surface after annealing, for ease of comparison. The surface topography resulting from growth of 1 nm of GaAs at this higher temperature is shown in Figs. 4.15(b1) and 4.15(b2), here small islands appear on regions away from the pits. As shown below, denuded zones exit near edges bounding pits along $\pm$ [110] and $\pm$ [$\bar{1}$10] directions, and indicates the absence of a significant effect due to an Ehrlich-Schwoebel barrier for step bunches along both [110] and [$\bar{1}$10]. The initial large, anisotropic islands which resulted from annealing the starting surface have nearly completely coalesced. The results of growing a much thicker layer, 10 nm, are shown in Fig. 4.15(c1) and 4.15(c2). In Fig. 4.15(c1) "A-type" steps[55], i.e. those running parallel to [$\bar{1}$10] have essentially disappeared, leaving predominantly rippled "B-type" steps [55](parallel to [110]).

Based upon Figs. 4.14 and 4.15 we learn that at 500 ºC, rings form at the edges bounding pits along ± [110] by the coalescence and stacking of islands, while at 600 ºC no such coalescence and stacking occurs. This observation alone argues against thermodynamic preroughening as the driving force for the change in growth mode that we observe. The signature of the preroughening transition is an increase in island density at high temperatures, while the island coalescence which is responsible for ring formation occurs at low temperatures, below T_P.

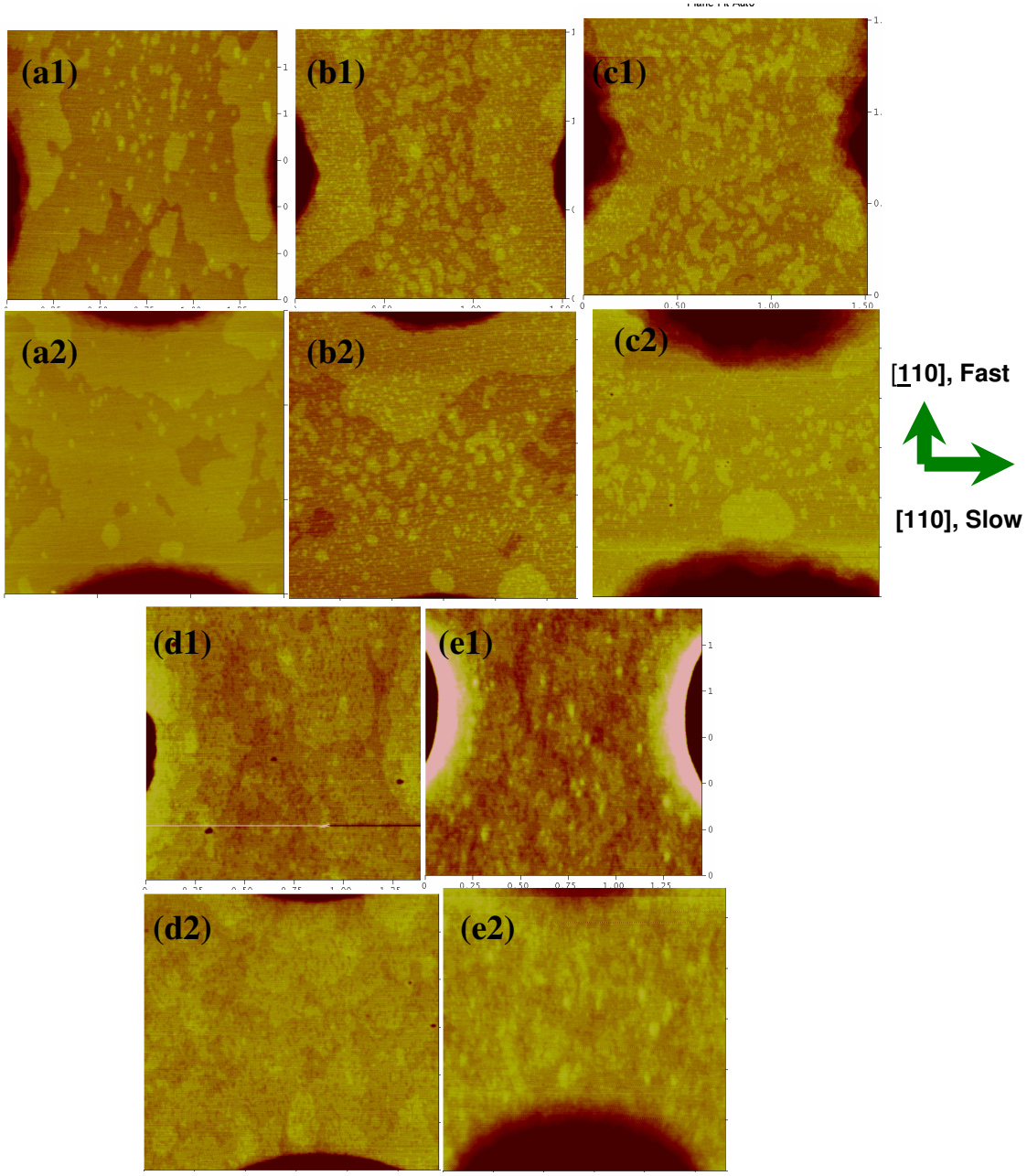

Fig. 4.14 AFM images of regions between 1.4µm diameter pits spaced at 2.8 nm (a1), (a2) no growth, (b1), (b2) after 1 nm growth, (c1), (c2) after 3 nm growth (d1), (d2) after 6 nm (e1), (e2) after 100 nm growth. (a1) (b1) (c1), (d1) and (e1) are scanned along [110], (a2), (b2), (c2), (d2) and (e2) are scanned along [1̄10]. Growth was done at 500 ºC. Ga (BEP) =2.6 x 10^{-6} mbar, As_2 (BEP) =1.4 x 10^{-6} mbar. Field of view is 1.5 µm x 1.5 µm. The range of heights is 5 nm full scale.

We now show that the change in growth mode is consistent with an anisotropic multiple ES barrier at this lower temperature [32, 87, 71]. Such a barrier would need to be small, in that thermal promotion across it changes noticeably over the temperature range 500 ºC – 600 ºC. It would also need to be anisotropic, since we observe that the island stacks which form the rings occur only at edges bounding pits along ±[110] directions; furthermore the shapes of the stacks are elongated along the orthogonal [$\underline{1}$10] direction. The absence of growth mounds away from the edges is further evidence for the weakness of the ES barrier in this case, and suggests a collective effect due to densely packed steps [87].

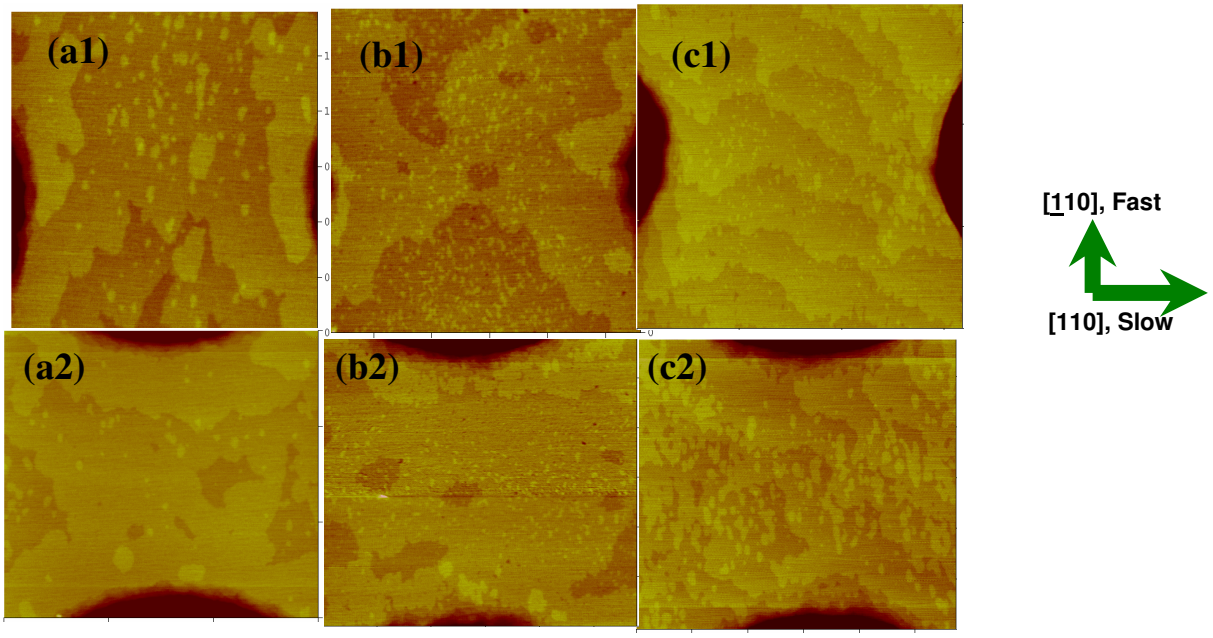

Fig. 4.15 AFM images of regions between 1.4 µm diameter pits spaced 2.8 µm (a1), (a2) No growth; (b1), (b2) after 1 nm growth; (c1), (c2) after 10nm growth. Growth was at 600 ºC. Ga BEP=2.8 x10 $^{-6}$ mbar, As_2 BEP=1.4 x10 $^{-5}$ mbar. Field of view is 1.5 µm x 1.5 µm. the range of heights is 5 nm full scale.

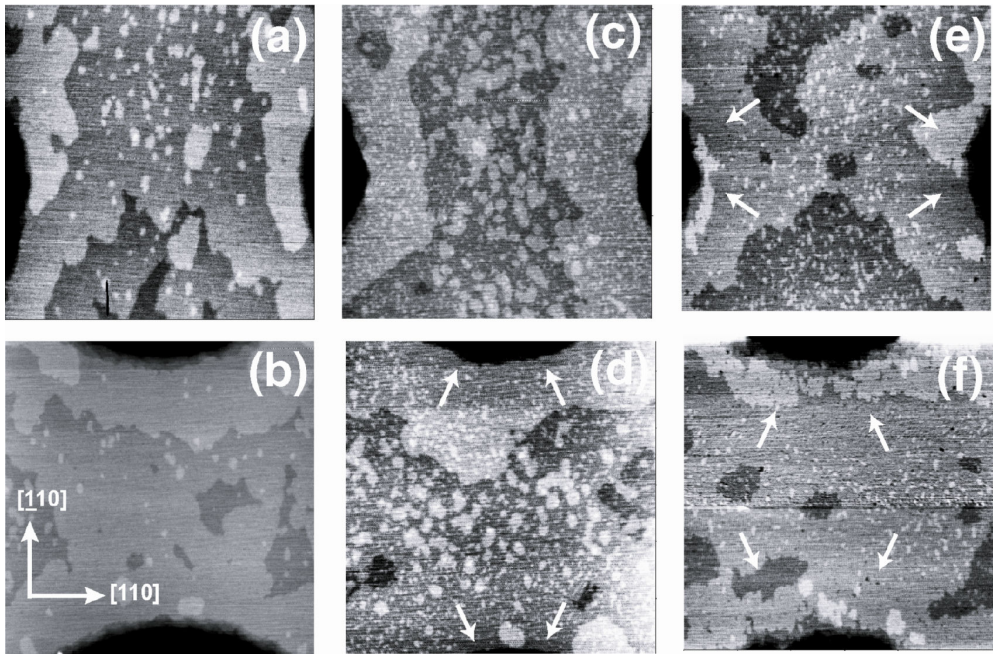

Fig. 4.16 AFM images of regions between pits (a, b) after annealing for 1 hour at 580 °C, but before MBE growth; (c, d) After growth of 1 nm at an As_2 flux BEP of 1.4 x 10^{-5} mbar and a temperature of 500°C; (e, f) After growth of 1 nm at an As_2 flux BEP of 1.4 x 10^{-5} mbar and a temperature of 600 °C. For all images, the field of view is 1.4 μm. The arrows in (d), (e), and (f) indicate zones denuded of small growth islands near the pit edges.

We in fact see evidence for such a barrier from AFM edges in the very early stages of growth. Fig. 4.16(a) and 4.16(b) are images scanned after annealing for one hour at a temperature of 580 ºC, but before growth. The large islands result from preroughening, followed by coalescence. Fig. 4.16(e) and 4.16(f) show the surface after growth of 1 nm of GaAs, at a temperature of at 600 ºC, in regions bounding pits along [110] and [1̄10], respectively. The surface now contains a moderate density of small islands, in addition to the larger island which resulted from annealing. The regions immediately adjacent to the pit edges however are nearly "denuded" of such small islands, as seen clearly in Figs. 4.17(c) and 4.17(d), where the density of these islands is plotted in the vicinity of [110]

and [1̲10], respectively. Thus at this temperature adatoms close to pit edges are relatively free to diffuse downward across, and attach to the bunched steps which form the pit walls, rather than coalescing to form islands; in this case there is no qualitative evidence for the effect of an ES barrier. Similarly, in Fig. 4.16(e) the AFM image acquired after growth of 1 nm in the region between pits along [1̲10] shows a small denuded zone, visible in the island density plot of Fig. 4.17(b). Contrasting behavior is seen in Fig. 4.16(b), and in the island density plot of 4.17(a) where the islands extend up to [110] pit edges, consistent with the effect of an anisotropic multi-step Ehrlich-Schwoebel barrier at this lower temperature.

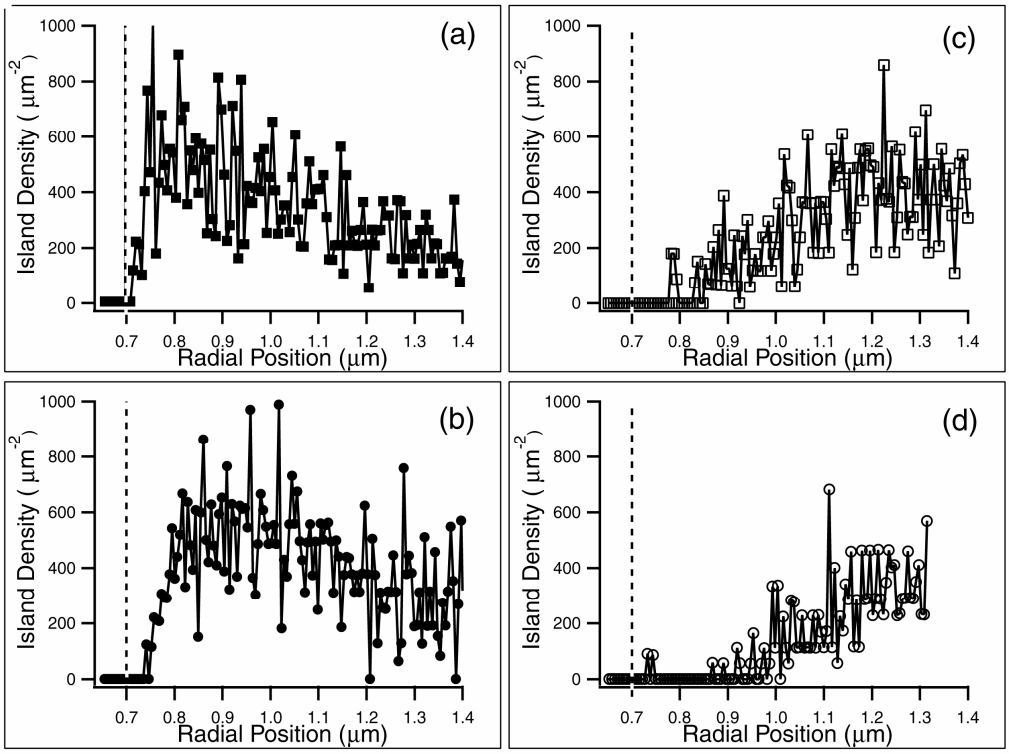

Fig. 4.17 Density of small growth islands vs. radial position, with respect to pit center, after growth of 1 nm GaAs at an As_2 flux BEP of 1.4 x 10^{-5} mbar, determined from Fig. 3. (a) Growth temperature T_G = 500ºC, island density determined over azimuthal range [110]+/- 45º. (b) T_G = 500 ºC, azimuthal range [1̲10]+/- 45º. (c) T_G = 600 ºC, island density determined over azimuthal range [110]+/- 45º. (d) T_G = 600ºC, azimuthal range [1̲10]+/- 45º. The dashed lines show the position of the pit edges in all cases.

Next we consider the behavior shown above in light of our previous observations [74, 71] that the detailed evolution of the surface morphology that we observe during MBE growth on these patterned GaAs(001) surfaces at high temperatures is consistent with the modified, mass conserving form (CKPZ) of the Kardar, Parisi and Zhang [5] equation proposed by Sun, Guo and Grant [72]:

$$\frac{\partial h}{\partial t} = -\nabla^2 \left[\upsilon_x \cdot \frac{\partial^2 h}{\partial x^2} + \upsilon_y \cdot \frac{\partial^2 h}{\partial y^2} + \lambda_x \cdot \left(\frac{\partial h}{\partial x} \right)^2 + \lambda_y \cdot \left(\frac{\partial h}{\partial y} \right)^2 \right] + \eta, \quad (4.1)$$

A common criticism of this and related continuum models is their phenomenological nature. We now show that the change in the growth mode with temperature provides an important insight as to the physical processes corresponding to Eq. (4.1). In the CKPZ equation the sign of λ_x and λ_y is taken to be positive. Reversing the sign of the nonlinear terms, as suggested by Lai and Das Sarma [81] (LDS), results in nearly isotropic rings of material building up around the pit initially during growth [74]. While this latter prediction is quite different from our observations at temperatures above the growth mode transition T_G, it is qualitatively consistent with those below T_G, along the [110] direction. Therefore reversing the sign of the non-linear term along the [110] direction gives us results qualitatively consistent with our experimental observations as shown in Fig. 4.17 which shows the results of a simulation based on the “mixed" model.

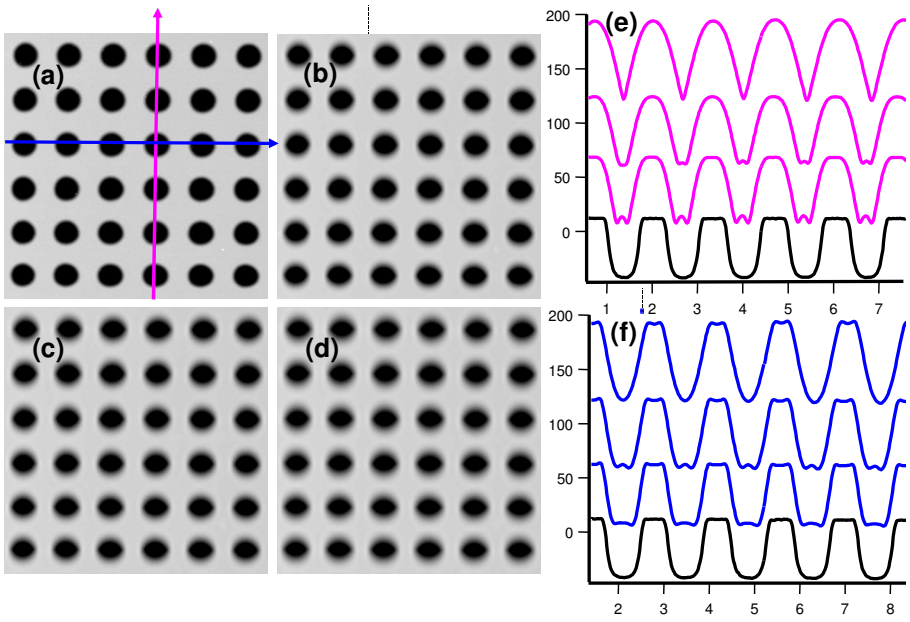

Fig. 4.18 Simulation based on the mixed model, initial patterned surface (a), for simulation after 100s (b), 200s (c) and 400s (d)and line profiles at center of the pit structure along [1̲10] direction (e) and along [110] direction (f). $v_x=10^3\ nm^4/s$, $v_y=5x10^3\ nm^4/s$, $\lambda_x/2=10^3\ nm^3/s$, $\lambda_y/2=10^4\ nm^3/s$.

Fig. 4.18 shows that the mixed model predicts as an evolution of the surface morphology quite consistent with the experimental results for growth at low temperature (500 ºC). Fig. 4.18(b)-(d) shows how the initial surface (a) evolves with simulation based on this model. The anisotropic rings are clearly shown in fig. 4.18(d), also in the line profile along the slow evolving direction, i.e. [110] as the spikes at the edge of the profiles indicates the rings.

The profile along [1̲10] direction indicates the formation of the cusps, which is similar to the experimentally observed behavior.

We have argued in chapter 3 that the nonlinear terms, which break the up-down symmetry of the equation, are consistent with the Zeno effect proposed by Elkinani and

Villain [4.19] and based upon Villain's ansatz that the adatom density can be written as $\rho = \rho_0 + \rho_1 \cdot (\nabla h)^2$ [88]. Since the surface adatom flux, $\vec{j} \propto -\nabla\rho$, and $\frac{\partial h}{\partial t} = -\nabla \cdot \vec{j}$, a negative value of ρ_1, corresponding to a local depletion of adatoms near where the pit bottoms intersect the side walls leads to the CKPZ form. We note that a multi-step Ehrlich-Schwoebel barrier [73] also breaks the up down symmetry of the problem, but results in the opposite trend, i.e. an increase in the local adatom density near descending steps, leading to a positive contribution to ρ_1. At low enough temperatures, this effect becomes dominant, at least along [110], and the sign of the nonlinear term along this direction reverses, leading to the formation of the rings along the top edges of the pits. This model provides a physically based explanation for the good agreement, over a range of temperature, flux and lateral length scales that we observe between our results and the predictions of what, until now has been a phenomenological model for growth.

An interesting final issue is whether the multiple ES barrier which we see evidence for bunches along [110] is finite along [$\underline{1}$10], i.e. the faster evolution direction. To address this we carried out growth at a temperature far below where MBE growth is typically done, 230 ºC. Our results are consistent with a finite, but smaller, multiple ES barrier along [$\underline{1}$10] as well as [110]. Fig. 4.18 shows how the individual pits evolve during the growth at three different temperatures, 600 ºC, 500 ºC and 230 ºC. At high temperature, the pits evolve anisotropically along [$\underline{1}$10] and [110] directions resulting in an ellipsoidal shape after 100 nm growth at 600 ºC. Further growth causes a relaxation of the pit topography, with no sign of ring formation at all at this temperature. For growth at 500 ºC, we again see the formation of the anisotropic ring along [$\underline{1}$10] crystalline direction. In addition, the anisotropic change of the pit shape leads to ellipsoid shape of

the pit. As shown earlier in this chapter, with further growth the ring expands and gets thicker in the middle along [110] than the sides. Reducing the growth temperature to 230 ºC leads to formation of isotropic ring around the pit consistent with an ES barrier along both [1̲10] and [110]. Interestingly, the pit remains nearly circular during growth at this temperature as well as an essentially circularly shaped pit.

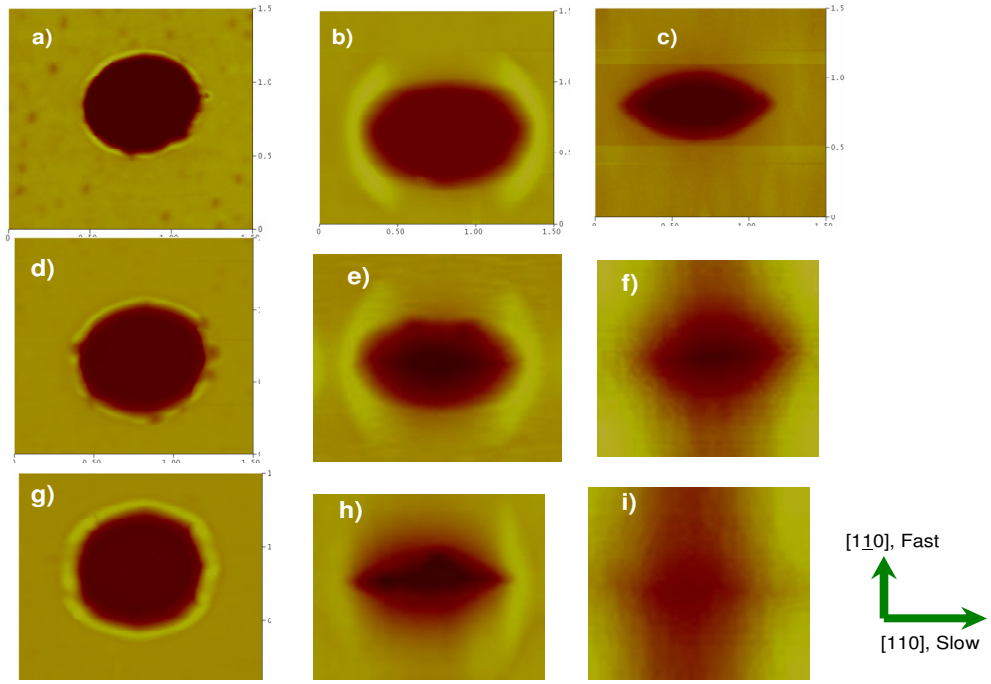

Fig. 4.19 AFM image of individual 0.7㎛m diameter pit, after growth at (a) 100 nm, 230 ºC, (b) 100 nm 500 ºC, (c) 100 nm 600 ºC, (d) 200 nm 230 ºC, (e) 200 nm 500 ºC (f) 500 nm 600 ºC, (g)100 nm 230 ºC (h) 500 nm 500 ºC, (i) 500 nm 600 ºC.

To summarize the major experimental results of this thesis, MBE growth on patterned GaAs (001) shows complex transient behavior, with a dramatic change in the mode evolution on cooling through a temperature approximately coinciding with the thermodynamic preroughening transition. We find that this behavior is consistent with

the predictions of the CKPZ model at high temperatures, but that the sign of the nonlinear term in the height equation reverses along [110] beneath ~550 ºC. Based on this, we propose a simple, physically based model involving a competition between decreased adatom collection rate during growth on small terraces [71, 79, and 4.21] and a small anisotropic multi-step Ehrlich-Schwoebel barrier. Undoubtedly, more complex models with additional effects, e.g. multiple types of diffusing species, and changes in diffusion length across transitions are possible. Further, it assumes that it makes sense to talk about steps in the presence of kinetic pre-roughening. Our results, along with the model we propose here provide new physical insight to the significance of the nonlinear term in a commonly evoked growth equation [72, 81, and 88] which describes our observations remarkably well, but until now has been phenomenological.

Chapter 5

Future work

In this chapter we will discuss possible future work which would help to understand or further test our explanation regarding the experimental observations which we have reported in chapters 3 and chapter 4, i.e. the instability during growth on patterned GaAs (001) surfaces and the change in the growth mode across the preroughening transition temperature.

5.1 Reducing the growth rate

As we reported in previous chapter, neither of two major thermodynamic effects, i.e. passing through the preroughening transition and a change in surface reconstruction can not explain the instability and the growth mode change that we reported during the homoepitaxial growth on patterned GaAs(001) surfaces. We proposed that the kinetic effects are responsible for driving these changes. To further test this proposition, one approach would be to conduct the growth closer to the equilibrium condition by reducing the growth rate. Reducing the growth rate would partially suppress the kinetic effects and therefore the instability that we see during the growth as well as the changing in the growth mode might be affected. A growth rate of one tenth of what we explored here would be practical for the thinnest films.

5.2 Exploring the pressure dependence of the kinetic effects

We proposed in chapter 4 that, a small, anisotropic and multistep Ehrlich-Shwoebel barrier along [110] direction which competes with the Zeno effect could drive the growth mode change. Reducing the As_2 flux, should in fact enhance the formation of the small islands very close to the pit edges which will remains even at higher growth temperatures. Plotting the island density very close to the pit edges along [110] crystalline direction as a function of As_2 pressure will confirm whether or not our guess regarding the mechanisms which drive the growth mode change is correct.

5.3 Evolution of the surface in Nano-Scale dependence

Another possibility is to reduce the lateral size of the features on the surface to the nano-scale and study the length scale dependence of the surface evolution during the growth. Using e-beam lithography, one could pattern the GaAs(001) surfaces with array of pits in the order of nanometer size. These features would be closer in size to the real initial roughness, resulting from oxide desorption as illustrated in chapter 2. Another advantage of creating the nano-scale features is that the smaller features would make Monte Carlo simulations including atomic scale effects practical.

Appendix A

Growth at 230 ºC

In this appendix we describe a series of growth experiments at a significantly lower temperature, 230 ºC. The fluxes were as in as table 4.1. The AFM images indicate the formation of an isotropic ring all around each individual pit. In Fig. A.1 AFM example image are shown and compared with those for growth at 500 ºC and 600 ºC for 100 nm thickness growth.

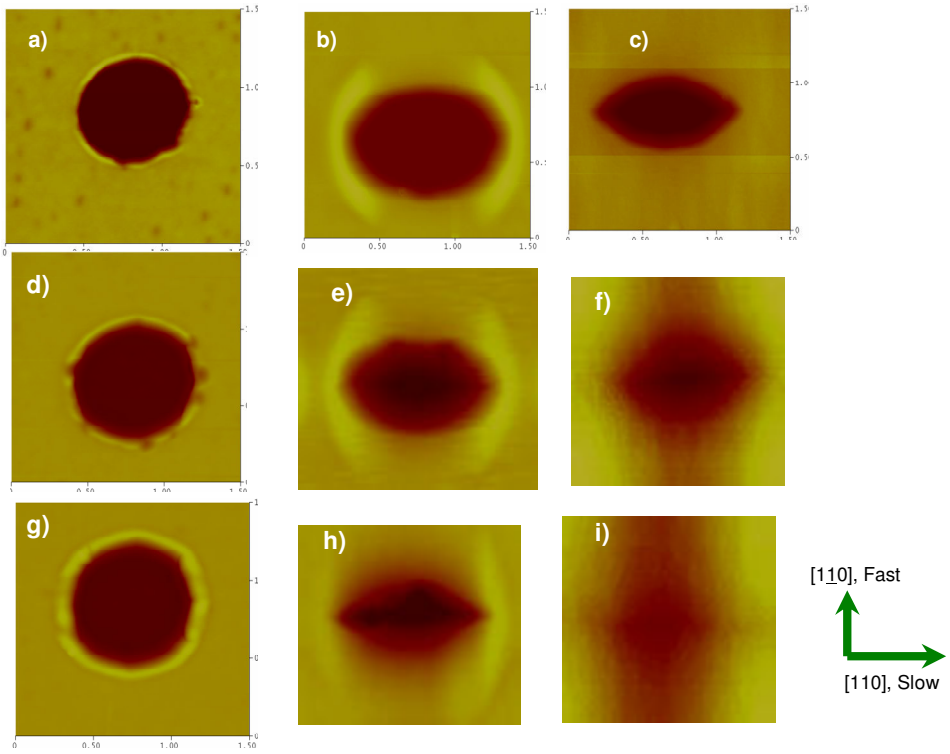

Fig. A.1 AFM image of individual 0.7 μm diameter pit, after growth at (a) 100 nm, 230 ºC, (b) 100 nm 500 ºC, (c) 100 nm 600 ºC, (d) 200 nm 230 ºC, e)200 nm 500 ºC (f)500 nm 600 ºC, (g)100 nm 230 ºC (h) 500 nm 500 ºC, (i) 500 nm 600 ºC.

As we increase the temperature from 230 ºC to 500 ºC the rings become anisotropic, as discussed in chapter 4, and finally completely disappear at temperatures above ~ 540 ºC.

This is consistent with a finite multistep ES barrier along [1̲10] as well.

We see the contrast in behavior more clearly in Fig. A.2, which shows line profiles of the individual pits along the [1̲10] direction. It is clear that material piles up along [1̲10] direction only at the lowest temperature, 230 ºC.

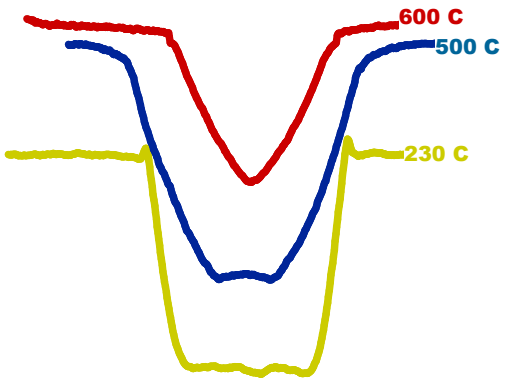

Fig. A.2 Line profiles across the center of a pit with initial diameter is 0.7 μm, after growth at 230 ºC, 500 ºC, 600 ºC; total growth is 100 nm: incident fluxes are As_2(BEP)=2.8 x 10^{-5} mbar, Ga (BEP)=2.8 x 10^{-6} mbar, Profile measured along [1̲10].

Fg. A.3 shows how the ring evolves with time (thickness) along [1̲10] direction for growth at 230 ºC.

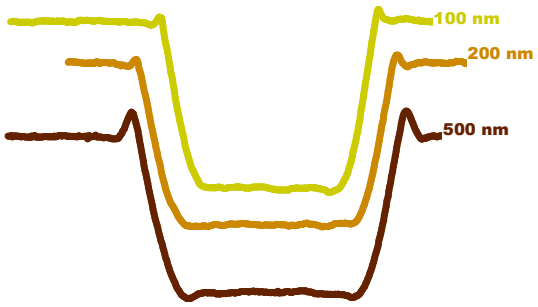

Fig. A.3 Line profiles across the center of one pit with initial diameter is 0.7 μm, at 230 ºC; total growth of 100 nm,200 nm and 500 nm. The incident fluxes are As_2 (BEP)=2.8 x 10^{-5} mbar, Ga (BEP)=2.8 x 10^{-6} mbar. Profile measured along [$\underline{1}$10].

As we continue to grow GaAs on the patterned surface the rings become thicker isotropically.

Appendix B

High-Flux Growth

In this appendix we show results for a set of growth experiments on patterned GaAs(001) surfaces at 555 ºC and 585 ºC for "high" As_2 flux (1.4 x 10^{-4} mbar).

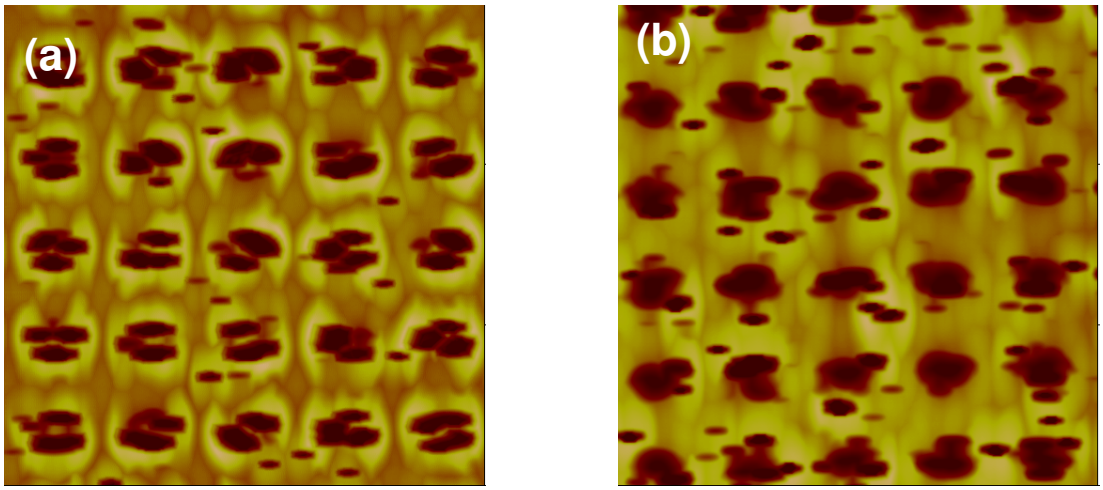

Fig. B.1 AFM images of patterned GaAs(001) for 0.7 μm pit diameter for growth Of 100 nm at (a) 555 ºC and (b) 585 ºC. Field of view is 7.5μm x 7.5μm and vertical range is 100 nm full scale.

Growth at these conditions produces a high concentration of defects. Their appearance is different from conventional "oval" defects, which are thought to be caused by Ga beads or droplets.

Appendix C

In this Appendix we show results for a set of growth experiments on patterned surfaces in which we used a complimentary mask to that we used in the main part of this thesis (fig. 2.1). Using a combination of photolithography and reactive ion etching we create array of cylindrical pillars with defined size and center to center spacing. Then using MBE we grow on the patterned GaAs (001) surfaces at the growth temperature of 580 ºC with the same As_2 and Ga (BEP) indicated in chapter 4, table 4.1. We grew total of 400 nm of GaAs on the patterned surfaces in 100 nm steps. After growth we scanned the

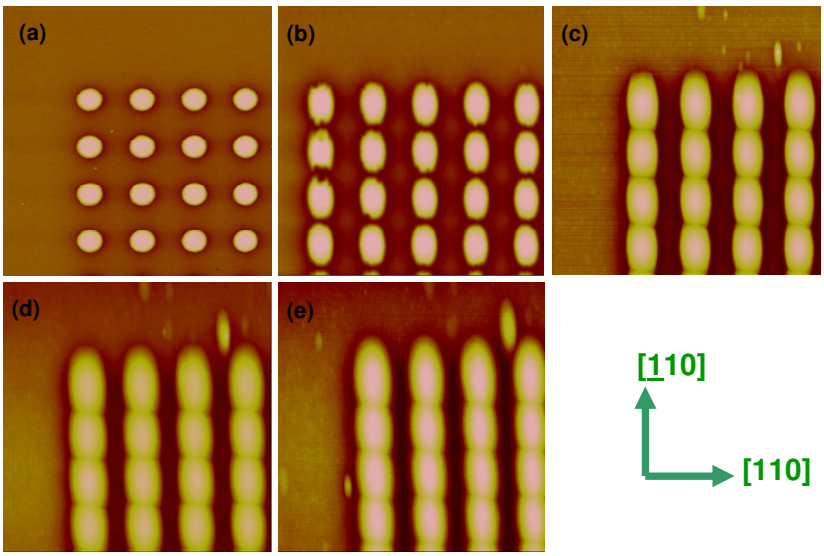

Fig. C.1 AFM images of the initial surface (a), after growth at 580 ºC with Ga(BEP)=1.6x10^{-6} mbar, As2 (BEP)=1.6x10^{-6} mbar for 100 nm growth (b), 200 nm growth (c), 300 nm growth (d) and 400 nm growth (e), the can size is 7.5 μm x 7.5 μm.

surface with AFM in tapping mode to see how the surface evolves. Fig. C.1 shows the AFM images for the growth of the smallest pillar size (0.7 μm with 1.4 μm spacing between the centers of the neighboring pillars) after different step of growth.

The pillar-patterned structure evolves anisotropically and faster along the [$\underline{1}$10] crystalline direction, which is consistent with what we see during the growth on pit-patterned structure (chapter 3 & 4). The pillars eventually merge together along fast evolving direction i.e., [$\underline{1}$10] as it is clear in Fig. C.2, where we show line profiles across the center of the pillars along both crystalline directions.

Fig. C.2 (a) indicates the formation of cusps between the pillars at early stages of growth which persist with further growth.

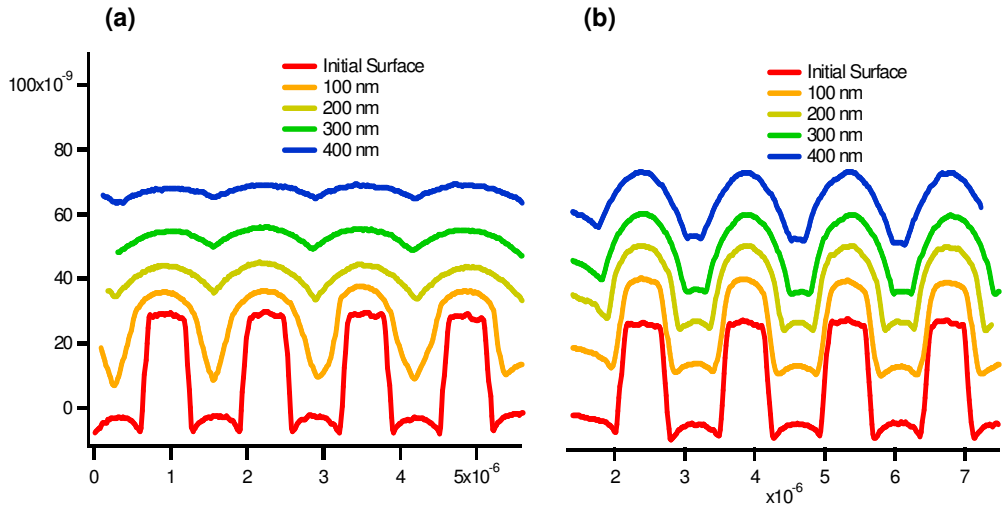

Fig. C.2 Line profiles across the center of pillars along [$\underline{1}$10] (a) and [110] (b), for different thickness of growth from 100 nm to 400 nm.

Profiles along both [110] and [$\bar{1}$10] crystalline directions show that pillars evolve to inverted paraboloids.

To distinguish between paraboloids and higher order polynomial, we took the first derivative of the line profiles . As shown in Fig. C.3 the first derivative is a straight line.

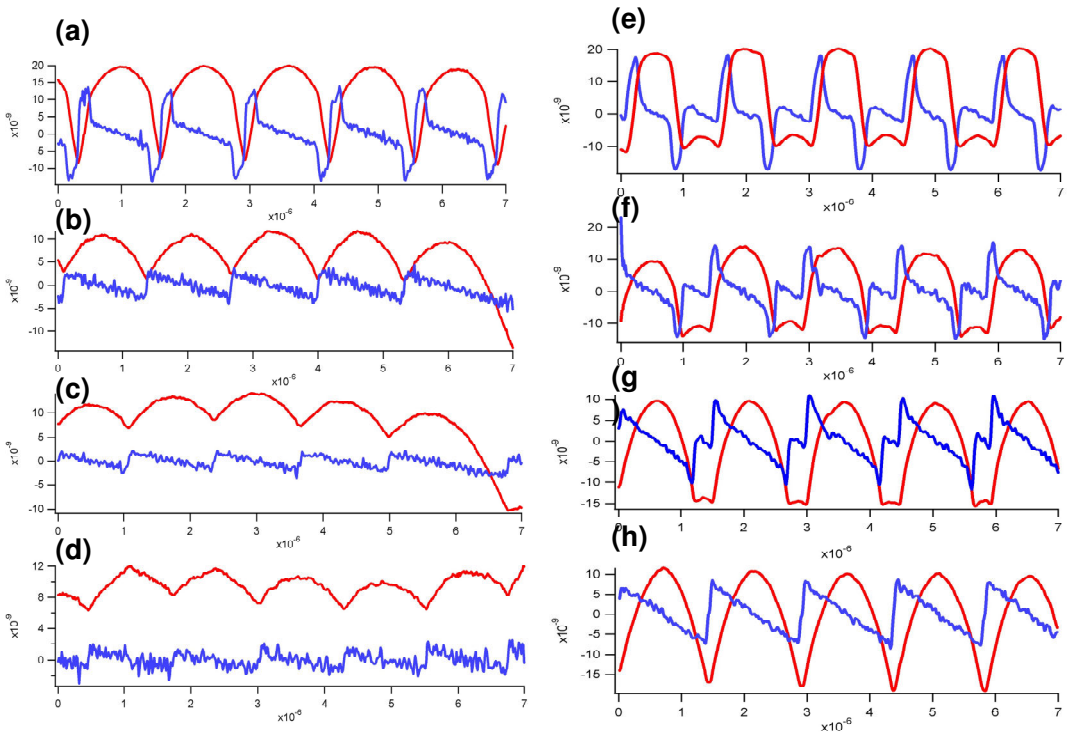

Fig C.3 The line profiles(red curves) and the first derivatives (blue curves) for profile along [$\bar{1}$10] crystalline direction (a)-(d) and along [110] direction (e)-(h). For 100 nm growth (a) and (e), 200 nm growth(b) and (f), 300 nm growth (c) and (g) and 400 nm growth (d) and (h).for pillar size of 0.7 μm and 1.4 μm spacing.

There is some noise in the slope of the derivative, but the major trend is towards a declining slope with increasing thickness. Based on our observation, all pillars will approach a simple parabolic shape which depends on the size of the pillar. The rate at which the pillar reaches this parabolic shape changes with lateral size.

We also performed simulations based on the CKPZ equation to propagate the starting AFM image forward in time, as discussed in chapter 3, 4. We compare the results of simulation with our the experimental results in Fig. C.4 and C.5.

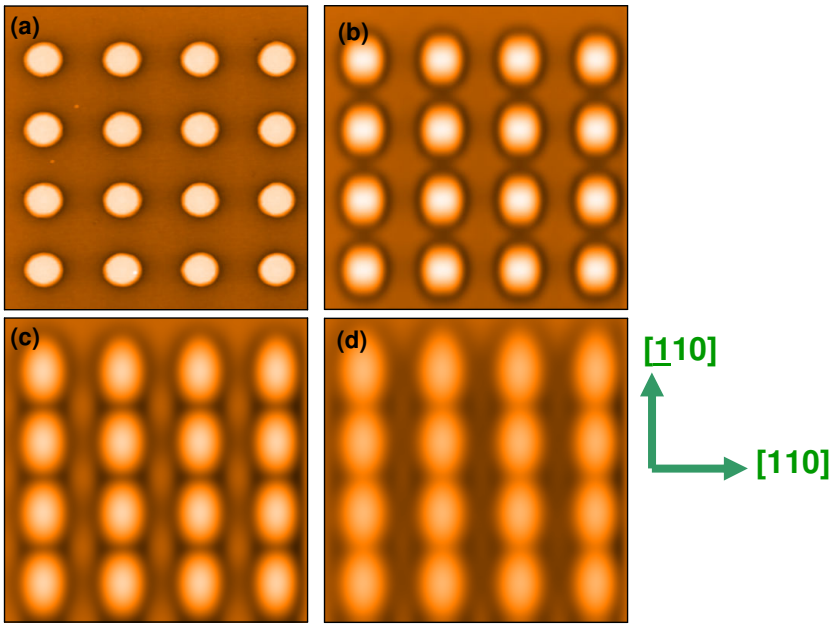

Fig. C.4. Initial patterned surface (a) along with images based on CKPZ equation for simulation after 800 sec (b), after 6400 (c), and after 19200 sec (d).Images size is 7.5 μm x 7.5 μm.

Fig. C.4 shows the simulated images based on integration of the CKPZ equation. The results are qualitatively in agreement with our experimental observations, Fig. C.1. Fig. C.5 shows line profiles and the first derivatives corresponding to the simulated images.

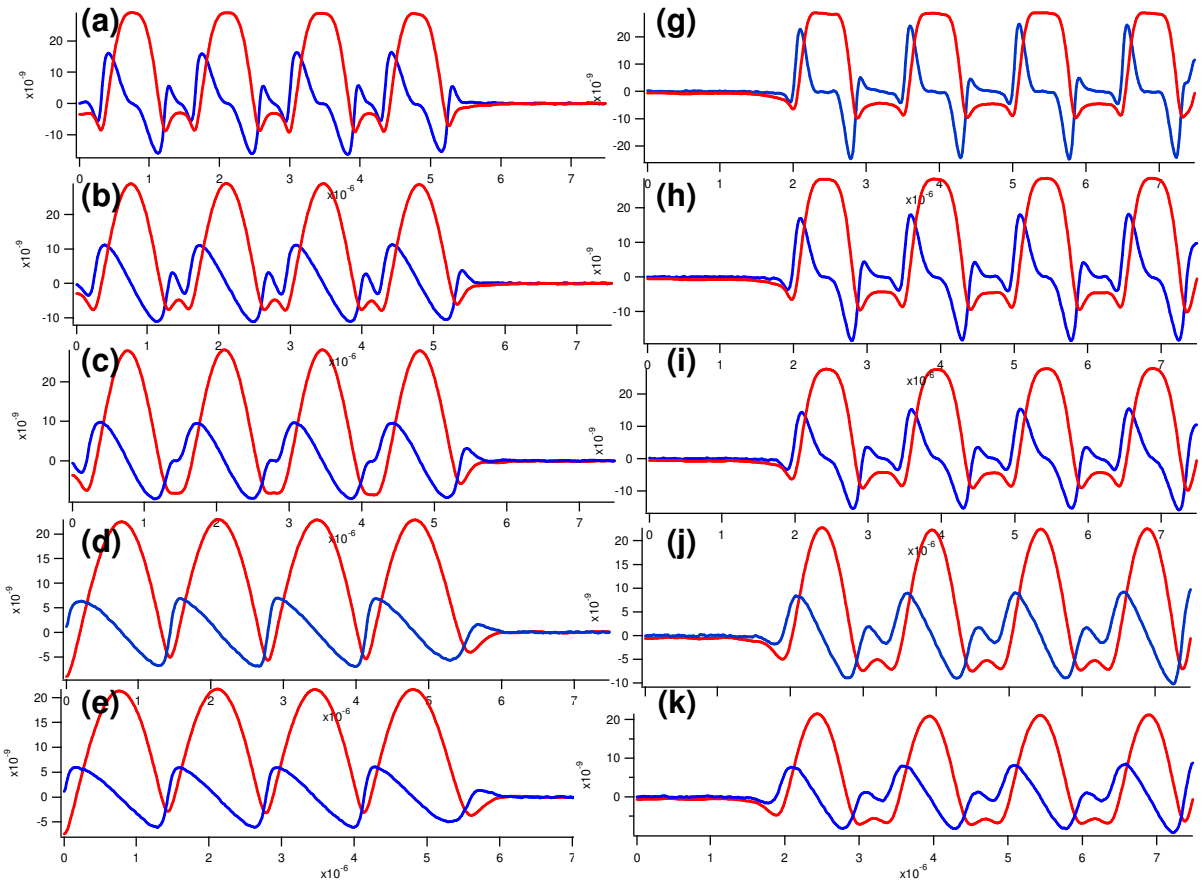

Fig. C.5 The line profiles(red curves) and the first derivatives (blue curves)for simulated images based on CKPZ model, for profile along [1̲10] crystalline direction (a)-(e) and along [110] direction (g)-(k).For 100 s (a) and (g), 400 s(b) and (h), 800 s (c) and (i), 4800 s(d) and (j), and 6400 s (e) and (k).

Comparing the experimental profiles from fig. C.3 and the simulated profiles, fig. C.5 we conclude that the trend towards a parabolic shape is consistent in both case. However, there is a difference in between those two profiles. In the profiles from our experimental results the parabola first forms at the top of each pillar and then spreads outward to the edges. The slope becomes constant in the middle of a pillar first and this region of constant slope then spreads out and merges to the neighboring pillars. On the other hand, the simulation shows the edges of the pillar broaden into a

parabolic shape and coalesce into the center. From the first derivative graphs (the blue curves) it is clear that regions of nonzero slope appear at the edges first and then the two lines corresponding to finite slope at the edges meet at the center and cause the inflection point which eventually become a straight line. Also the top of the pillar stays flat during the simulation until the edges meet during the growth.

A comparison of Fig. C.4 and C.1 shows that over longest simulation, nominally 6400s, corresponds to a relatively small total grown thickness, about 200-300nm. We might use this to calibrate the simulation time scale to that of the growth experiments, as follows:

$$t_{EXP} = \frac{250nm}{0.3nm/s} = 833s$$

For the growth of 250nm we need about 833 second which is almost correspond to 6400 s of simulation. Apparently, one second of the growth is almost corresponding to ~8 second of the simulation. Fig. C.6(a) shows the curvature of the line profile measured on the top of the pillars scanned in [$\underline{1}$10] direction as a function of thickness of growth, all pillars seems to approach the same value. Similar trend is also suggested by the plots of curvature in [110] direction shown in Fig. C. 6(b). This implies that during the growth the top of the pillars evolved to the same paraboloidal shape in spite of initial diameter.

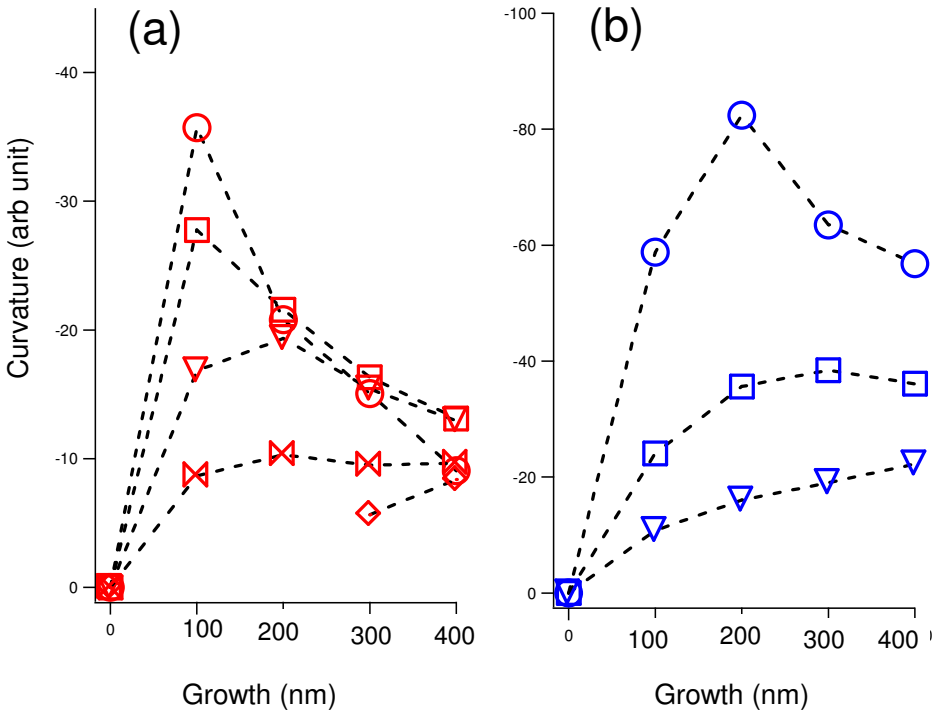

Fig. C.6 Pillar curvature vs growth thickness for curvature measured along [1̲10], (a) and along [110], (b).

References

[1] J. Rutkowski, L. Kubiak, J. Wenus, "Epilayers and Heterostructures in Optoelectronics and Semiconductor Technology": International Conference on Solid State Crystals,(SPIE, Bellingham, WA 2001).

[2] S. Shah, T. J. Garrett, K. Limpaphayom, T. Tadayyon-Eslami, H. C. Kan & R. J. Phaneuf," A Patterning-Based Investigation of the Length-Scale Dependence of the Evolution of the Interfaces during GaAs/ AlAs Multilayer Growth". Appl. Phys. Let. 83, 4330 (2003).

[3] Sonam Shah M.S. Thesis, University of Maryland College Park, MD, (2004).

[4] Z. Ding, D.W. Bullock, W.F. Oliver, P.M. Thibado, V.P. LaBella,"Dynamics of Spontaneous Roughening on the GaAs(001)-(2x4) Surface", Journal of Crystal Growth, 251 35–39 (2003).

[5] T. Sun, H. Guo and M. Grant," Dynamic of Driven Interfaces with a Conservation Law", Physical Review A, 40, 6763(1989).

[6] J. Tsao, "Materials Fundamentals of Molecular Beam Epitaxy", (Academic Press, San Diego, 1993).

[7] M. A. Herman and H. Sitter, "Molecular Beam Epitaxy: Fundamentals and Current Status"(Springer, Berlin, 1997).

[8] K. Ploog, "Molecular Beam Epitaxy of III-V Compounds" (Springer, Berlin, 1984).

[9] B. A. Joyce, D. D. Vvedenskey, A. R. Avery, J. G. Belk, H. T. Dobbs & T. S. Jones, " Nucleation Mechanisms during MBE Growth of Lattice-matched and Strained III-V Compound Films", Applied Surface Science 130-132 357 (1998).

[10] A. Ballestad, B. J. Ruck, M. Adamcyk, T. Pinningtaon & T. Tiedje, "Evidence from the Surface Morphology for Nonlinear Growth of Epitaxial GaAs Films", Physical Review Letters, 86, 2377 (2001).

[11] M. Adamcyk, A. Ballestad, T. Pinnington, T. Tiedje, M. Davis & Y. Feng, "Smoothing of Textured GaAs Surfaces during Molecular beam Epitaxy Growth", J. Vac. Sci. Technol. B 18, 1488 (2000).

[12] J. H. Neave and B. A. Joyce," Temperature Range for Growth of Autoepitaxial GaAs Films by MBE". J. Crystal Growth 43, 204 (1978).

[13] E. H. C. Parker, "The Technology and Physics of Molecular Beam Epitaxy", (Springer, Berlin, 1985), p. 54.

[14] V. P. Labella, Z. Ding, D. W. Bullock, C. Emery and P. M. Thibado, "A Union of the Real-Space and Reciprocal-Space View of the GaAs(001) Surface". Int. J. Mod. Phys. B, 15, 2301 (2001).

[15] Z. Ding, D.W. Bullock, and P.M. Thibado, V. P. LaBella & Kieran Mullen," Atomic-Scale Observation of Temperature and Pressure Driven Preroughening and Roughening", Phys. Rev. Lett. 90, 216109 (2003).

[16] G. Apostolopoulos, J. Herfort, L. Daweritz & K. H. Ploog," Reentrant Mound Formation in GaAs(001) Homoepitaxy Observed by ex situ Atomic Force Microscopy". Phys. Rev. Lett. 84, 3358 (2000).

[17] G. Lengel, R. J. Phaneuf, E. D. Williams, S. Das Sarma, W. T. Beard & F. G. Johnson, "Nonuniversality in Mound Formation during Semiconductor Growth". Phys. Rev. B 60, R8469 (1999).

[18] M. D. Johnson, C. Orme, A. W. Hunt, D. Graff, J. Sudijono, L. M. Sander, and B. G. Orr, "Stable and unstable Growth in Molecular Beam Epitaxy". Physical Review Letters 72, 116 (1994).

[19] J. Tersoff, M. D. Johnson, B. G. Orr, "Adatom Densities on GaAs: Evidence for Near Equilibrium Growth", Phys. Rev. Lett., 78, 282 (1997).

[20] C. Orme, M. D. Johnson, J. L. Sudijono, K. T. Leung, B. G. Orr, " Large Scale Surface Structure Formed during GaAs(001) Homoepitaxy", Appl. Phys. Lett. 64, 860 (1994).

[21] M. Adamcyk, T. Pinnington, A. Ballestad & T. Tiedje, "Effect of the Starting Surface on the Morphology of MBE-Grown GaAs". Materials Science and Eng. B 75, 153 (2000).

[22] N. Haider, M. R. Wilby & D. D. Vvedenskky, " Epitaxial Growth Kinetics on Patterned Substrates". Appl. Phys. Lett. 62, 3108 (1993).

[23] A. Dalla Volta, D. D. Vvedenskey, N. Gogneau, E. Pelucchi, A. Rudra, B. Dwir, E. Kapn & C. Ratsch, " Step Ordering Induced by Nonplanar Patterning of GaAs Surfaces", Appl. Phys. Lett., 88 23104 (2006).

[24] R. J. Phaneuf, E. D. Williams and N. C. Bartelt, "The Temperature Dependence of Vicinal Si(111) Surfaces", Phys. Rev. B 38, 1984 (1988).

[25] R. J. Phaneuf and E. D. Williams," Surface Phase Separation of Vicinal Si(111)", Phys. Rev. Lett. 58 2563 (1987).

[26] P. Politi, G. Grenet, A. Marty, A. Ponchet and J. Villain, "Instability in Crystal Growth by Atomic or Molecular Beams", Phys. Rep. 324, 27 (2002).

[27] E. I. Altman, M. Bienfait, H. P. Bonzel and R. Diehl, “Adsorption on Surfaces and Surface Diffusion”, (Springer, Berlin, 2001).

[28] A. Kley, P. Ruggerone & M. Scheffler, “Novel Diffusion Mechanism on the GaAs(001): The Role of Dimer Interaction”, Phys. Rev. Lett. 79, 5278 (1997).

[29] P. Kratzer and M. Scheffler,” Reaction Limited Island nucleation in Molecular Beam Epitaxy of Compound Semiconductors”, Phys. Rev. Lett. 21, 036102 (2001).

[30] T. Michely & J. Krug, in “Islands, Mounds and Atoms, Patterns and Process in Crystal Growth Far from Equilibrium”, (Springer, Berlin, 2004).

[31] G. Ehrlich, F. G. Hudda, ”Atomic view of Surface Diffusion: Tungsten on Tungsten, J. Chem. Phys. 44, 1039 (1966).

[32] R. L. Schwoebel and E. J. Shipsey, ”Step Motion on Crystal Surfaces:, J. Appl. Phys. 37, 3682 (1966).

[33] R. L. Schwoebel, “Step Motion on Crystal Surfaces II”, Journal of Applied Physics 40, 614 (1969).

[34] F. Family and T. Vicsek, “Dynamics of Fractal Surfaces” (World Scientific, Singapore, 1991).

[35] A-L. Barabasi, “Fractal Concepts in Surface Growth”, Cambridge (1995).

[36] W. Burton, N. Cabrera and F. Frank, Trans. Royal Soc. London, A 243, 299 (1951).

[37] G. S. Bales and A. Zangwill, “Morphological Instability of a Terrace Edge during Step-flow Growth”, Phys. Rev. B 41, 5500 (1990).

[38] K. Bromann, H. Brune, H. Rűder, K. Kern, “Interlayer Mass Transport in Homoepitaxial Metal Growth, Phys. Rev. Lett. 75, 677 (1995).

[39] J.A. Meyer, J. Vrijmoeth, H.A. van der Vegt, E. Vlieg, R.J. Behm, “Importance of The Additional Step-Edge Barrier in Determining Film Morphology during Epitaxial Growth”, Phys. Rev. B 51 14790(1995).

[40] P. Smilauer and S. Harris, “Determination of Step-Edge Barriers to Interlayer Transport from Surface Morphology During the Initial Stages of Homoepitaxial Growth”, Phys. Rev. B 51, 14798 (1995).

[41] I. Markov,”Method for Evaluation of the Ehrlich-Schwoebel Barrier to Interlayer Transport in Metal Homoepitaxy”, Physical Review B 54, 17930 (1996).

[42] K. Morgenstern, G. Rosenfeld, E. Laegsgaard, F. Besenbacher, G. Comsa, "Measurement of Energies Controlling Ripening and Annealing on Metal Surfaces", Phys. Rev. Lett. 80. 556 (1998).

[43] D. J. Eaglesham and G. H. Gilmer," Roughening during Si Deposition at Low Temperature, in: R. Jullien, J. Kertesz, P. Meakin, D. E. Wolf (Eds), "Surface Disordering: Growth, Roughening and Phase transformation, Vova Science, New York,(1993).

[44] J. E. Van Nostrand, S. J. Chey, and D. G. Cahill, "Low-temperature Growth Morphology of Singular and Vicinal Ge(001)", Phys. Rev. B, 57, 12536 (1998).

[45] S. J. Liu, E. G. Wang, C. H. Woo and H. C. Huang, J. Computer-Aided Materials Design 7, 195 (2001).

[46] A. Cho, "Film Deposition by Molecular Beam Techniques," J. Vac. Sci. Technol. 8 S31 (1971).

[47] C. T. Foxon, "MBE Growth of GaAs and III-V Alloys", J. Vac. Sci. Technol. B 1 293 (1983).

[48] M. D. Pashley, "Electron Counting Model and its Application to Island Structures on Molecular-beam Epitaxy Grown GaAs(001) and ZnSe(001)". Phys. Rev. B. 40, 1048 (1989).

[49] E. A. Wood," Vocabulary of Surface Crystallography," J. Appl. Phys. 35, 1306 (1964).

[50] M. Lannoo,"Basic Principles Governing the Surface Atomic Structure of Zinc Blende Semiconductors" Materials Science and Engineering B, 22(1993) 1.

[51] A. Ohtake, M. Ozeki, T. Yasuda and T. Hanada," Atomic Structure of the GaAs(001) Surface under As flux", Phys. Rev. B, 65 165315. (2002).

[52] A. Ohtake, P. Kocan, J. Nakamura, A. Natori and N. Koguchi," Kinetics in Surface Reconstructions on GaAs(001)", Phys. Rev. Lett. 92, 236105 (2004).

[53] K. Kanisawa & H. Yamaguchi, "Extremely long Surface Diffusion of Ga and Critical on As-rich GaAs(001) Surfaces Caused by Phase Transition" Physical Review B, 56, 12080 (1997).

[54] T. Hashizume, Q. K. Xue, A. Ichimaya, and T. Sakurai, "Determination of the Surface Structures of the GaAs(001)-(2x4) As-rich Phase", Phys. Rev. B 51, 4200 (1995).

[55] G. B. Bell, T. S. Jones, and B. A. Joyce, "Direct Observation of Anisotropic Step Activity on GaAs(001)". Surface Sci. 429, L492 (1999).

[56] W. Brau,"Applied RHEED: Reflection High-Energy Electron Diffraction During Crystal Growth", Springer (Berlin 1999).

[57] http://www.hostultra.com/~mhegazy/rheed.htm

[58] A. Pimpinelli and J. Villain, "Physics of Crystal Growth", Cambridge University Press (Cambridge, 1997).

[59] M. den Nijs, E. K. Riedel, E. H. Conrad & T. Engel,"Roughening of Stepped Metal Surfaces", Phys. Rev. Lett.14 1689 (1985).

[60] K. Rommelse and M. den Nijs,"Preroughening Transitions in Surfaces", Phys. Rev. Lett., 59 2578 (1987).

[61] M. den Nijs, "Roughening, Preroughening, and Reconstruction Transitions in Crystal Surfaces" in The Chemical Physics of Solid Surfaces and Heterogeneous Catalysis, Vol.7, edited by D. King, Elsevier (Amsterdam, 1994).

[62] M. Yamada and Y. Ide, "Anomalous Behaviors Observed in Isothermal Desorption of GaAs Surface Oxides", Surface Sci. Lett. L914(1995).

[63] Y. Asaoka, "Desorption Process of GaAs Surface Native Oxide Controlled by direct Ga-beam irradiation", J. Crys. Growth 251, 40 (2003).

[64] A. Ballestad, B. J. Ruck, J. H. Schmid, M. Adamcyk, E. Nodwell, C. Nicoll, and T. Tiedje, "Surface Morphology of GaAs during Molecular Beam Epitaxy Growth: Comparison of Experimental Data with Simulations based on Continuum Growth Equations", Phys. Rev. B 65, 205302 (2002).

[65] T. Sugaya and M. Kawabe, "Low-Temperature Cleaning of GaAs Substrate by Atomic Hydrogen Irradiation", Lap. J. Appl. Phys. 30, L402 (1991).

[66] M. Yamada "GaOH: Unstable Species Liberated from GaAs Surface Oxides during Atomic Hydrogen Cleaning", Jap. J. Appl. Phys., part 2, 35 L651 (1996).

[67] Y. Ide and M. Yamada, "Role of Ga in the Removal of GaAs Surface Oxides Induced by Atomic Hydrogen", J. Vac. Sci. Technol. A 12 1858 (1994).

[68] T. Ogino, Surface Sci. 386, 137 (1997).

[69] S. Tanaka, N. C. Bartelt, C. C. Umbach, R. M. Tromp, and J. M. Blakely, Phys.Rev. Lett. 78, 3342 (1997); S. Tanaka, C. C. Umbach, and J. M. Blakely, R. M. Tromp and M. Mankos, J. Vac. Sci. Technol. A 15, 1345 (1997).

[70] H.-C. Kan, S. Shah, T.T. Tadyyon-Eslami and R.J. Phaneuf, "Transient Evolution of Surface Roughness on Patterned GaAs(001) during Homoepitaxial Growth" Phys. Rev. Lett., 92, 146101 (2004).

[71] M. Kardar, G. Parisi, and Y.-C. Zhang, Phys. Rev. Lett., 56, 889 (1986).

[72] Z.-W. Lai, and S.Das Sarma, Phys. Rev. Lett., 66, 2348 (1991).

[73] H.-C. Kan, R. Ankam, S. Shah, K. M. Micholsky, T. Tadayyon-Eslami, L. Calhoun and R. J. Phaneuf, " Evolution of Patterned GaAs(001) during Homoepitaxial Growth: Size versus Spacing", Phys. Rev. B 73 195410 (2006).

[74] T. Tadayyon-Eslami,H.-C. Kan, L. C. Calhoun and R. J. Phaneuf ,"Temperature-Driven Change in the Unstable Growth Mode on Patterned GaAs(001)" Phys. Rev. Lett., accepted (2006).

[75] A. Kley and M. Scheffler, "Diffusivity of Ga adatoms on GaAs(001)". in Proc. 23rd Int. Conf. on the Physics of Semiconductors, M. Scheffler and R. Zimmermann, Editors. 1996, World Scientific: Singapore. P.1031.

[76] T. Shitara, D. D. Vvedensky, M. R. Wilby, J. Zhang, J. H. Neave, and B. A. Joyce, "Misorientation dependence of epitaxial growth on vicinal GaAs(001)". Physical Review B 46, 6825(1992).

[77] S. Shah, master Thesis, University of Maryland, 2004.

[78] T.J. Newman and A. J. Bray,"Strong-Coupling Behavior in Discrete Kardar-Parisi – Zhang Equations", J. Phys. A 29, 7917 (1996).

[79] J. Villain, "Continuum Models of Crystal Growth from Atomic Beams with and without Desorption", Journal De Physique I, 1(1991)19.

[80] P. Politi, G. Grenet, A. Marty, A. Ponchet and J. Villain, "Instabilities in Crystal Growth by Atomic or Molecular Beams", Physics Reports 324(2000)271.

[81] I. Elkinani and J. Villain, "Growth Roughness and Instabilities due to the Schwoebel Effect: A One-Dimentional Model", Journal De Physique I, 4(1994)949.

[82] V. P. LaBella, D. W. Bullock, M. Anser, Z. Ding, C. Emery, L. Bellaiche, and P. M. Thibado, "Microscopic View of a Two-Dimensional Lattice Gas Ising System within theGrand Canonical Ensemble", Phys. Rev. Lett. 84, 4152 (2000).

[83] M. den Nijs,"Preroughening of Crystal Surfaces and Energy Differences Between Inside and Outside Corners", Phys. Rev. Lett. 64, 435 (1990).

[84] V. Tsai, X.-D. Wang, E.D. Williams, T.V. Vorburger, R. Dixon, J. Fu, J. Schneir and T. McWaid, "Conformal Oxides on Si Surface,", Appl. Phys. Lett. 71, 1495 (1997).

[85] L. C. Calhoun, private communication.

[86] Z. Ding, D. W. Bullock, P. M. Thibado, V. P. Labella & Kieran Mullen, "Time-evolution of the GaAs(001) Pre-roughening Process", Surface Science540, 491 (2003).

[87] S. J. Liu, E. G. Wang, C. H. Woo and H.C. Huang, "Three-dimensional Schwoebel–Ehrlich barrier", J. Computer-Aided Materials Design, 7, 195 (2001).

[88] It is likely that step flow occurs at the side walls of the pits, however, due to the small terrace widths.